THE EFFECTS OF TORSIONAL-LATERAL COUPLING ON THE

DYNAMICS OF A GEAR COUPLED ROTOR

A Thesis

by

MICHAEL AARON EMERY

Submitted to the Office of Graduate Studies of
Texas A&M University
in partial fulfillment of the requirements for the degree of

MASTER OF SCIENCE

December 2005

Major Subject: Mechanical Engineering

THE EFFECTS OF TORSIONAL-LATERAL COUPLING ON THE

DYNAMICS OF A GEAR COUPLED ROTOR

A Thesis

by

MICHAEL AARON EMERY

Submitted to the Office of Graduate Studies of
Texas A&M University
in partial fulfillment of the requirements for the degree of

MASTER OF SCIENCE

Approved by:

Chair of Committee,   John Vance
Committee Members, Alan Palazzolo
                                  Yassin Hassan
Head of Department, Dennis O'Neal

December 2005

Major Subject: Mechanical Engineering

ABSTRACT

The Effects of Torsional-Lateral Coupling on the Dynamics of a Gear Coupled Rotor.
(December 2005)
Michael Aaron Emery, B.S., Texas A&M University
Chair of Advisory Committee: Dr. John Vance

This thesis focuses on the torsional-lateral interactions seen in gear coupled rotors. Of particular interest are cases where the torsional stiffness parameters affect the lateral critical speeds and where lateral stiffness and damping parameters affect torsional critical speeds and amplitudes. A common procedure for critical speed calculations has been to solve lateral and torsional systems separately. This procedure is tested through an eigenvalue analysis.   It is shown in this thesis, however, that torsional-lateral interactions play major roles in each other's critical speeds.   Some research has seemingly uncoupled two lateral degrees of freedom from the gear system by choosing bearing forces and a coordinate system pointing along the line of action and normal to the line of action. This simplification method has been tested for cases when the lateral bearing stiffness becomes asymmetric. The force generated by a rotating imbalance also creates a variable moment arm as the center of mass rotates about the geometric center of the gear. This variable moment arm is commonly neglected, but is included in the last case study and its effects are displayed in the results section of this thesis.

DEDICATION

To Renee, because I wouldn't be where I am today without her love and support.

NOMENCLATURE

R_1	Pitch Radius of Gear 1
R_2	Pitch Radius of Gear 2
u_1	Distance to Mass Unblance on Gear 1
u_2	Distance to Mass Unblance on Gear 2
m_1	Mass of Gear 1
m_2	Mass of Gear 2
J_1	Mass Moment of Inertia of Gear 1
J_2	Mass Moment of Inertia of Gear 2
K_n	Equivalent Tooth Stiffness
K_t	Torsional Shaft Stiffness
K_{xx1}	X-Lateral Shaft Stiffness of Gear 1
K_{yy1}	Y-Lateral Shaft Stiffness of Gear 1
K_{xx2}	X-Lateral Shaft Stiffness of Gear 2
K_{yy2}	Y-Lateral Shaft Stiffness of Gear 2
C_{xx1}	X-Lateral Shaft Damping of Gear 1
C_{yy1}	Y-Lateral Shaft Damping of Gear 1
C_{xx2}	X-Lateral Shaft Damping of Gear 2
C_{yy2}	Y-Lateral Shaft Damping of Gear 2
C_{t_1}	Torsional Damping of Gear 1
C_{t_2}	Torsional Damping of Gear 2
α	Gear Pressure Angle
p_d	Diametral Pitch

TABLE OF CONTENTS

LIST OF FIGURES

LIST OF TABLES

I. INTRODUCTION: THE NEED TO DEVELOP A GEAR COUPLED DYNAMIC MODEL

Gear vibration brings unique challenges to the field of rotordynamics when considering the coupling caused by the mesh of the gear teeth. In order for the equations of motion to realistically represent rotors connected by gears, five degrees of freedom (DOF) need used to represent the shaft motion at any station. Currently, rotordynamic software packages use two simplified sets of equations (one lateral set and one torsional set) to describe the motion seen in gear coupled rotors. These equations of motion have neglected the torsional-lateral coupling as well as the contribution of the gear tooth stiffness. In some instances, the uncoupled model for the coupled system has produced accurate results. However, the uncoupled model's equations of motion may not be accurate for cases where the torsional-lateral coupling is significant.

The objective of this thesis is to provide a better understanding of the torsional-lateral interaction and when its effects are significant. Several studies listed below have been conducted in order to fulfill this objective:

1. Compare the natural frequencies of the coupled model to the natural frequencies of the uncoupled model as a function of torsional stiffness.
2. Investigate the effects of varying torsional stiffness on torsional-lateral coupled natural frequencies and mode shapes with symmetric support stiffness.
3. Investigate the effects of varying torsional stiffness on torsional-lateral coupled natural frequencies and mode shapes with asymmetric support stiffness.
4. Investigate the effects of varying lateral stiffness on torsional-lateral coupled natural frequencies with symmetric support stiffness.
5. Compare the lateral critical speeds from the coupled model to the lateral critical speeds of the uncoupled model using rotating mass imbalance as the exciting force.
6. Investigate the possibility of stable subsynchronous vibrations caused by forces in the low speed gear.

This thesis follows the style of Journal of Engineering for Gas Turbines and Power.

7. Investigate the 2nd order harmonic effects caused by a rotating moment arm using numerical integration and FFTs. This investigation will include the development of waterfall plots for a range of running speeds.

If any debate exists on whether to couple the torsional equations of motion to the lateral equations of motion when solving for geared system lateral and torsional critical speeds, this thesis should help resolve the matter.

II. LITERATURE REVIEW

BACKGROUND INFORMATION

Wachel and Szenasi

Subsynchronous vibrations in several centrifugal compressors prompted the study presented in 1980 by Wachel and Szenasi [1]. One of the machines producing subsynchronous vibrations was a compressor coupled to a turbine with a gear box. Figure 1 shows the schematic of the compressor train.
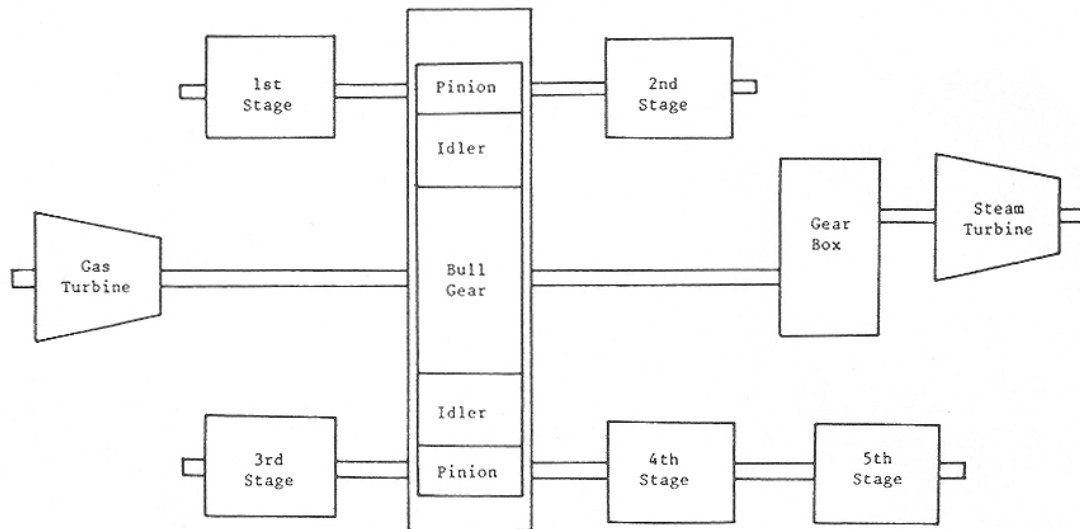
Figure 1: Schematic of the compressor train [1]

Proximity probes were used to measure lateral vibrations in the fourth stage compressor as well as the lateral vibrations in the gear box. Torsiographs were also installed in the gear box to measure the torsional vibration seen by the gear teeth. Rigid couplings were used on the shafts connecting the turbines and compressors to the gear box, allowing lateral vibrations to transmit between the components of the train. Lateral vibrations of the fourth stage compressor were measured and were interpreted as subsynchronous instabilities. The authors note that the frequency of these lateral vibrations coincided with the third torsional natural frequency of the compressor train.

The lateral instabilities were eventually corrected when the bearings for the fourth stage compressor was changed from pressure pad bearing to tilt pad bearings. Threshold instability calculations based on the logarithmic decrement showed that the compressor would be stabile with the new bearings. These stability calculations were confirmed from low frequency, maximum load test data.

The subsynchronous vibrations seen in the fourth stage compressor were still apparent on initial startup. The authors found that this vibration was caused by the idler gear exciting the natural frequency of the compressor shaft. Increased damping improved the amplitude of this low frequency vibration.

Based on the test data, Wachel concludes that the torsional vibrations and the lateral vibrations are coupled at torsional natural frequencies. Furthermore, he concludes that this coupling mechanism can be a catalyst for inciting any instabilities that may exist in the machine.

Remmers
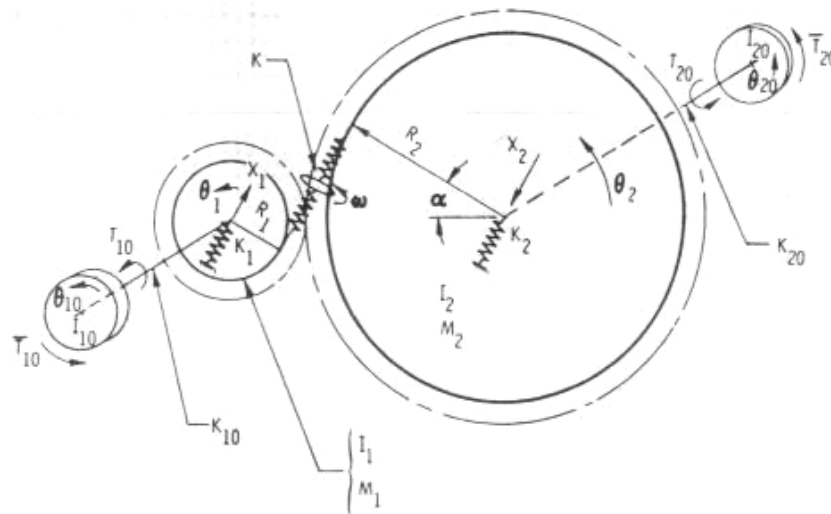
Figure 2: Mass elastic system [2]

In his paper published in 1971 on gear paired systems, Remmers details the effects of gear tooth errors and the mass inertia characteristics of the gear system. Remmers explains the model of a gear paired system to be one with involute gears where the forces act along the line of action, which is tangent to the base circle outlined in Figure 2.

When the gear train is stationary, the gear teeth stresses can be modeled as a cantilevered beam. However, this analysis is no longer accurate once the system is in motion. Gear tooth errors cause the transmission of motion from one gear to another to be less than ideal. Remmers suggests that the transmission error could be measured with the use of a single flank gear tester, but cautions that this method does not take into account tooth deflections or the effect of lubrication. He also notes that this analysis must be done with a load as close to zero as possible. The result of this analysis, the external excitation, is taken as the linear equivalent to the angular error, or

$$X_e = \varepsilon \sin \omega t \qquad (1)$$

where: X_e = Instantaneous Error, ε = Amp. (in), ω = Frequency (rad/s) and t = Time (sec)

Remmers derived the governing differential equations of motion for the gear coupled system by summing the forces and summing the moments in the X_1, X_2, θ_1, θ_2 directions. The forces in the Y directions have not been considered since friction has been assumed minimal and no bearing forces appear in the Y direction. The force along the line of action between the gears is given as:

$$F = K[(X_1 + X_2)(1 + \sin^2 \alpha) + R_1\theta_1 + R_2\theta_2 + \varepsilon \sin \omega t] \qquad (2)$$

which is based on the standard F=KX equation for a spring force. Assuming a solution of the form $e^{i\omega t}$ and substituting the back into the force and moment equations will yield six equations and six unknowns and the ratios of response can now be calculated. These ratios are important in that they are used to solve for the dynamic forces, torques, and torsional vibrations on the gears.

Remmers justifies his theory by collecting data on the "frictional effects, profile modifications, tooth deflections, and the excitation spectrum for different gear designs" (page 6). Figure 9 and Figure 10 on page 7 of this article shows how close the experimental data was to the theoretical data. While the frequency of the peaks closely agrees with those predicted by theory, the forces predicted by theory are several orders of magnitude larger than the experimental values. Remmers explains this by stating that the assumed coefficient of friction played a large role in the overestimation of these forces and that improvements should be made to the dynamic model to enhance the precision of predicted forces.

Mitchell

In his paper published in 1975, Mitchell [3] showed through experimental results that uncoupled equations of motion are inadequate for calculating natural frequencies. His conclusions were based on a comparison of his measured experimental vibrations to the uncoupled theoretical model. The test rig used in this experiment consisted of three

gears; one bull gear driven by a motor and two pinions with heavy inertias connected to both sides. The test was performed on the system several times with varying torsional shaft stiffness values.
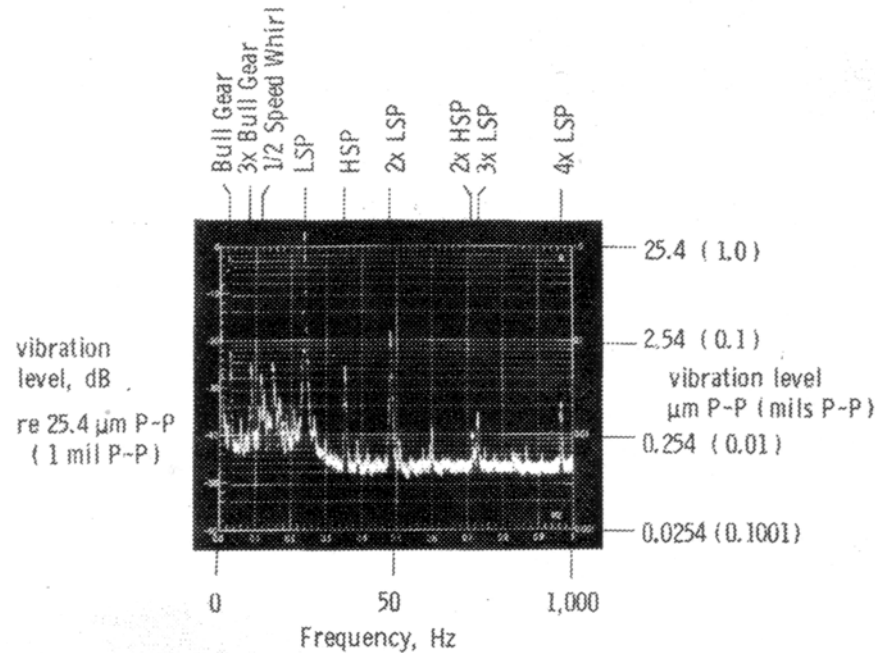
Figure 3: Vibration spectrum of low speed pinion shaft [3]

Vertical vibration amplitudes were measured using non-contacting proximity probes and the vibration data was processed with a Real-Time Signal Analyzer. The results show that the system exhibits peak responses above the predicted critical speeds by as much as 12 percent. Further analysis using the Fast Fourier Transform function on the signal analyzer in Figure 3 shows 2nd, 3rd, and 4th order harmonics. Mitchell concludes that dynamic models should move towards completely coupling the torsional and lateral equations of motion in order to accurately predict critical speeds.

Iwatsubo

Further findings in the subject of geared coupled rotors included Iwatsubo's [4] study in 1984 on lateral torsional vibrations. The main focus of this study was to determine the effect of the variation of tooth stiffness on torsional critical speeds. The variation in tooth stiffness has been taken as the exciting force in the torsional direction and the

forces caused by imbalance were assumed minimal. The coordinate system is set up so that the Y directions align normal to the tooth pressure angle, allowing the meshing force to be considered in the X direction alone. Using this coordinate convention allows Iwatsubo to uncouple the Y equations from the remaining equations of motion. He uses this reasoning to ignore vibrations in the Y direction altogether. His work showed that unstable regions occurred for some running speeds because of the variation of tooth stiffness. He also concluded that vibrations are affected by the mesh period as well as the contact ratio.

Iida and Tamura

Iida and Tamura's study published in 1984 [5] on gear dynamics focuses on cases where the gear shaft cannot be assumed rigid. The dynamic model was developed for a system containing four gears with three flexible shafts. The research also involved taking experimental data from a physical setup representing the dynamic model. The authors concluded through numerical integration and experimental results that the torsional and lateral modes of vibration are coupled.

Iannuzzelli, Raymond, and Edwards

A geared compressor failure became the basis of Iannuzzelli's and Edwards's study [6] on torsional lateral coupling published in 1984. The problems that occurred in the field eventually required a better analytical model, which the authors realized should include the torsional lateral coupling produced by the gear mesh. Finite element analysis was utilized for the new model and included the torsional degrees of freedom. The model developed did not include external excitation forces, but was used for eigenvalue/eigenvector analysis.

One of the key elements in this paper is the notion that the forces create a moment about the centerline of the gears. This differs slightly from the topic of this thesis, in that the moments are taken about the geometric center of the gear, and is assumed that

the bearing forces act some constant distance away from the geometric center. The authors did not consider the response due to unbalance or the effect of the varying moment it produces.
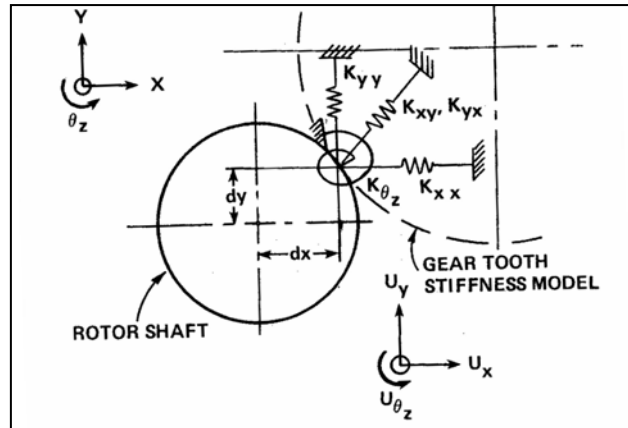
Figure 4: Diagram for derivation of mesh stiffness equations [6]

Iannuzzelli also includes the cross-coupling stiffness terms K_{xy} and K_{yx} (as seen in Figure 4) that are created by spring displacements in the X and Y directions. A major draw back with this model was the assumption that the inertia of the bull-gear could be neglected. This reduced the system from a six degree of freedom system to a three degree of freedom system and gives rise to the possibility that several natural frequencies could be missed.

Iannuzzelli and Edwards also conducted tests to validate their new computer model. Several experiments were performed on the rig to show how stiffening lateral bearing parameters affected the natural frequency of the system. The authors show that the measured data closely matched the theoretical predictions of the new computer model. Since their model only contained three degrees of freedom, the first natural frequency was not predicted at all though some improvement was made in the predict for the other modes.

Simmons and Smalley

In their paper published in 1984 [7] on lateral gear shaft dynamics, H. R. Simmons and A. J. Smalley compare the various rules of thumb used in industry to actual measurements. Their goal in this research project was to show the inaccuracy of uncoupled equations of motion in certain cases when calculating critical speeds. They concluded through experimental results that for accurate predictions, the equations of motion should remain coupled.

Appendix B gives a simplified version of the method developed by Lund in his paper entitled "Critical Speeds, Stability and Response of a Gear Trained Rotor." Simmons and Smalley used Lund's method to develop a torsional-lateral vibration model. The authors use this model to predict the torsional critical speeds which will be compared to the verified speeds found from experimental data. The basis behind this method is to treat the system as a series of lumped masses connected by massless springs. A more detailed discussion of this method will be given in Section 3 of this paper.

The theoretical results were evaluated in the laboratory and compared to experimental results. Simmons and Smalley utilized several transducers in this effort, including the "torsional strain telemetry system" shown in Figure 5 below.
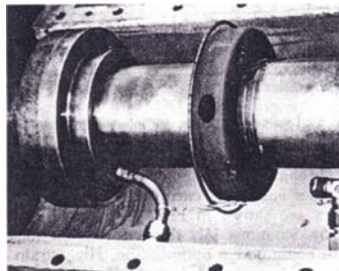
Figure 5: Strain gauge telemetry system on coupling spool piece [7]

The test results show that high stresses on the gears are caused by the excitation of the turbine's second torsional critical speed at 65% running speed and by the gearing backlash caused by low compressor loads around 30% running speed. These critical

speeds are clearly seen in the Stress vs. Speed graph (Figure 7) found on page 948 of the article. These test results also closely resembled the values predicted before the experiment and are shown in Table 2 on page 949, though the predicted damping values are consistently around half of the measured damping values.

The authors use Appendix A to give an overview of three methods employed in calculating the critical damping ratio from the experimental data. The three methods are the Half Power Method, the Phase Slope Method, and the Real Peak Method. The calculated critical damping ratios for each of these methods are listed in Table 1 on page 948. Note the large jump in the values estimated for the second mode of the compressor. It is the authors' belief that this mode is non-linear due to the backlash characteristics displayed by the gear system; hence, the wide range in critical damping ratios.

David and Park

David's and Park's [8] article published in 1987 focused on the forces generated in the gear mesh by the varying tooth stiffness over time. The authors use the Transfer Matrix Method to find the gear meshing forces and model the system using equations similar to the Simmons and Smalley paper, with the meshing force is given as:

$$F_n = \left[(X_1 - X_2)\cos\phi + (Y_1 - Y_2)\sin\phi + (r_{b1}\theta_1 - r_{b2}\theta_2) - e_t \right] K_e \qquad (3)$$

where ϕ = pressure angle, K_e = equivalent average tooth stiffness, and e_t = the displacement error.

In this case, the displacement error, otherwise known as Transmission Error, has been used to account for gear tooth errors. Results from an experimental Fast Fourier Transform (Figure 6) shows that higher ordered harmonic vibrations are caused by time varying tooth stiffness.
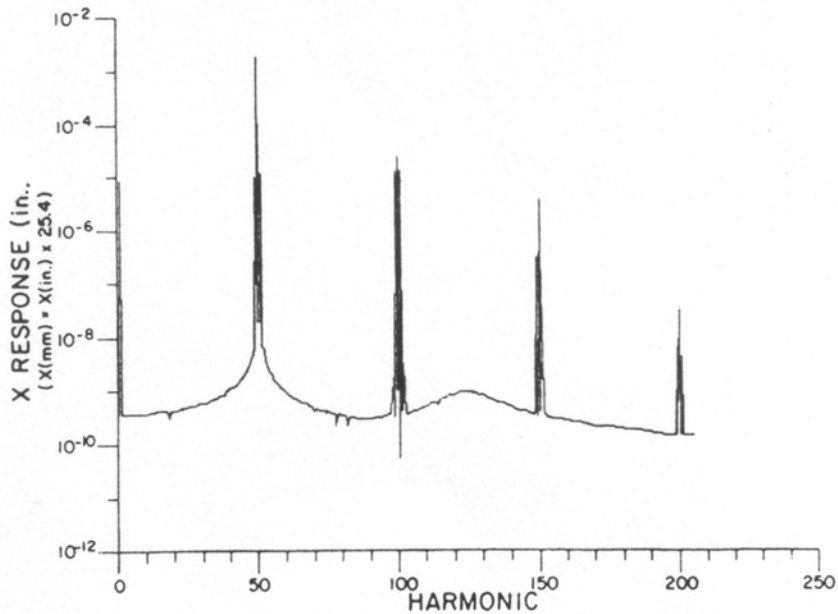
Figure 6: Lateral disk response due to unbalance and single frequency mesh force [8]

Ozguven and Houser

Ozguven's [9] work published in 1988 on gear dynamics became the reference for several papers that focused on the excitation of the variable stiffness characteristics of the gear mesh. For his study, the gear model has been reduced into a non-linear single degree of freedom system that uses Static Transmission Error as the exciting force. Transmission error describes where tooth contact is made in relation the perfect transfer of motion between two gears, and it has been used in place of the other types of gear contact error. Ozguven showed that Static Transmission Error can be used successfully to account for the varying equivalent tooth stiffness while using the average stiffness as a constant in the stiffness matrix.

Zuerbes, Neumer, Klimmek, Schwibinger, and Nordmann

In their paper published in 1989, Zuerbes [10] and his colleagues look at the coupled lateral torsional gear model. Two systems, one running on ball bearings and the other running on journal bearings, were analyzed for this project. One of the key features of this dynamic model was the exclusion of such phenomena as the variation of equivalent tooth stiffness and backlash. The authors contend that this simplification does not deleteriously affect the system behavior. The eigenvalues and eigenvectors were calculated from the equations of motion, but the effect of a rotating unbalance was not discussed.

Based on the test results, the authors conclude that for more accurate natural frequency predictions, the equations of motion should be coupled. The results showed great disparity when compared to the uncoupled equations of motion, including natural frequency and mode shape predictions, the stability of the machine, and non-linear bearing forces.

Kahraman, Ozguven, Houser, Zakrajsek

Kahraman's journal article in 1992 [11] focuses on the use of finite elements to model a geared rotor system. The work presented in this paper is a continuation of Ozguven's paper on high speed gears from 1988. A finite element rotordynamic software package (ROT-VIB^{TM}) was altered to include the torsional-lateral interaction caused by gear tooth mesh. The coordinate system was set up like Iwatsubo's, so that the gear meshing forces were isolated in the y-direction thus effectively uncoupling the x direction from the y direction. Though he included the addition moment terms caused by the rotating mass unbalance in his moment equation, they were not included in the forced response analysis and were assumed negligible. Kahraman concluded through his findings that bearing parameters play a major role in gear mesh natural frequency, depending on the bearing stiffness parameters. Increasing the stiffness of the flexible bearings changes the mesh frequency up to a certain limit. Increasing very stiff bearing values was not found to change the mesh frequency significantly. The results shown in

Figure 7 and Figure 8 demonstrate how both lateral and torsional response change with bearing stiffness.
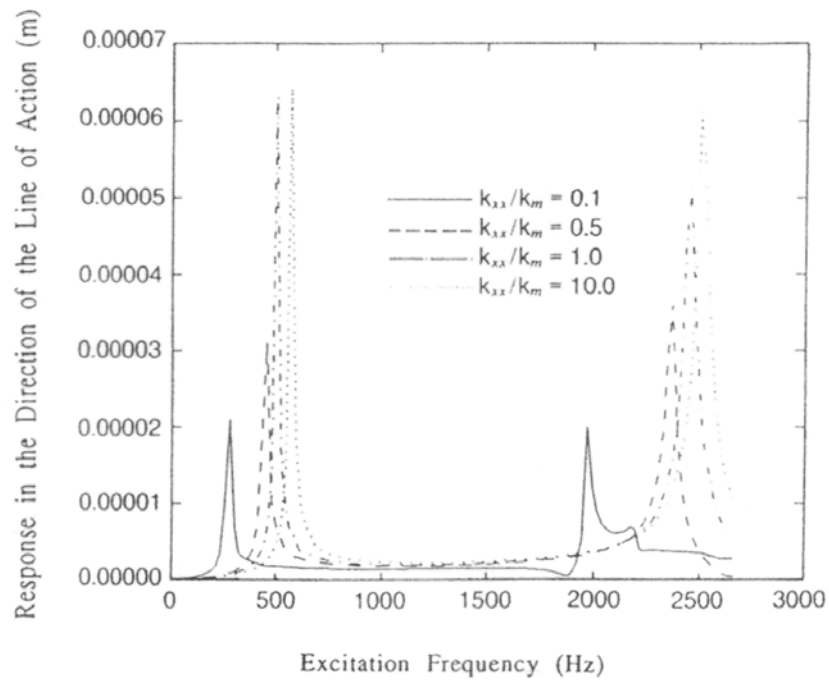
Figure 7: Forced response along line of action due to transmission error [11]
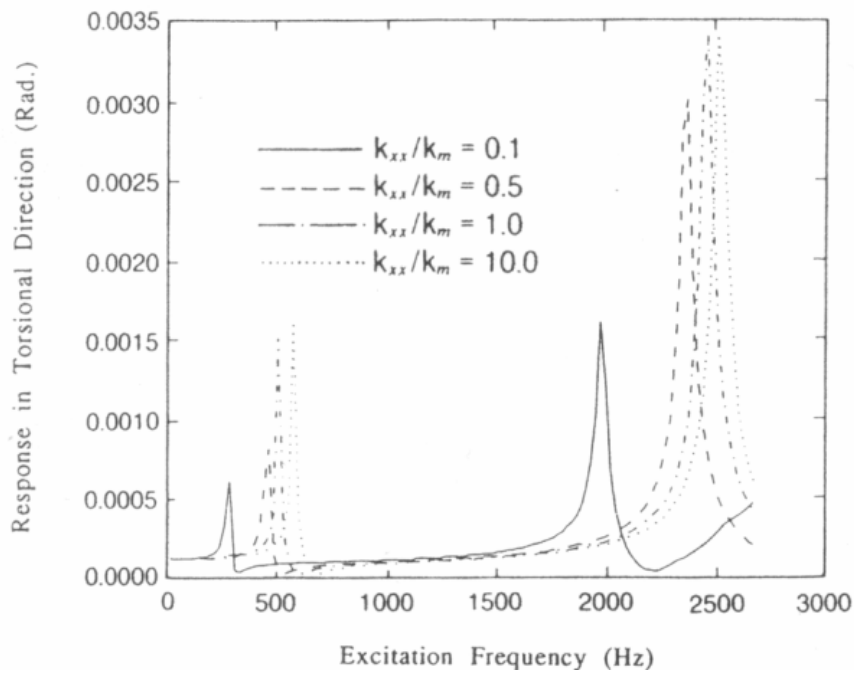
Figure 8: Forced response in the torsional direction due to transmission error [11]

Nelson, Shiau, Chou, and Chang

Nelson [12] expanded Ozguven's work in his paper in 1994 though he based his results on tests conducted by Kahraman [11]. While the finite element method offers very accurate results, it does so at the expense of computational times. In this paper, Nelson focused on the merits of using the Hybrid method to improve computational efficiency.

One of the studies included in his paper involved varying the mesh angle. Nelson concludes that the mesh angle plays an insignificant role for systems with symmetric bearing stiffness. This is not true, however, with asymmetric supports as the mesh angle significantly changes the torsional-lateral coupled natural frequencies.

Again, the excitation force of particular interest dealt with in Nelson's paper was transmission error. Forces caused by unbalance response were generally assumed negligible in most cases compared to the effects of transmission error. Theoretical analysis of the unbalance response was conducted in his paper, though it dealt with non-synchronous high frequency excitations. The theoretical results using the Hybrid method favorably agreed with the finite element method. This new method allows for quicker computational running times without losing significant accuracy.

III. MATHEMATICAL METHODOLOGY

This project deals with the torsional-lateral interactions found in geared rotors. The gear mesh pressure angle acts as a coupling mechanism between the torsional degrees of freedom and the lateral degrees of freedom. Currently, XLTRC^2 and other rotor analysis software packages independently calculate torsional and lateral critical speeds. To properly model either the torsional or the lateral rotordynamics of some systems, the torsional degrees of freedom must be included with the lateral degrees of freedom. The new gear dynamic model contains six degrees of freedom when the torsional-lateral coupling is included.

Figure 9 below illustrates the physical setup for this study. For the purposes of this study, standard AGMA spur gears were used, so the degrees of freedom associated with pitch and yaw can be neglected. Heavy loads have been assumed on each gear to maintain tooth contact.
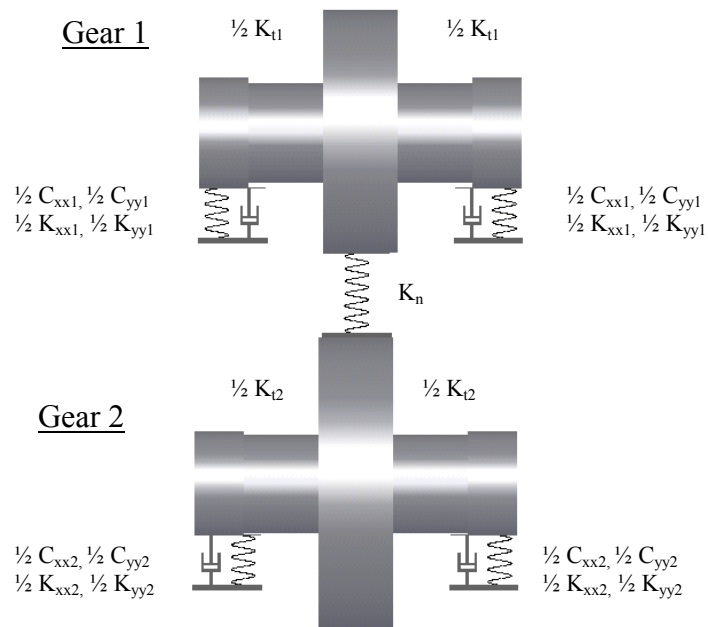
Figure 9: System for gear study

The key forces in the six equations of motion in this model are the bearing spring and the bearing damping forces, the torsional spring from the shaft, and the normal force applied to the gear tooth. Gyroscopic moments and friction against the gear teeth have been neglected.

For typical gears, more than one gear tooth pair is in contact at any given time, and this varies with time. Multiple gear teeth in contact serve to increase the equivalent spring stiffness at the gear mesh, since the cantilevered tooth springs are in parallel. Since this study focuses primarily on the interaction between lateral and torsional dynamics, the change in tooth stiffness will be averaged and assumed constant over time.

By making slight changes to the model's stiffness and damping parameters, key properties of the torsional-lateral coupling phenomena can be studied. The first study involves the torsional-lateral interactions found in the homogenous solution to the differential equations of motion. The eigenvalues and the eigenvectors are calculated based on given gear geometry and bearing parameters. The eigenvalue study helps to illustrate the effects the torsional and lateral support parameters play in each other's natural frequencies. This study also serves to verify the accuracy of the equations of motion.

One of the practices in the literature is to uncoupled the degree of freedom perpendicular to the line of action from the equation describing the normal force acting on the gear tooth. An eigenvalue analysis indicates that the assumption that the natural frequencies are independent of the torsional stiffness is not accurate when using asymmetric bearings.

Since critical speeds do not exactly match natural frequencies in cases where damping exists, a forced response case has also been studied. Instead of treating the transmission error caused by the variation of tooth stiffness over time as the primary excitation source, this study focuses on the vibrations caused by a rotating mass imbalance. The system has been assumed to be a short rigid rotor on flexible bearings where the stiffness and damping parameters come directly from the bearing.

The forced response case presents a problem when dealing with the torsional equations of motion. The rotating mass imbalance creates varying moments which, on first inspection, appear to be 2nd order harmonic. This moment was initially ignored in the forced response analysis, but is studied in depth using numerical integration techniques. A Fast Fourier Transform of the numerical integration results shows the harmonic vibration components at each running speed that cannot be seen in the forced response analysis of the linearized system.

DETERMINATION OF TOOTH STIFFNESS
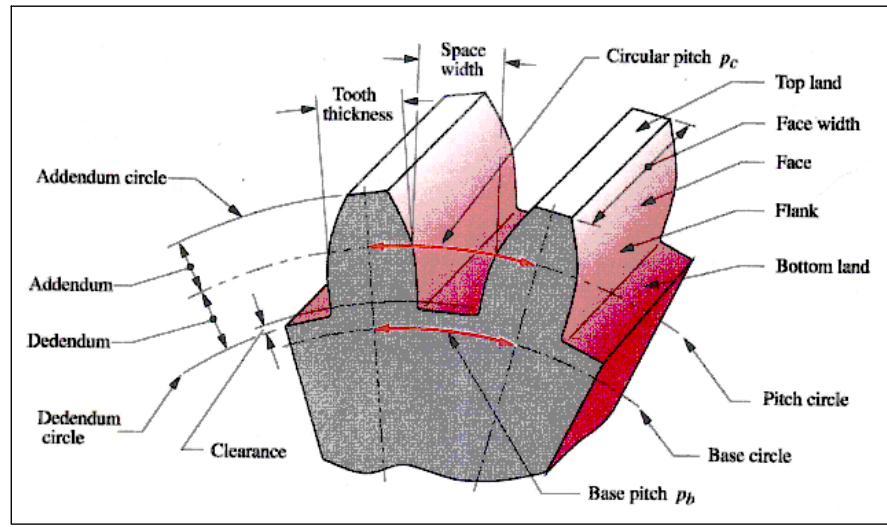
Figure 10: Common gear terminology [13]

The stiffness of the gear teeth was calculated using Euler beam bending theory equations and the gear terminology described in Figure 10. The equations below show how the gear tooth stiffness should be calculated. The tooth was approximated as a rectangular beam mounted into a rigid support.

$$I = \frac{(\text{Face Width})(\text{Tooth Thickness})^3}{12} \qquad (4)$$

$$\text{Tooth Thickness} = \frac{1.571}{p_d} \qquad (5)$$

$$\text{Addendum} = L = \frac{2.25}{p_d} \qquad (6)$$

$$\text{Stiffness of Single Tooth} = K_n = \frac{3EI}{L^3} \qquad (7)$$

The diametral pitch (p_d) is the ratio of gear teeth to pitch diameter and is shared by all of the gears in the gear train. At least two of these three parameters (usually the diametral pitch and the number of gear teeth) must be given in order to calculate the tooth stiffness. Two teeth in contact act as two springs in series, making the equivalent tooth stiffness of the system

$$K_n = \frac{K_{n1}K_{n2}}{K_{n1}+K_{n2}} \qquad (8)$$

Accounting for Multiple Gears Teeth in Contact
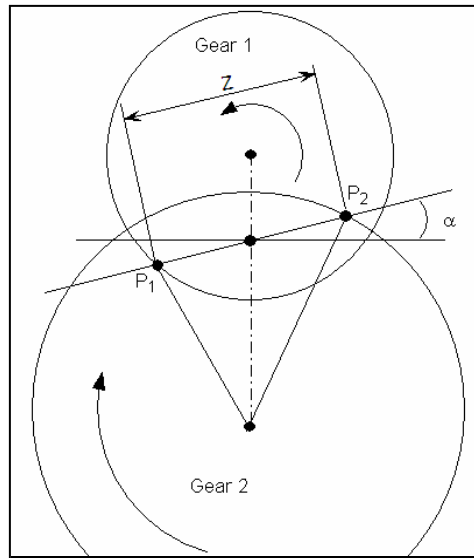
Figure 11: Sketch of gear system and line of action

$$C = R_1 + R_2 \qquad (9)$$

$$R_1 = \frac{N_1}{2p_d} \qquad (10)$$

$$R_2 = \frac{N_1}{2p_d} \qquad (11)$$

$$R_{b1} = R_1 \cos(\alpha) \qquad (12)$$

$$R_{b2} = R_2 \cos(\alpha) \qquad (13)$$

$$a = \frac{1}{p_d} \qquad (14)$$

$$m_p = \frac{Z}{p_b} = \frac{\sqrt{(R_1 + a)^2 - R_{b1}^2} + \sqrt{(R_2 + a)^2 - R_{b2}^2} - C\sin(\alpha)}{\left(\dfrac{2\pi R_{b1}}{N_1}\right)} \qquad (15)$$

where the subscripts describe the gear, pd = Diametral Pitch, p_b = Base Pitch, R = Pitch Radius, N = Number of Gear Teeth, α = Addendum, mp = Contact Ratio [14], R_b = Base Radius, C = Center to Center Distance, Z = Length of Action.

Gear teeth mesh along the line of action (Z); an imaginary line whose angle is co-linear to the pressure angle (see Figure 11). Tooth contact and the release of tooth contact occur when the line of action crosses the addendum circle of first and second gear respectively. At some point before contact is terminated, another tooth pair initiates contact. For the purposes of this study, however, the equivalent tooth stiffness was taken to be the average over time based on the gear contact ratio. Figure 12 illustrates how the equivalent tooth stiffness changes over the contract cycle. The gear contact ratio shows the average number of teeth in contact over the entire line of action.
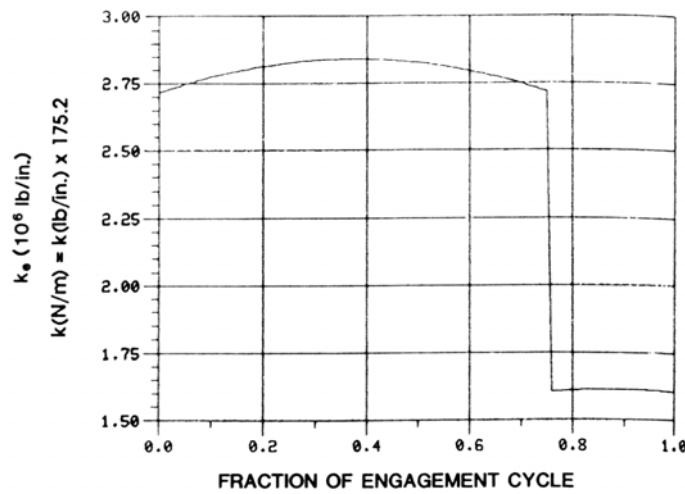
Figure 12: Tooth stiffness vs. fraction of engagement cycle [8]

External spur gears generally have a contact ratio between 1.2 and 2, which indicates that for some portion during the gear mesh two gear tooth pairs make contact. The average tooth stiffness takes into account the average number of tooth pairs in contact over the length of the line of action.

$$K_{neq} = (m_p - 1)(2K_n) + (2 - m_p)K_n \qquad (16)$$

This equation assumes a contact ratio between 1 and 2. When the contact ratio equals one, multiple tooth pairs never make contact while single pair contact occurs throughout the contact cycle of the gear teeth. As the contact ratio increases, more multiple pair contact occurs while less single tooth contact decreases. External spur

gears rarely have gear contact ratios greater than two. For those rare cases, the equivalent stiffness equation should be adjusted accordingly.

DEVELOPING HOMOGENEOUS EQUATIONS OF MOTION FOR A SINGLE GEAR PAIR ON FLEXIBLE SUPPORTS
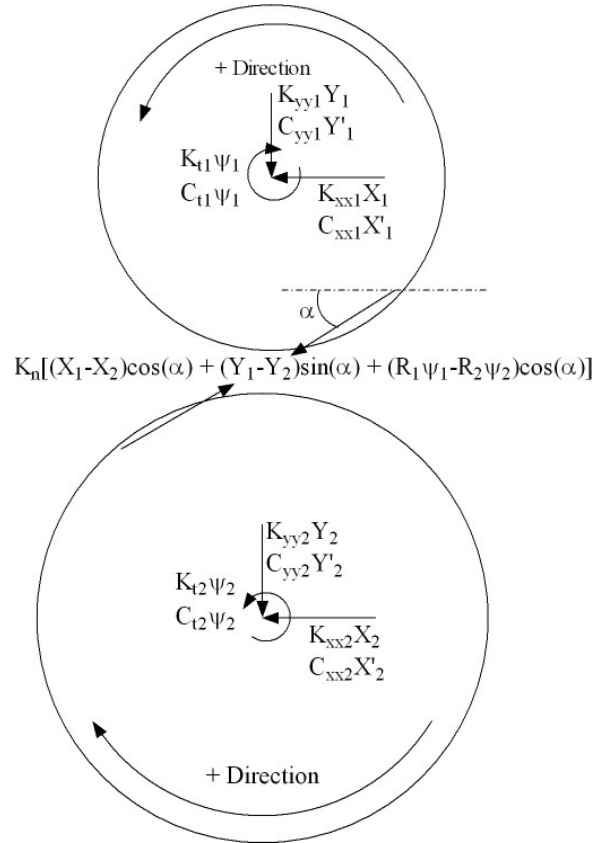
Figure 13: Free body diagram

The development of the equations of motion starts with expressing the normal force on the tooth in terms of the chosen X-Y coordinates based on the free body diagram in Figure 13. The normal force on the face of the gear tooth is then defined as [7]:

$$F_n = K_n[(X_2 - X_1)\cos(\alpha) + (Y_2 - Y_1)\sin(\alpha) + (R_2\psi_2 - R_1\psi_1)\cos(\alpha)] \qquad (17)$$

where K_n is the tooth stiffness, α is the pressure angle, and the subscripts represent displacements of Gears 1 and 2. The terms, ψ_1 and ψ_2 are state variables to be included for torsional-lateral interaction. From here, the normal force is resolved into X and Y components and the sum of all forces and moments are taken to develop the equations of motion.

$$F_{nx} = K_n[(X_1 - X_2)\cos(\alpha) + (Y_1 - Y_2)\sin(\alpha) + (R_1\psi_1 - R_2\psi_2)\cos(\alpha)]\cos(\alpha) \quad (18)$$

$$F_{ny} = K_n[(X_1 - X_2)\cos(\alpha) + (Y_1 - Y_2)\sin(\alpha) + (R_1\psi_1 - R_2\psi_2)\cos(\alpha)]\sin(\alpha) \quad (19)$$

Gear 1:

$$\sum F_{x1} = m_1\ddot{X}_1 = -C_{xx_1}\dot{X}_1 - K_{xx_1}X_1 - F_{nx} \quad (20)$$

$$\sum F_{y1} = m_1\ddot{Y}_1 = -C_{yy_1}\dot{Y}_1 - K_{yy_1}Y_1 - F_{ny} \quad (21)$$

$$\sum M_{cg1} = J_1\ddot{\psi}_1 = -C_{t_1}\dot{\psi}_1 - K_{t_1}\psi_1 - R_1F_{nx} \quad (22)$$

Gear 2:

$$\sum F_{x2} = m_2\ddot{X}_2 = -C_{xx_2}\dot{X}_2 - K_{xx_2}X_2 + F_{nx} \quad (23)$$

$$\sum F_{y2} = m_2\ddot{Y}_2 = -C_{yy_2}\dot{Y}_2 - K_{yy_2}Y_2 + F_{ny} \quad (24)$$

$$\sum M_{cg2} = J_2\ddot{\psi}_2 = -C_{t_2}\dot{\psi}_2 - K_{t_2}\psi_2 + R_2F_{nx} \quad (25)$$

To find the eigenvalues using mathematical software (MathCAD™), the second order differential equations must be expanded to first order differential equations. The result is a 12 x 12 matrix of the form:

$$\begin{Bmatrix} \dot{X} \\ \ddot{X} \end{Bmatrix} = \begin{Bmatrix} 0 & I \\ -K/m & -C/m \end{Bmatrix} \begin{Bmatrix} X \\ \dot{X} \end{Bmatrix} \quad (26)$$

The undamped natural frequencies are purely imaginary eigenvalues and can be found by setting the damping coefficients to zero and solving for the eigenvalues of the matrix. The damped natural frequencies are the imaginary parts of the complex eigenvalues produced when the damping is included.

SIMPLIFIED SYSTEM CHECKS FOR EIGENVALUE SOLUTIONS

Several measures were taken to help establish credibility for the solutions obtained in the MathCAD^{TM} program. First, it was noted that the gear system would be analogous to the equivalent system of two disks connected by a flexible shaft when the bearing stiffness becomes very high and the external torsional stiffness acting on the gears is very low. In this model the gear tooth stiffness produces an equivalent torsional stiffness connecting the two gears.

The virtual flexible shaft has a torsional stiffness K_t which must be derived before the equivalent system can be of any use. $K_t = K_n R^2$, where K_n is the tooth stiffness and R is some unknown radius to be determined. The eigenvalues of the equivalent system are set equal to the eigenvalues of the gear pair.

$$\frac{K_n R^2 (J_1 + J_2)}{J_1 J_2} = \frac{K_n (R_1^2 J_2 - R_2^2 J_1)}{J_1 J_2} \quad \Rightarrow \quad R^2 = \frac{(R_1^2 J_2 + R_2^2 J_1)}{J_1 + J_2} \qquad (27)$$

$$\omega_n = \sqrt{K_n R^2 \cos^2(\alpha) \Big/ J_{eq}} \qquad (28)$$

This first check of the gear pair eigenvalues comes from (28) when the bearing stiffness becomes very large. It was expected that the torsional eigenvalue would approach this number as the bearing stiffness increases. Figure 14 shows that assumption to be correct when using the parameters in Table 1.

Table 1: Parameters for simplified system checks

m_1 = .0058 lb$_m$	R_1 = in	Kx=0..2000000 lb/in
m_2 = .0362 lb$_m$	R_2 = 2.5 in	Ky=Kx
K_t=0 in-lb/rad	Kn=10000 lb/in	

Figure 14: Plot of equivalent and actual eigenvalues versus lateral stiffness
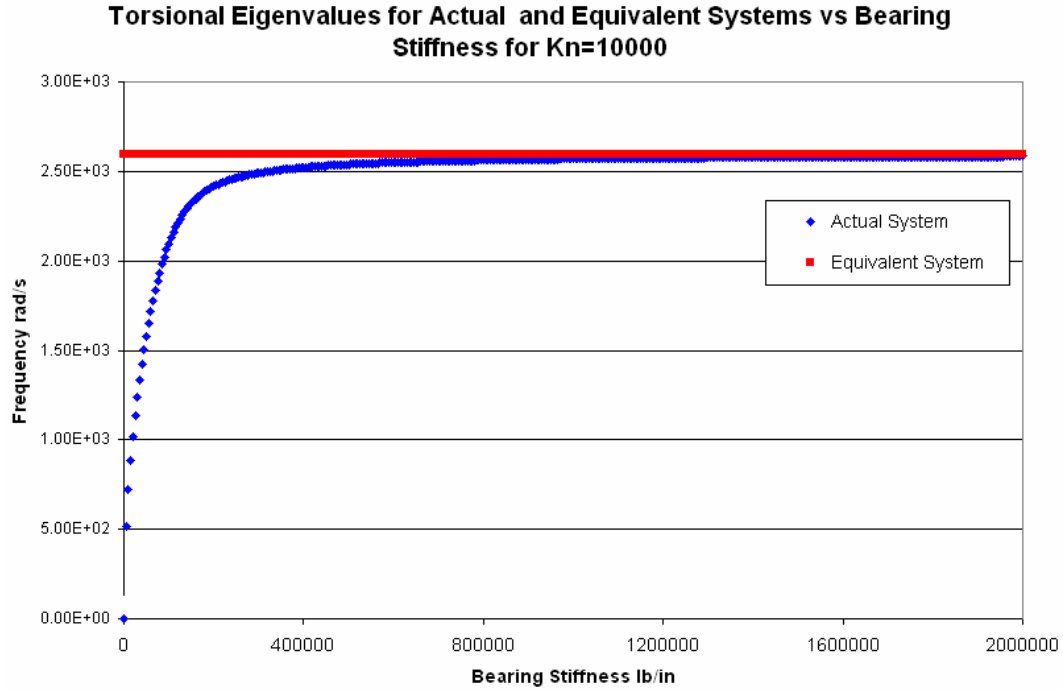
Further verification involved taking extreme values for the gear tooth pressure angles. When the pressure angle is set to 90 degrees with a high amount of tooth stiffness, the two gears will exhibit two modes along the line of centers and hence, two natural frequencies. The first natural frequency occurs when the two bodies move together in the same direction. During this case, the bodies can be converted into an equivalent mass-spring system. With this motion, the tooth stiffness does not come into play at all and the gears oscillate on the bearing springs. During the second scenario, the two bodies move in opposite directions and the tooth spring is considered working in parallel with the bearing springs. Therefore, the two natural frequencies that should be apparent in the MathCAD^{TM} eigenvalue solution are:

$$\omega_{lat_1} = \sqrt{\frac{2K_y}{m_1 + m_2}} \tag{29}$$

$$\omega_{lat_1} = \sqrt{\frac{(2K_y + K_n)(m_1 + m_2)}{m_1 m_2}} \tag{30}$$

Figure 15 and Figure 16 below confirm both of these cases, and lend more credibility to the eigenvalue solutions from the MathCAD ^{TM} 12x12 matrix.
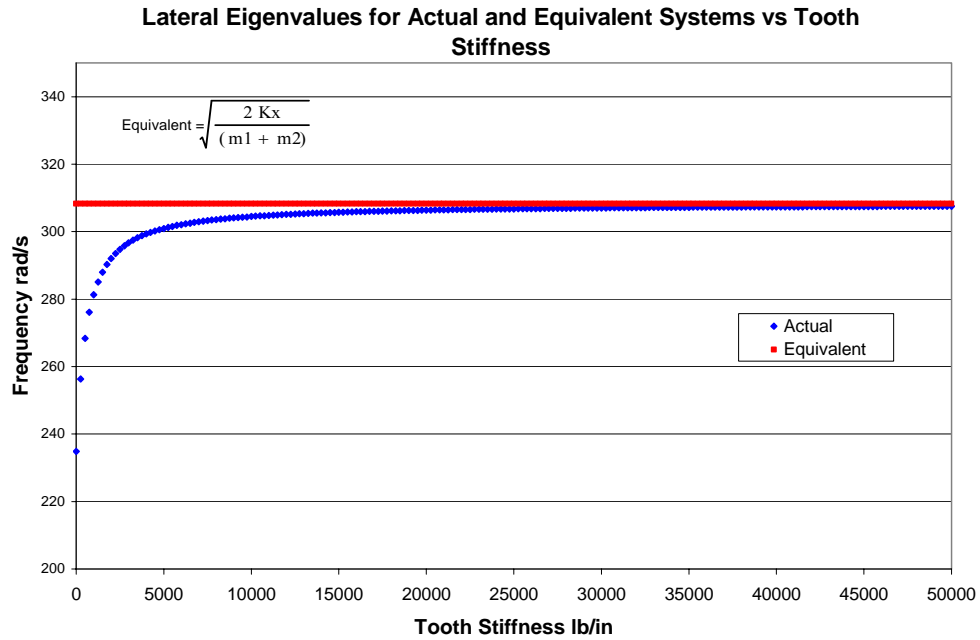

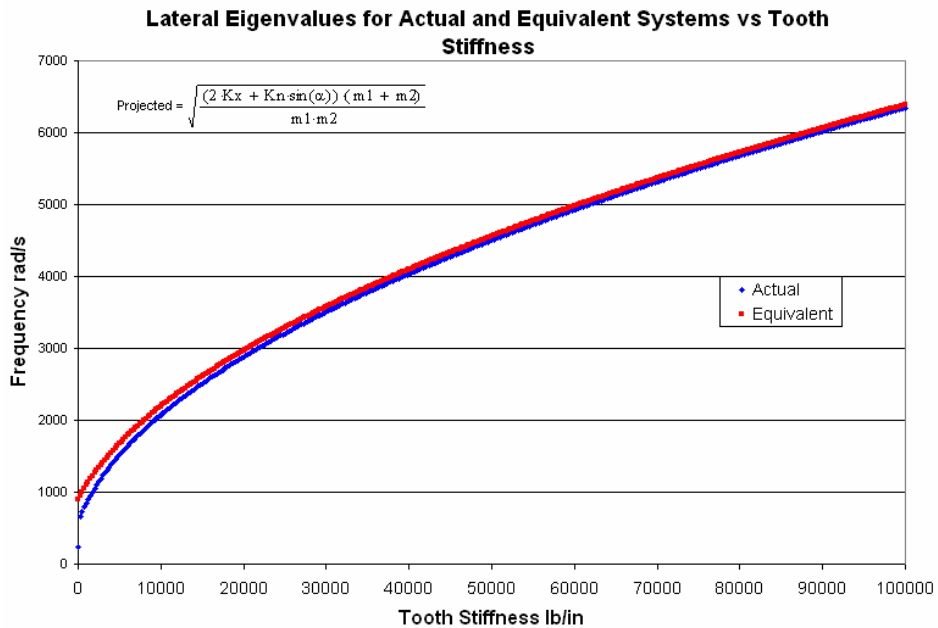**Figure 15:** Equivalent and actual system eigenvalues versus tooth stiffness for Kx=1000 and α =90

Figure 16: Plot of equivalent and actual system eigenvalues versus tooth stiffness for Kx=1000 and α =90

One interesting phenomenon occurs when the X and Y bearing stiffness components are equal. It appears as though the eigenvalues are independent of tooth stiffness. Furthermore, it appears that the eigenvalues are simply $\sqrt{K_x/m_n}$, which seems surprising. The mode shape from Figure 17 provides an answer to this problem:

	0	1	2	3	4	5
0	$5.395i \cdot 10^{-6}$	$-5.395i \cdot 10^{-6}$	$-5.826i \cdot 10^{-4}$	$5.826i \cdot 10^{-4}$	$1.473i \cdot 10^{-3}$	$-1.473i \cdot 10^{-3}$
1	$1.964i \cdot 10^{-6}$	$-1.964i \cdot 10^{-6}$	$1.601i \cdot 10^{-3}$	$-1.601i \cdot 10^{-3}$	$5.36i \cdot 10^{-4}$	$-5.36i \cdot 10^{-4}$
2	$1.079i \cdot 10^{-5}$	$-1.079i \cdot 10^{-5}$	0	0	$-1.305i \cdot 10^{-3}$	$1.305i \cdot 10^{-3}$
3	$-8.632i \cdot 10^{-7}$	$8.632i \cdot 10^{-7}$	0	0	$1.358i \cdot 10^{-4}$	$-1.358i \cdot 10^{-4}$
4	$-3.142i \cdot 10^{-7}$	$3.142i \cdot 10^{-7}$	0	0	$4.942i \cdot 10^{-5}$	$-4.942i \cdot 10^{-5}$
5	$-6.906i \cdot 10^{-7}$	$6.906i \cdot 10^{-7}$	0	0	$8.353i \cdot 10^{-5}$	$-8.353i \cdot 10^{-5}$

Figure 17: Sample eigenvector results from MathCAD^{TM} program

Taking a close look at the free body diagram, when the gears move normal to the line of action, they are free to move independently of tooth stiffness. To verify whether this explains the eigenvalues calculated by MathCAD^{TM}, the angle generated by the displacements in the X and Y direction were calculated. Setting $\theta=\tan^{-1}(Y/X)$, the 2nd and 4th mode shape exhibits an angle of 70 degrees. This agrees with the angle perpendicular to the pressure line and is the final piece of evidence that proves that the eigenvalue solutions are valid.

DEVELOPING HOMOGENEOUS EQUATIONS OF MOTION FOR AN
UNCOUPLED GEARED ROTOR SYSTEM

The uncoupled system shown in Figure 18 treats each gear as a separate rotor. The gear tooth stiffness is not considered in the development of the equations of motion. The key forces in the uncoupled model are the bearing spring and the bearing damping forces, along with the torsional shaft spring and torsional damping forces on the gears.
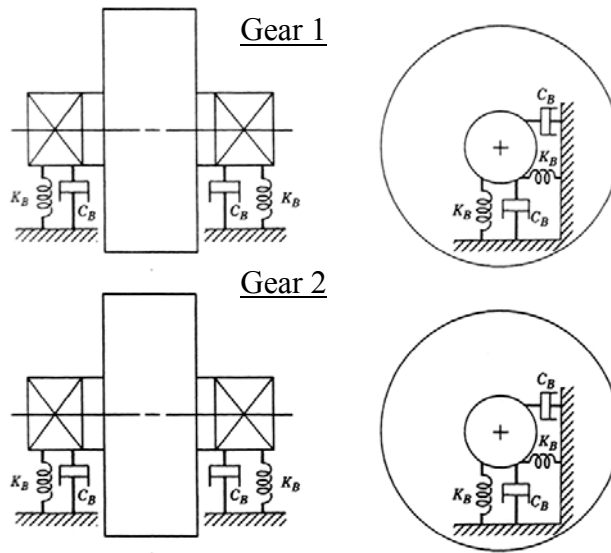
Figure 18: Uncoupled geared system [15]

Equations of Motion

$$\sum F_{x_1} = m_1 \ddot{X}_1 = -C_{xx_1} \dot{X}_1 - K_{xx_1} X_1 \tag{31}$$

$$\sum F_{y_1} = m_1 \ddot{Y}_1 = -C_{yy_1} \dot{Y}_1 - K_{yy_1} Y_1 \tag{32}$$

$$\sum M_{o_1} = J_1 \ddot{\psi}_1 = -C_{t_1} \dot{\psi}_1 - K_{t_1} \psi_1 \tag{33}$$

$$\sum F_{x_2} = m_2 \ddot{X}_2 = -C_{xx_2} \dot{X}_2 - K_{xx_2} X_2 \tag{34}$$

$$\sum F_{y_2} = m_2 \ddot{Y}_2 = -C_{yy_2} \dot{Y}_1 - K_{yy_2} Y_2 \tag{35}$$

$$\sum M_{o_2} = J_2 \ddot{\psi}_2 = -C_{t_2} \dot{\psi}_2 - K_{t_2} \psi_2 \tag{36}$$

The undamped natural frequencies are found by setting det(K-λI) equal to zero. Gathering the like stiffness, and mass terms forms a 6 x 6 diagonal matrix. By

definition, the eigenvalues of a diagonal matrix are found by solving each diagonal term independently.

$$\begin{bmatrix} -m_1\lambda^2+K_{xx_1} & 0 & 0 & 0 & 0 & 0 \\ 0 & -m_1\lambda^2+K_{yy_1} & 0 & 0 & 0 & 0 \\ 0 & 0 & -J_1\lambda^2+K_{t_1} & 0 & 0 & 0 \\ 0 & 0 & 0 & -m_2\lambda^2+K_{xx_2} & 0 & 0 \\ 0 & 0 & 0 & 0 & -m_2\lambda^2+K_{yy_2} & 0 \\ 0 & 0 & 0 & 0 & 0 & -J_2\lambda^2+K_{t_2} \end{bmatrix} \begin{Bmatrix} X_1 \\ Y_1 \\ \psi_1 \\ X_2 \\ Y_2 \\ \psi_2 \end{Bmatrix} = \begin{bmatrix} 0 \\ 0 \\ 0 \\ 0 \\ 0 \\ 0 \end{bmatrix} \quad (37)$$

$$\omega_{nX_1} = \sqrt{K_{xx_1}\big/m_1} \tag{38}$$

$$\omega_{nY_1} = \sqrt{K_{yy_1}\big/m_1} \tag{39}$$

$$\omega_{n\psi_1} = \sqrt{K_{t_1}\big/J_1} \tag{40}$$

$$\omega_{nX_2} = \sqrt{\frac{K_{xx_2}}{m_2}} \tag{41}$$

$$\omega_{nY_2} = \sqrt{K_{yy_2}\big/m_2} \tag{42}$$

$$\omega_{n\psi_2} = \sqrt{K_{t_2}\big/J_2} \tag{43}$$

The resulting natural frequencies suggest that the lateral natural frequencies are independent of the torsional stiffness from the shaft and that the torsional natural frequencies are independent of lateral stiffness from the bearings. Furthermore, the eigenvectors of a diagonal matrix result in mode shapes that are purely lateral and purely torsional.

DEVELOPING NONHOMOGENEOUS EQUATIONS OF MOTION FOR A SINGLE
GEAR PAIR ON FLEXIBLE SUPPORTS

For the purposes of this project, critical speeds are defined as speeds correlating with the peak amplitude of the forced response plot. Critical speeds are not exactly the same as the eigenvalues when damping exists, as damping moves the response peaks to a higher frequency. The second order differential equations are no longer homogenous when the center of mass is moved away from the center of the gear (Figure 19). This rotating imbalance generates harmonic forces that can be derived from the kinematic constraints which define the position and acceleration of the center of mass.
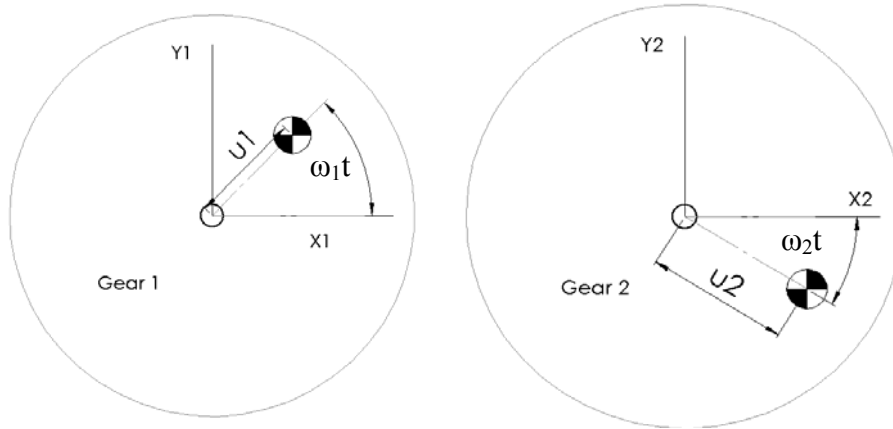
Figure 19: Location of the center of mass for Gear 1 (right) and Gear 2 (left)

Gear 1:

$$X_{1g} = X_1 + u_1 \cos(\omega_1 t) \tag{44}$$

$$\ddot{X}_{1g} = \ddot{X}_1 - u_1 \omega^2 \cos(\omega_1 t) \tag{45}$$

$$Y_{1g} = Y_1 + u_1 \sin(\omega_1 t) \tag{46}$$

$$\ddot{Y}_{1g} = \ddot{Y}_1 - u_1 \omega^2 \sin(\omega_1 t) \tag{47}$$

Re-writing the force equations:

$$\sum F_{x_1} = m_1 \ddot{X}_{1g} = -C_{xx_1} \dot{X}_1 - K_{xx_1} X_1 - F_{nx} \tag{48}$$

$$\sum F_{y_1} = m_1 \ddot{Y}_{1g} = -C_{yy_1} \dot{Y}_1 - K_{yy_1} Y_1 - F_{ny} \tag{49}$$

Plugging in definitions for X_{1g} and Y_{1g}:

$$m_1 \ddot{X}_1 + C_{xx_1} \dot{X}_1 + K_{xx_1} X_1 + F_{nx} = m_1 u_1 \omega^2 \cos(\omega_1 t) \tag{50}$$

$$m_1 \ddot{Y}_1 + C_{yy_1} \dot{Y}_1 + K_{yy_1} Y_1 + F_{ny} = m_1 u_1 \omega^2 \sin(\omega_1 t) \tag{51}$$

Gear 2:

$$X_{2g} = X_2 + u_2 \cos(\omega_2 t) \tag{52}$$

$$\ddot{X}_{2g} = \ddot{X}_2 - u_2 \omega^2 \cos(\omega_2 t) \tag{53}$$

$$Y_{2g} = Y_2 - u_2 \sin(\omega_2 t) \tag{54}$$

$$\ddot{Y}_{2g} = \ddot{Y}_2 + u_2 \omega^2 \sin(\omega_2 t) \tag{55}$$

Re-writing the force equations:

$$\sum F_{x2} = m_2 \ddot{X}_{2g} = -C_{xx_2} \dot{X}_2 - K_{xx_2} X_2 + F_{nx} \tag{56}$$

$$\sum F_{y2} = m_2 \ddot{Y}_{2g} = -C_{yy_2} \dot{Y}_2 - K_{yy_2} Y_2 + F_{ny} \tag{57}$$

Plugging in definitions for X_{1g} and Y_{1g}:

$$m_2 \ddot{X}_2 + C_{xx_2} \dot{X}_2 + K_{xx_2} X_2 - F_{nx} = m_2 u_2 \omega^2 \cos(\omega_2 t) \tag{58}$$

$$m_2 \ddot{Y}_2 + C_{yy_2} \dot{Y}_2 + K_{yy_2} Y_2 - F_{ny} = -m_2 u_2 \omega^2 \sin(\omega_2 t) \tag{59}$$

Equations (50)-(58) are second order non-homogeneous ordinary linear differential equations with constant coefficients and can be solved by the method of undetermined coefficients. Noting that $e^{i\omega t}$ can be re-written as:

$$e^{i\omega t} = \cos(\omega t) + i \sin(\omega t) \tag{60}$$

Note that $cos(\omega t)$ and $sin(\omega t)$ can be re-written to represent the real part of (60) by multiplying $e^{i\omega t}$ by $(^+/-)1$ or $(^+/-)\ i$.

This allows differential equations to be written in exponential form.

$$m_1\ddot{X}_1 + C_{xx_1}\dot{X}_1 + K_{xx_1}X_1 + F_{nx} = m_1 u_1 \omega^2 e^{i\omega t} \tag{61}$$

$$m_2\ddot{X}_2 + C_{xx_2}\dot{X}_2 + K_{xx_2}X_2 - F_{nx} = m_2 u_2 \omega^2 e^{i\omega t} \tag{62}$$

$$m_1\ddot{Y}_1 + C_{yy_1}\dot{Y}_1 + K_{yy_1}Y_1 + F_{ny} = -i m_1 u_1 \omega^2 e^{i\omega t} \tag{63}$$

$$m_2\ddot{Y}_2 + C_{yy_2}\dot{Y}_2 + K_{yy_2}Y_2 - F_{ny} = i m_2 u_2 \omega^2 e^{i\omega t} \tag{64}$$

Using the method of undetermined coefficients, with the assumed solution $Xe^{i\omega t}$ the differential equations become:

$$(-m_1\omega^2 + iC_{xx_1}\omega + K_{xx_1})\overline{X}_1 e^{i\omega t} = m_1 u_1 \omega^2 e^{i\omega t} \tag{65}$$

$$(-m_1\omega^2 + iC_{yy_1}\omega + K_{yy_1})\overline{Y}_1 e^{i\omega t} = -i m_1 u_1 \omega^2 e^{i\omega t} \tag{66}$$

$$(-J_1\omega^2 + i\omega C_{t_1} + K_{t_1})\overline{\psi}_1 e^{i\omega t} = 0 \tag{67}$$

$$(-m_2\omega^2 + i\omega C_{xx_2} + K_{xx_2})\overline{X}_2 e^{i\omega t} = m_2 u_2 \omega^2 e^{i\omega t} \tag{68}$$

$$(-m_2\omega^2 + i\omega C_{yy_2} + K_{yy_2})\overline{Y}_2 e^{i\omega t} = i m_2 u_2 \omega^2 e^{i\omega t} \tag{69}$$

$$(-J_1\omega^2 + i\omega C_{t_1} + K_{t_1})\overline{\psi}_2 e^{i\omega t} = 0 \tag{70}$$

The same procedure is performed on the variables in the tooth mesh force equations. After inserting the coefficients from the assumed solution and grouping the like terms, the equations of motion can be placed in a 6 x 6 matrix:

A=

$$
\begin{array}{lll}
K_n\cos^2(\alpha)+K_{xx1}-m_1\omega^2+iC_{xx_1}\omega & K_n\sin(\alpha) & K_nR_1\cos^2(\alpha) \\
K_n\cos(\alpha)\sin(\alpha) & K_n\sin^2(\alpha)+K_{yy1}-m_1\omega^2+iC_{yy_1}\omega & K_nR_1\cos(\alpha)\sin(\alpha) \\
K_n\cos^2(\alpha)R_1 & K_n\sin(\alpha)R_1 & K_nR_1^2\cos^2(\alpha)+K_t-J_2\omega^2+iC_t\omega \ \cdots \\
-K_n\cos^2(\alpha) & -K_n\sin(\alpha) & -K_nR_1\cos^2(\alpha) \\
-K_n\cos(\alpha)\sin(\alpha) & -K_n\sin^2(\alpha) & -K_nR_1\cos(\alpha)\sin(\alpha) \\
-K_n\cos^2(\alpha)R_2 & -K_n\sin(\alpha)R_2 & -K_nR_1R_2\cos^2(\alpha)
\end{array}
$$

$$
\begin{array}{lll}
-K_n\cos^2(\alpha) & -K_n\sin(\alpha)\cos(\alpha) & -K_nR_2\cos^2(\alpha) \\
-K_n\cos(\alpha)\sin(\alpha) & -K_n\sin^2(\alpha) & -K_nR_2\cos(\alpha)\sin(\alpha) \\
\cdots \ -K_nR_1\cos^2(\alpha) & -K_nR_1\sin(\alpha)\cos(\alpha) & -K_nR_1R_2\cos^2(\alpha) \\
K_n\cos^2(\alpha)+K_{xx2}-m_2\omega^2+iC_{xx_2}\omega & K_n\sin(\alpha)\cos(\alpha) & K_nR_2\cos^2(\alpha) \\
K_n\cos(\alpha)\sin(\alpha) & K_n\sin^2(\alpha)+K_{yy2}-m_2\omega^2+iC_{yy_2}\omega & K_nR_2\cos(\alpha)\sin(\alpha) \\
K_nR_2\cos^2(\alpha) & K_nR_2\sin(\alpha)\cos(\alpha) & K_nR_2^2\cos^2(\alpha)+K_t-J_2\omega^2+iC_t\omega
\end{array}
\tag{71}
$$

$$
\overline{X}=\begin{bmatrix}\overline{X}_1\\ \overline{Y}_1\\ \overline{\psi}_1\\ \overline{X}_2\\ \overline{Y}_2\\ \overline{\psi}_2\end{bmatrix}
\qquad
b=\begin{bmatrix}m_1\omega_1^2u_1\\ -im_1\omega_1^2u_1\\ 0\\ m_2\omega_2^2u_2\\ im_2\omega_2^2u_2\\ 0\end{bmatrix}
\tag{72}
$$

The matrix equation now takes on the form $A\overline{X}=b$, where A is the 6 x 6 matrix, $\overline{X}$ is the complex amplitude, and b is the column vector containing the right hand side of the equation. The amplitude of the steady state response is calculated by setting $\overline{X}=A^{-1}b$, where the solution is a complex column vector. The real amplitude is simply the magnitude of each row in the column vector.

Since the excitation forces are at separate frequencies, another important concept that must be used is the rule of superposition. In this case, two external forces (from

unbalance of Gear 1 and unbalance of Gear 2) act on the gears. The amplitudes from Case 1 (no unbalance on Gear 2) must be added to Case 2 (no unbalance on Gear 1), whose sum is the total amplitude used in the forced response plot.

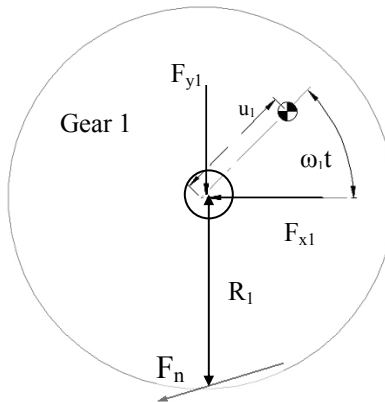## THE ROTATING MOMENT ARM AND ITS EFFECTS ON CRITICAL SPEEDS

Figure 20: Gear 1 system sketch with rotating moment arm

Figure 20 shows that the perpendicular distance of the moment arm (from the bearings and tooth forces to the center of mass) changes with time as the center of gravity of the gear rotates about the geometric center. Thus far, it has been assumed that the effects of this rotating moment arm on the system dynamics were negligible. However, closer examination of this phenomenon suggests this assumption may not be valid for gears with large unbalances. With the varying moment arm included, the assumed solutions to the forced response equations are no longer valid since the coefficients in the matrix are no longer constants.

Also, the right-hand side (RHS) of the moment equations treats the moments generated by the unbalance moment arm as a forced excitation. This produced non-constant coefficients in the moment equations. The right-hand side of the equation of each moment equation becomes:

$$J_1\ddot{\psi}_1 + C_{t_1}\dot{\psi}_1 + K_{t_1}\psi_1 = -\{K_n[(X_1 - X_2)\cos(\alpha) + (Y_1 - Y_2)\sin(\alpha) + ...$$
$$...(R_1\psi_1 - R_2\psi_2)\cos(\alpha)]\cos(\alpha) + K_{xx1}X_1 + C_{xx1}\dot{X}_1\} \cdot (R_1 + u_1\sin(\omega_1 t)) + ...$$
$$...\{K_n[(X_1 - X_2)\cos(\alpha) + (Y_1 - Y_2)\sin(\alpha) + (R_1\psi_1 - R_2\psi_2)\cos(\alpha)]\sin(\alpha) + ...$$
$$...K_{yy1}Y_1 + C_{yy1}\dot{Y}_1\} \cdot u_1\cos(\omega_1 t)$$

(73)

$$J_2\ddot{\psi}_2 + C_{t_2}\dot{\psi}_2 + K_{t_2}\psi_2 = \{K_n[(X_1 - X_2)\cos(\alpha) + (Y_1 - Y_2)\sin(\alpha) + ...$$
$$...(R_1\psi_1 - R_2\psi_2)\cos(\alpha)]\cos(\alpha) - K_{xx2}X_2 - C_{xx2}\dot{X}_2\} \cdot (R_2 + u_2\sin(\omega_2 t)) + ...$$
$$...\{K_n[(X_1 - X_2)\cos(\alpha) + (Y_1 - Y_2)\sin(\alpha) + (R_1\psi_1 - R_2\psi_2)\cos(\alpha)]\sin(\alpha) - ...$$
$$...K_{yy2}Y_2 - C_{yy2}\dot{Y}_2\} \cdot u_2\cos(\omega_2 t)$$

(74)

Since the state variables are multiplied by $\cos(\omega_1 t)$ and $\sin(\omega_1 t)$ in the RHS of the equation, these terms suggest that second order harmonic vibration will be present. The simplified version of this problem shows where these 2nd order harmonics appear. The variable moment arm is treated as an excitation force and is moved to the right-hand side of the equation.

$$I\ddot{\psi} + C(R_1 + u\cos(\omega t))\dot{\psi} + K(R_1 + u\cos(\omega t))\psi = 0$$
$$I\ddot{\psi} + CR_1\dot{\psi} + KR_1\psi = -u\cos(\omega t)\dot{\psi} - u\cos(\omega t)\psi$$

(75)

The solution to the differential equation cannot be assumed to be of the form $e^{i\omega t}$ and the method of undetermined coefficients cannot be used to solve the differential equation. That assumed solution causes a 2nd order harmonic to appear on the RHS of the equation, while only a 1st order harmonic appears on the left-hand side. This makes a traditional solution to the forced response problem impossible.

$$I\ddot{\psi} + CR_1\dot{\psi} + KR_1\psi = -\omega\dot{\psi}ue^{i\omega t} - u\psi e^{i\omega t}$$
$$(-I\omega^2 + iCR_1\omega + KR_1)\bar{\psi}e^{i\omega t} = -i\omega^2\bar{\psi}e^{i\omega t}ue^{i\omega t} - u\bar{\psi}e^{i\omega t}e^{i\omega t}$$
$$(-I\omega^2 + iCR_1\omega + KR_1)\bar{\psi}e^{i\omega t} = -i\omega^2 u\bar{\psi}e^{i2\omega t} - u\bar{\psi}e^{i2\omega t}$$

(76)

The differential equations of motion can be solved using the Runge-Kutta numerical method with the initial conditions taken from the original forced response plots.

The initial displacement and velocity for each of the degrees of freedom are the initial conditions needed for the Runge-Kutta method. Runge-Kutta requires the system to be decomposed into a first order differential equation using the following procedure.

Setting:

$$x_1 = X_0 \qquad y_1 = X_2 \qquad \psi_1 = X_4 \qquad x_2 = X_6 \qquad y_2 = X_8 \qquad \psi_2 = X_{10}$$
$$\dot{x}_1 = X_1 \qquad \dot{y}_1 = X_3 \qquad \dot{\psi}_1 = X_5 \qquad \dot{x}_2 = X_7 \qquad \dot{y}_2 = X_9 \qquad \dot{\psi}_2 = X_{11}$$
$$\ddot{x}_1 = \dot{X}_1 \qquad \ddot{y}_1 = \dot{X}_3 \qquad \ddot{\psi}_1 = \dot{X}_5 \qquad \ddot{x}_2 = \dot{X}_7 \qquad \ddot{y}_2 = X_9 \qquad \ddot{\psi}_2 = \dot{X}_{11}$$

A column vector is formed from the variables used in the reduction of order process. The final rows of the resulting column vector are shown below:

$$R_1 = X_1 \tag{77}$$

$$R_2 = \frac{1}{m_1}\left(\begin{array}{l} m_1(X_{12})^2 u_1\cos(X_{12}t)-(K_{xx_1}+K_n\cos^2(\alpha))X_0-K_n\sin(\alpha)\cos(\alpha)(X_2-X_8) \\ ...-K_n\cos^2(\alpha)(R_1X_4-R_2X_{10})+K_n\cos^2(\alpha)X_6-C_{xx_1}X_1 \end{array} \right) \tag{78}$$

$$R_3 = X_3 \tag{79}$$

$$R_4 = \frac{1}{m_1}\left(\begin{array}{l} m_1(X_{12})^2 u_1\sin(X_{12}t)-(K_{yy_1}+K_n\sin^2(\alpha))X_2-K_n\sin(\alpha)\cos(\alpha)(X_0-X_6) \\ ...-K_n\sin(\alpha)\cos(\alpha)(R_1X_4-R_2X_{10})+K_n\sin^2(\alpha)X_8-C_{yy_1}X_3 \end{array} \right) \tag{80}$$

$$R_5 = X_5 \tag{81}$$

$$R_6 = \frac{1}{J_1}\left(\begin{array}{l} -(K_{xx_1}X_0+C_{xx_1}X_1)u_1\sin(X_{12}t)+(K_{yy_1}X_2+C_{yy_1}X_3)u_1\cos(X_{12}t)-K_tX_4-C_tX_5- \\ ...\left(\begin{array}{l}(K_n\cos^2(\alpha))(X_0-X_6)+K_n\sin(\alpha)\cos(\alpha)(X_2-X_8)+ \\ ...K_n\cos^2(\alpha)(R_1X_4-R_2X_{10})\end{array}\right)(u_1\sin(X_{12}t)+R_1)+ \\ ...\left(\begin{array}{l}(K_n\sin^2(\alpha))(X_2-X_8)+K_n\sin(\alpha)\cos(\alpha)(X_0-X_6)+ \\ ...K_n\sin(\alpha)\cos(\alpha)(R_1X_4-R_2X_{10})\end{array}\right)u_1\cos(X_{12}t) \end{array} \right) \tag{82}$$

$$R_7 = X_7 \tag{83}$$

$$R_8 = \frac{1}{m_2} \left(\begin{array}{l} m_2(\frac{R_1}{R_2}X_{12})^2 u_2 \cos(\frac{R_1}{R_2}X_{12}t) - (K_{xx_2} + K_n \cos^2(\alpha))X_6 + \\ ...K_n \sin(\alpha)\cos(\alpha)(X_2 - X_8) + K_n \cos^2(\alpha)(R_1X_4 - R_2X_{10}) \\ ...K_n \cos^2(\alpha)X_0 - C_{xx_2}X_7 \end{array} \right) \tag{84}$$

$$R_9 = X_9 \tag{85}$$

$$R_{10} = \frac{1}{m_2} \left(\begin{array}{l} m_1(\frac{R_1}{R_2}X_{12})^2 u_2 \sin(\frac{R_1}{R_2}X_{12}t) - (K_{yy_2} + K_n \sin^2(\alpha))X_8 + \\ ...K_n \sin(\alpha)\cos(\alpha)(X_0 - X_6) + K_n \sin(\alpha)\cos(\alpha)(R_1X_4 - R_2X_{10}) + \\ ...K_n \sin^2(\alpha)X_2 - C_{yy_2}X_9 \end{array} \right) \tag{86}$$

$$\text{Row } 11 = X_{11} \tag{87}$$

$$R_{12} = \frac{1}{J_2} \left(\begin{array}{l} -(K_{xx_2}X_6 + C_{xx_2}X_7)u_1 \sin(\frac{R_1}{R_2}X_{12}t) - (K_{yy_2}X_8 + C_{yy_2}X_9)u_1 \cos(\frac{R_1}{R_2}X_{12}t) - \\ ...K_{t_2}X_{10} - C_{t_2}X_{11}... \\ ...\left(\begin{array}{l} (K_n \cos^2(\alpha))(X_0 - X_6) + K_n \sin(\alpha)\cos(\alpha)(X_2 - X_8) \\ ...+ K_n \cos^2(\alpha)(R_1X_4 - R_2X_{10}) \end{array} \right) (u_2 \sin(\frac{R_1}{R_2}X_{12}t) + \\ ...\left(\begin{array}{l} (K_n \sin^2(\alpha))(X_2 - X_8) + K_n \sin(\alpha)\cos(\alpha)(X_0 - X_6) \\ ...+ K_n \sin(\alpha)\cos(\alpha)(R_1X_4 - R_2X_{10}) \end{array} \right) u_2 \cos(\frac{R_1}{R_2}X_{12}t) \end{array} \right) \tag{88}$$

$$R_{13} = 0 \tag{89}$$

MathCAD^{TM} and other mathematic software requires that the column vector is a function of time and X alone. This causes difficulties since the system is also a function of running speed (ω). The workaround to this problem is to include an additional zero row to the D(t,x) matrix (Row 13) and define ω as X_{12}. In addition, a row is added to the initial condition matrix which is where ω is varied.

The vibration of the system is described by a cosine wave, with a phase angle φ. The amplitude of vibration wave is the magnitude of the complex amplitude from the forced response plot. The phase angle is found using the inverse tangent of the imaginary part over the real part of the complex amplitude. The displacement and velocity at time = 0 now becomes:

$$Displacement = |amp_n|\cos(-\varphi_n) \tag{90}$$

$$Velocity = -|amp_n|\omega\sin(-\varphi_n) \tag{91}$$

A Fast Fourier Transform (FFT) of the solutions to the differential equation would confirm the existence of second order harmonic vibrations. However, since the FFT only gives solutions in terms of one running speed at a time, a range of running speeds was used to build a waterfall plot. This offers a better representation of what occurs in the system as the running speed increases. The system parameters were modified to lower eigenvalues to allow for reasonable computational running times.

IV. RESULTS

COMPARISON OF COUPLED AND UNCOUPLED SYSTEMS WITH SYMMETRIC
SUPPORTS

Table 2: Parameters for system with symmetric supports

$m1 = .1451 \ lb_m$	R1 = 5 in	Kx=50000 lb/in	0<Kt<2000000 in-lb/rad
$m2 = .9068 \ lb_m$	R2 = 12.5 in	Ky=Kx	

Figure 21 shows the natural frequencies of the uncoupled system and Figure 22 shows
the natural frequencies of the coupled system with symmetric supports. Both results
were found using the parameters listed in Table 2. Note: The sixth mode in the coupled
system does not appear in the graph because the frequency is several magnitudes higher
than the first five modes. One immediate disparity between the two systems is that the
coupled system contains five natural frequencies, while the uncoupled system shows
only four. Using an uncoupled model for the coupled system may result in missing a
natural frequency entirely.
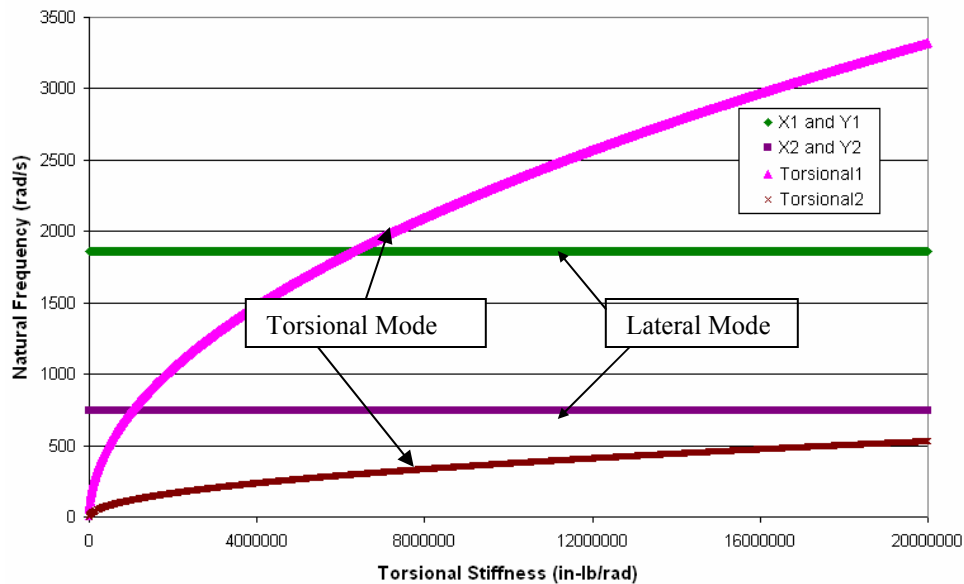
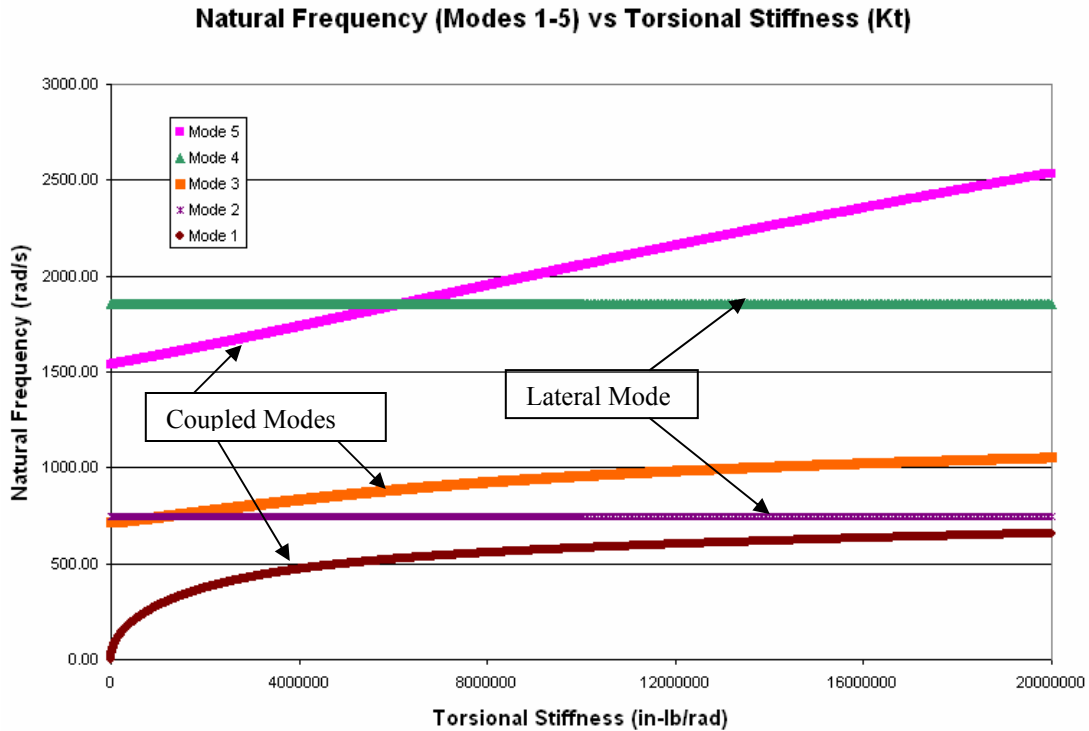**Figure 21:** Natural frequencies of the uncoupled system

Figure 22: Natural frequencies of the coupled system

The torsional-lateral coupling in the gear pair can be seen by varying the stiffness parameters. Figure 22 shows how increasing torsional stiffness of the shaft affects the undamped natural frequencies of the coupled system. Each of these modes involves significant lateral motion (at least 10 percent compared to torsional vibration). The modes have been labeled corresponding with their placement at high torsional stiffness values. Two natural frequencies are independent of the torsional stiffness parameter. These eigenvalues correspond to the vibration mode perpendicular to the line of action, and are the uncoupled degree of freedom used in Iwatsubo [4] and Kahraman [11]. The natural frequencies of Modes 1, 3, and 5 suggests the existence of a strong torsional lateral coupling.

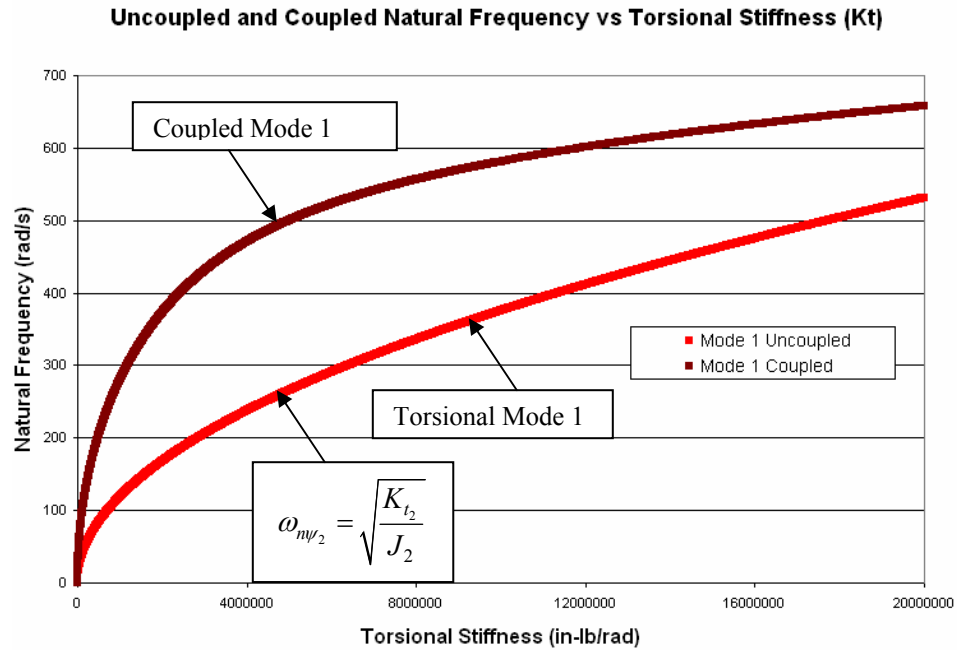*Mode 1: The Lowest Coupled Natural Frequency*

Uncoupled and Coupled Natural Frequency vs Torsional Stiffness (Kt)

Coupled Mode 1

Torsional Mode 1

$$\omega_{n\psi_2} = \sqrt{\frac{K_{t_2}}{J_2}}$$

- Mode 1 Uncoupled
- Mode 1 Coupled

Natural Frequency (rad/s)

Torsional Stiffness (in-lb/rad)

Figure 23: Mode 1 natural frequencies of coupled and uncoupled systems

Figure 23 compares the lowest uncoupled torsional natural frequency with the lowest coupled natural frequency.   Though the difference between the two natural frequencies seems to narrow as the torsional stiffness becomes very large, Figure 24 shows that the 1st mode in the coupled case is heavily dependent on the bearing support stiffness as well.

Mode 1 Natural Frequency vs Torsional Stiffness (Kt)
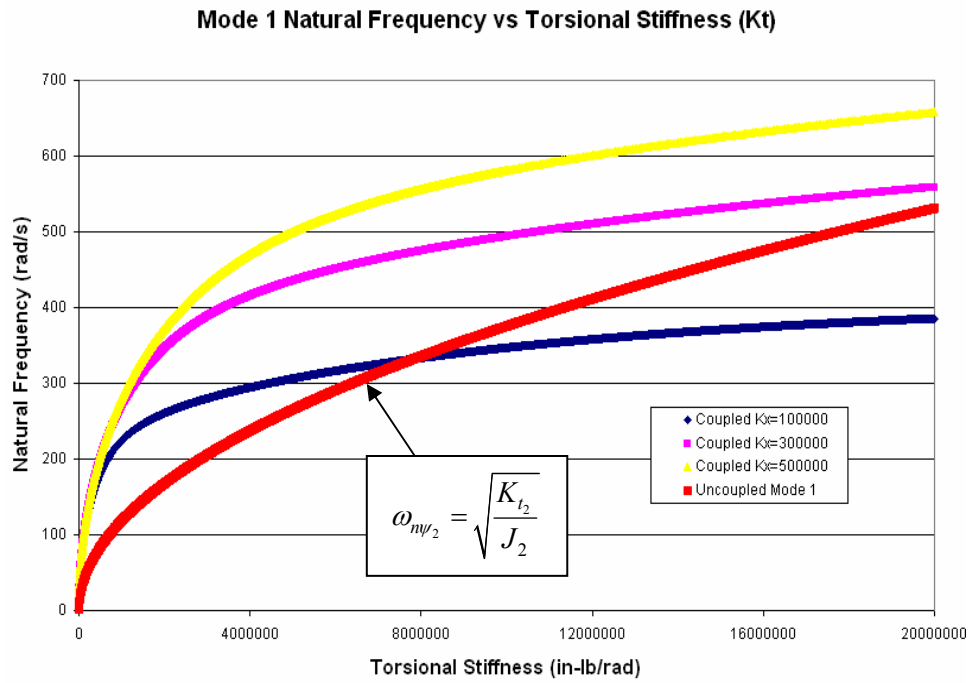
Figure 24: Changes in Mode 1 natural frequencies for various support stiffness values with increasing torsional stiffness

Mode 1 Natural Frequency and Mode Shape vs Torsional Stiffness (Kt)
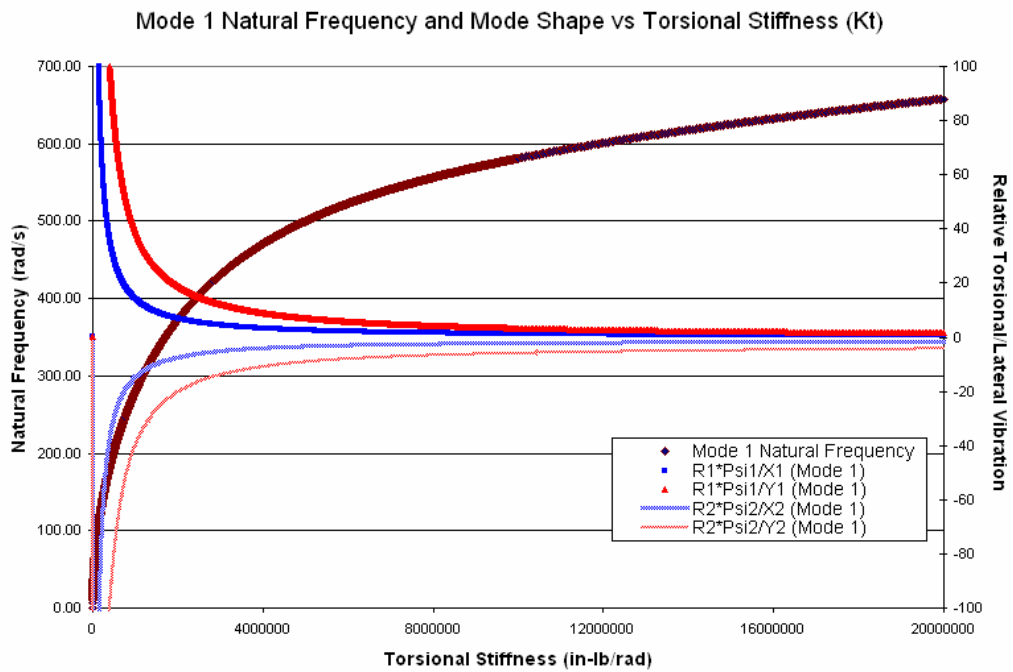
Figure 25: Undamped natural frequency and mode shape (Mode 1) as a function of torsional stiffness Kt

The first mode shape calculated of the uncoupled model is pure torsional vibration with no lateral motion. For the coupled model, Figure 25 shows the relative amplitude of torsional vibration compared to lateral amplitudes of Gear 1 and Gear 2. The initial mode shape is highly torsional at low torsional flexibilities, but the ratio of torsional vibration amplitude to lateral vibration amplitude decreases exponentially as the torsional stiffness is increased. At high torsional stiffness, the vibration seen in either gear is dominated by lateral vibrations. Based on the eigenvalue and eigenvector results for this particular mode, the uncoupled equations of motion would not accurately predict the system's torsional natural frequency or mode shape. Note, however, from Figure 22, that with very high torsional stiffness, the mode becomes predominantly lateral, and this natural frequency may coincide with the natural frequency of Mode 2.

Modes 2 and 4: Lateral Modes for Coupled and Uncoupled Models
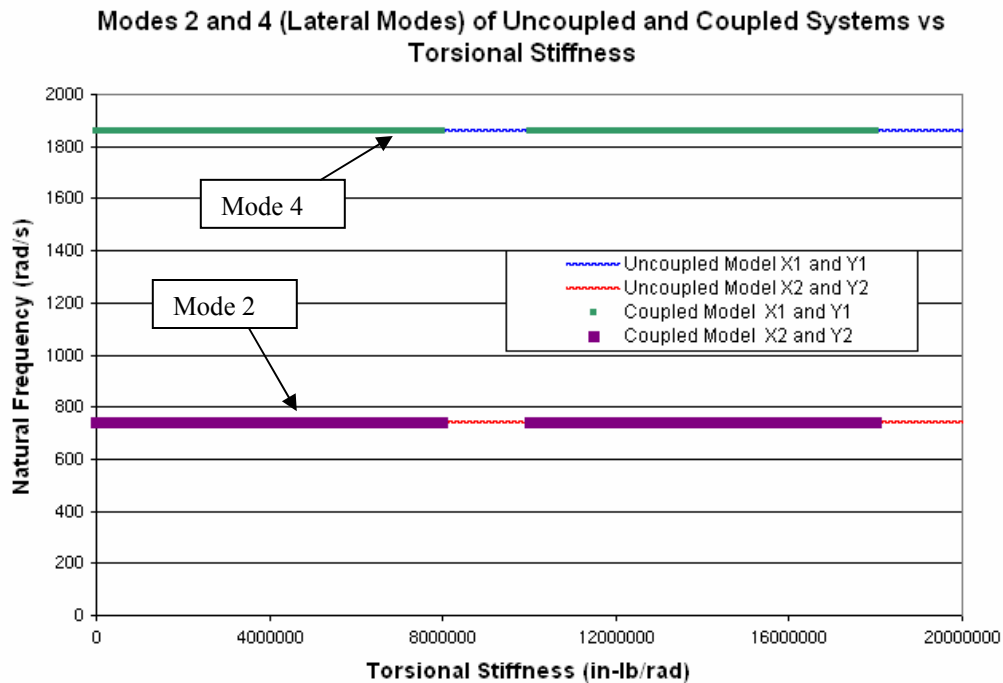
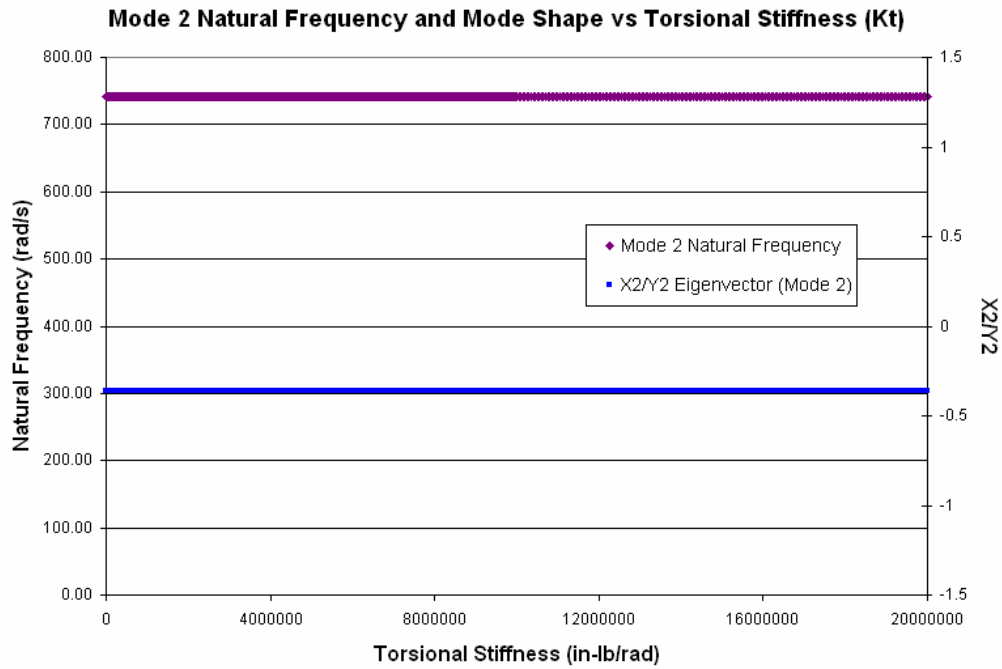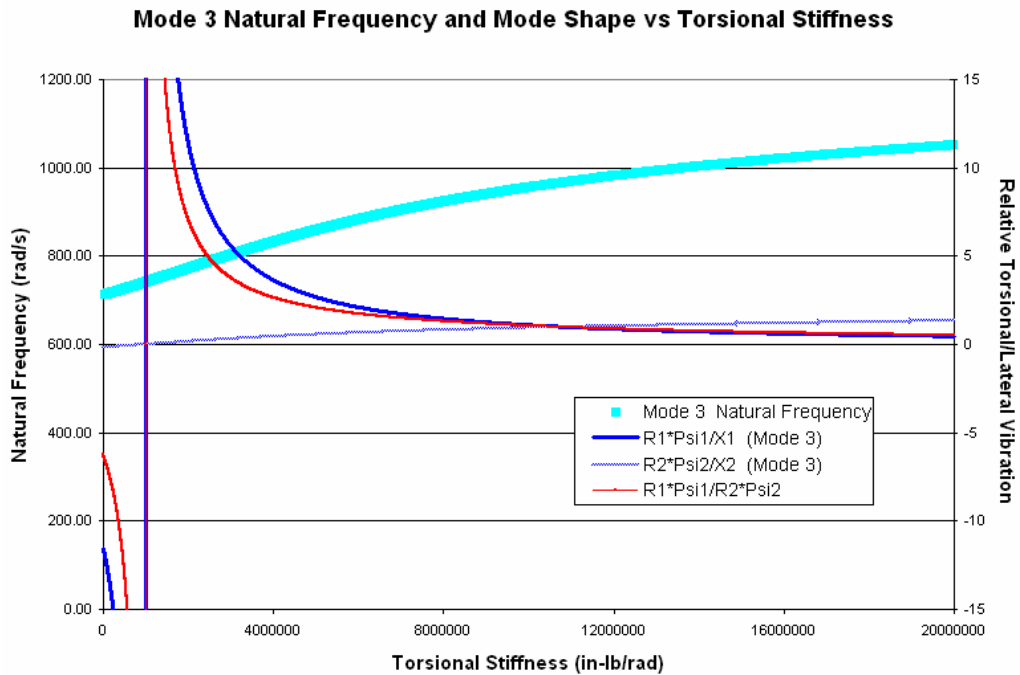**Figure 26:** Lateral natural frequencies of coupled and uncoupled systems

Figure 27: Undamped natural frequency and mode shape (Mode 2) as a function of torsional stiffness Kt

However, some of the uncoupled lateral natural frequencies favorably match the natural frequencies of the coupled system. In particular, the lateral natural frequencies shown in Figure 26 perfectly match those of the coupled system. The coupled motion is normal to the line of action. In this case, with symmetric bearing stiffness, using the coupled approximation may be acceptable for some lateral natural frequency calculations

Figure 27 shows that no torsional vibration exists at the natural frequencies for Modes 2 and 4. The vibration of these natural frequencies occurs perpendicular to the line of action and can be calculated using $\sqrt{K_x/m_n}$. This result suggests that at least two natural frequencies of lateral vibration can be calculated using uncoupled equations of motion in cases where the overall bearing support stiffness are symmetric.

Mode 3: The Second Coupled Mode

Figure 28: Undamped natural frequency and mode shape (Mode 3) as a function of torsional stiffness Kt

Mode 3 does not appear in the uncoupled natural frequency calculations. Figure 28 shows a peak in the relative torsional vibration for Gear 1 using the coupled system. At this point, vibration in the lateral X1 and Y1 direction goes to zero leaving $R_1\psi_1$ as the only source of vibration in Gear 2. Torsional vibration dominates with low values of K_t, though significant lateral vibration (over 10%) begins as K_t is further stiffened. The relative motion $R_2\psi_2/X_2$ vibrates out of phase with low values of K_t, but in phase at higher stiffness values. The point on the graph where Gear 2 vibrates laterally, with no torsional vibration coincides with the peak torsional response of Gear 1.

Eigenvector Analysis of Mode 3

The relative amplitude seen between $R_1\psi_1$ and X_1 as well as the relative amplitudes of torsional vibration is shown in Figure 29 as a function of torsional stiffness. The importance of torsional dynamics increases as the dominance of the torsional mode over the lateral mode increases. The gears initially vibrate out of phase, but at some point as the torsional stiffness is increase, they begin vibrating in phase to each other. At the same point in Figure 29 the relative vibration in the X_1 direction becomes zero as it changes signs and vibrates in phase with the torsional degree of freedom. The amount of torsional stiffness required to make this spike depends strongly on the lateral support stiffness, as well as gear ratios. Figure 30 shows how the stiffness ratio required to produce the spike moves as a function of gear ratios. The radius of Gear 2 has been held constant while varying the radius of Gear 1.
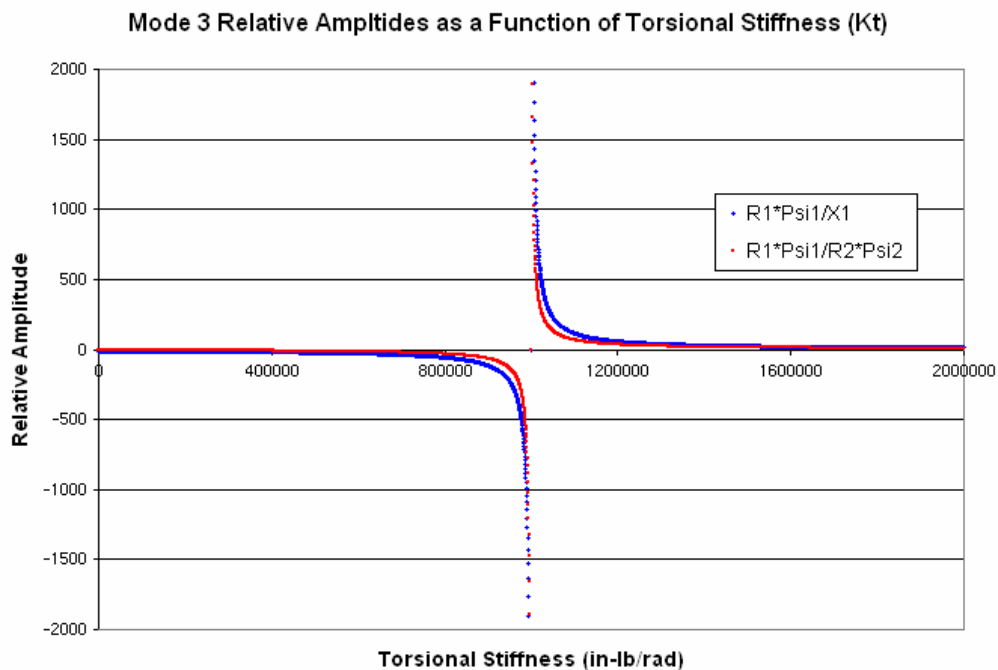
Figure 29: Change in vibration ratio between Phi1 and X1 as torsional stiffness is increased
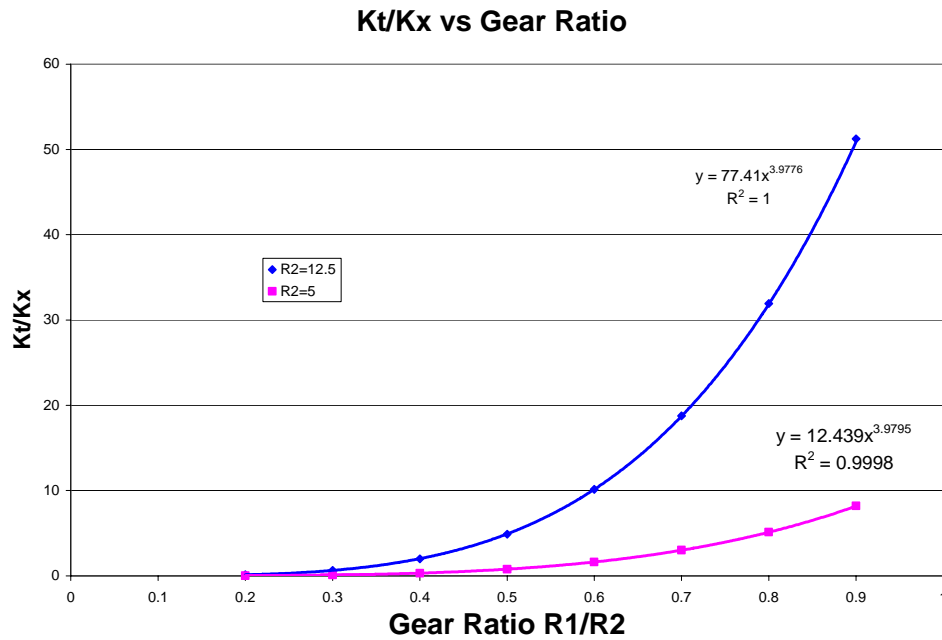
Kt/Kx vs Gear Ratio

Figure 30: Plot of the relative torsional stiffness/support stiffness vs. gear ratio for torsional vibration spike
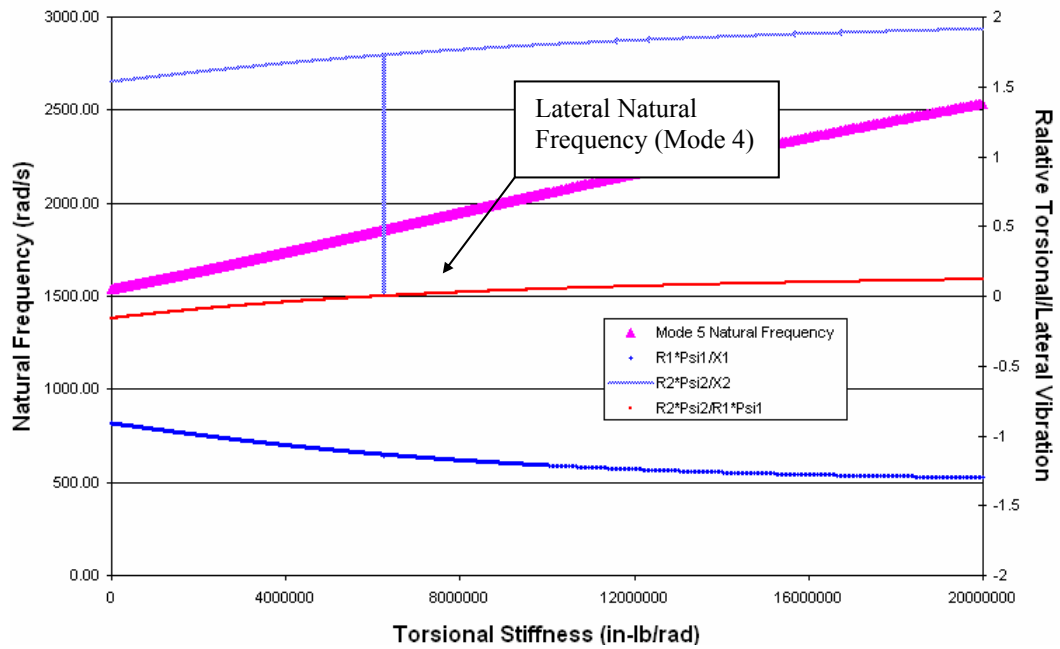
Mode 5: The Third Coupled Mode

Figure 31: Undamped natural frequency and mode shape (Mode 5) as a function of torsional stiffness Kt
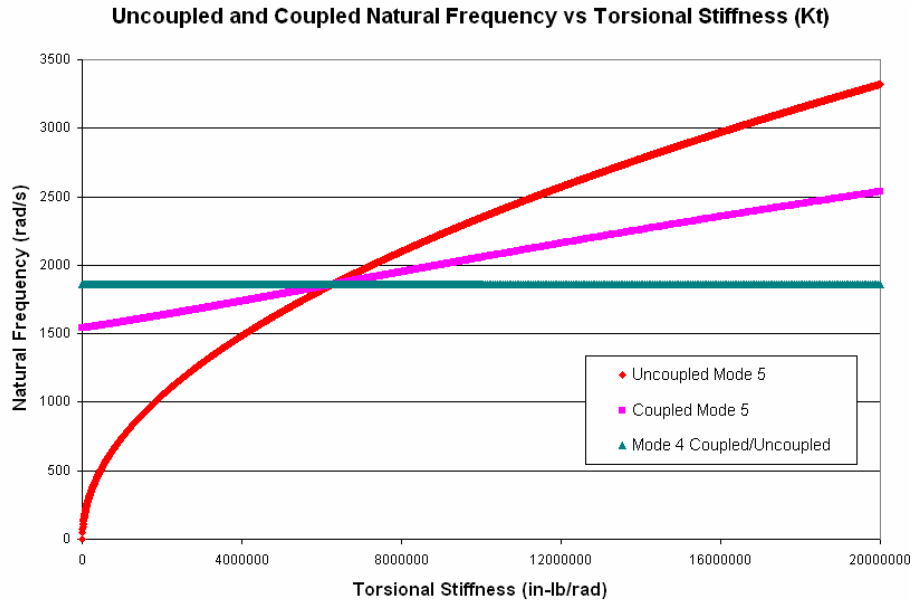
Figure 32: Undamped natural frequency and mode shape (Mode 5) as a function of torsional stiffness Kt

The closest agreement of this mode with the uncoupled modes occurs when the torsional stiffness causes a natural frequency close to the lateral natural frequency of Gear 2. Therefore, at this point, it may be possible to accidentally predict this natural frequency using the uncoupled case. Figure 31 shows the natural frequency and relative torsional/lateral vibration amplitudes as well as relative torsional amplitudes of Mode 5. Lateral vibration amplitudes in both gears are significant, with the vibration in the X_1 direction more than 75 percent of the torsional ψ_1 vibration. The influence that torsional stiffness plays in the relative vibration amplitudes levels off with increasing stiffness. One point to note in Figure 31 is the vibration amplitude seen in Gear 2 as the natural frequency approaches 1856 rad/s. This natural frequency also coincides with the natural frequency of Mode 4. As the natural frequencies of Mode 4 and Mode 5 intersect (see Figure 32), the vibration in Gear 2 goes to zero, though the uncoupled model suggests that a mode near this frequency is torsional.
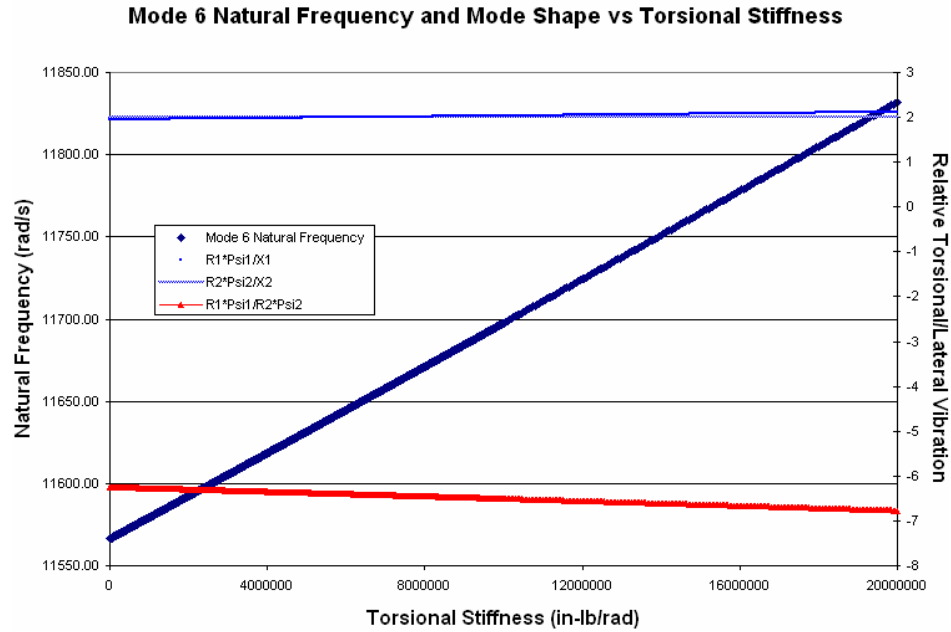
Mode 6: The Highest Natural Frequency

Figure 33: Undamped natural frequency and mode shape (Mode 6) as a function of torsional stiffness Kt

Figure 33 shows the highest natural frequency not shown in Figure 22. Significant lateral motion exists in the mode shape, with the highest lateral influence being that of X_2 (50 percent of the torsional motion). The relative motion between the two gears is dominated by the torsional vibration in Gear 1 and vibrates out of phase with respect to Gear 2. Increasing the torsional stiffness does not significantly affect the mode shape at this frequency for either gear.

Asymmetric Supports

Figure 34 shows how increasing torsional stiffness of the shaft affects the undamped natural frequencies for a system with asymmetric supports using the parameters listed in Table 3. The seemingly independent natural frequencies now become dependent on the torsional stiffness values as well, making the method used by Iwatsubo and Kahraman to uncouple two degrees of freedom from the system invalid for cases of asymmetric support stiffness.

Table 3: Parameters for system with asymmetric supports

m1 = .1451 lb$_m$	R1 = 5 in	Kx=100000
m2 = .9068 lb$_m$	R2 = 12.5 in	Ky=.25*Kx
0<Kt<2000000 in-lb/rad		
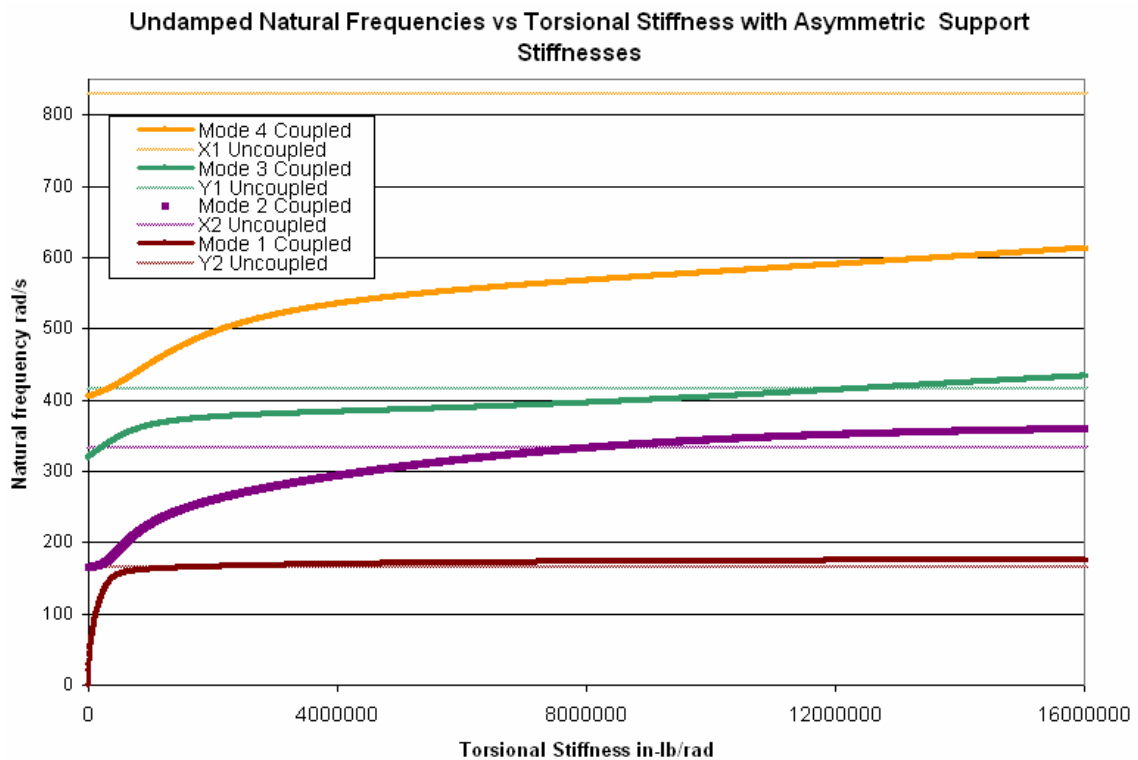
Figure 34: Undamped natural frequencies of uncoupled and coupled systems with asymmetric bearings as a function of torsional stiffness Kt

Figure 34 shows that unlike the case with symmetric supports, the uncoupled equations of motion do not always produce matching lateral natural frequencies. The difference between the first modes is approximately 5 percent, but this error increases significantly for the other three modes. Asymmetric bearing causes a vibration that does not line up perpendicular to the line of action. Slight torsional vibration shown now occurs (see Figure 35) and is the reason why torsional shaft stiffness can change the natural frequency of these laterally dominated modes.
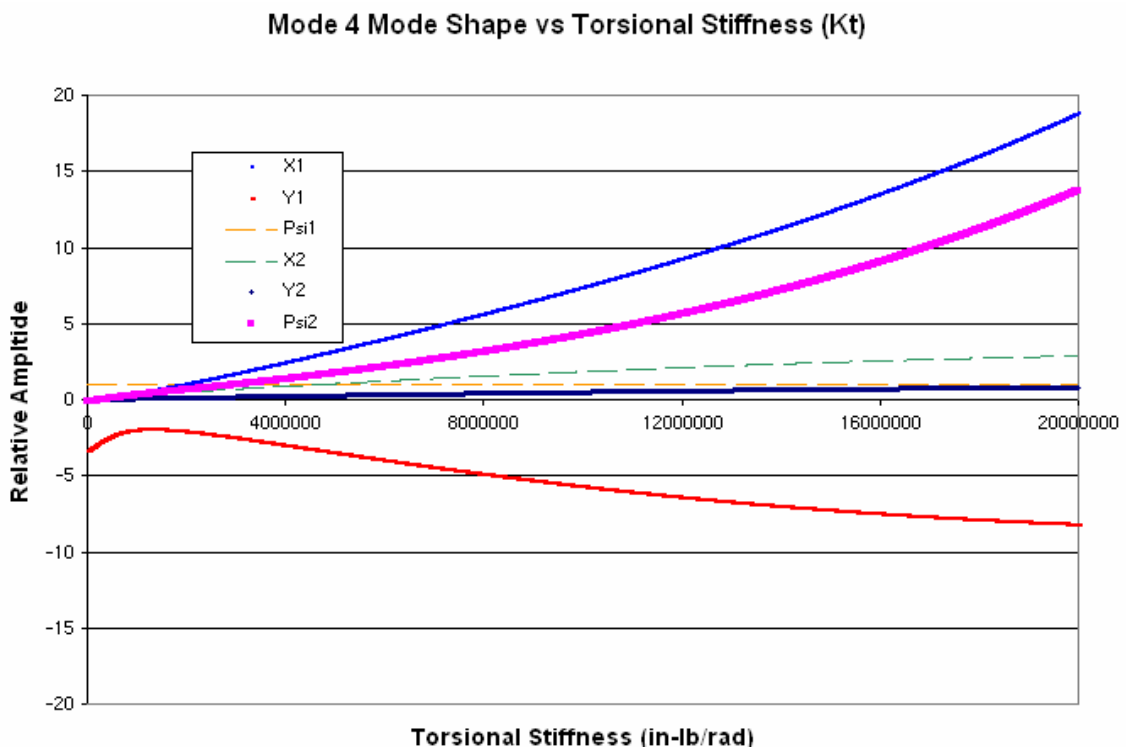
Figure 35: Mode 4 mode shapes as a function of torsional stiffness (normalized to ψ_1)

THE EFFECT LATERAL STIFFNESS HAS ON NATURAL FREQUENCIES WITH
SIGNIFICANT TORSIONAL MOTION

Figure 36 below shows how increasing lateral support stiffness values in the X and Y
directions affect the undamped natural frequencies when using the parameters listed in
Table 4. All of the natural frequencies appear to be strong functions of the lateral
support stiffness. The yellow and light blue lines exhibit the greatest dependency on the
lateral support stiffness as is expected since these natural frequencies are independent of
torsional stiffness in cases with symmetric supports. The other coupled natural
frequencies behave similar to the previous plots, where the influence of the lateral
stiffness diminishes as the stiffness becomes large.

Table 4: Parameters for system with symmetric supports for lateral stiffness analysis

m_1 = .1451 lb_m	R_1 = 5 in	Kt = 500000
m_2 = .9068 lb_m	R_2 = 12.5 in	Ky = Kx
0< Kx <50000 lb/in		
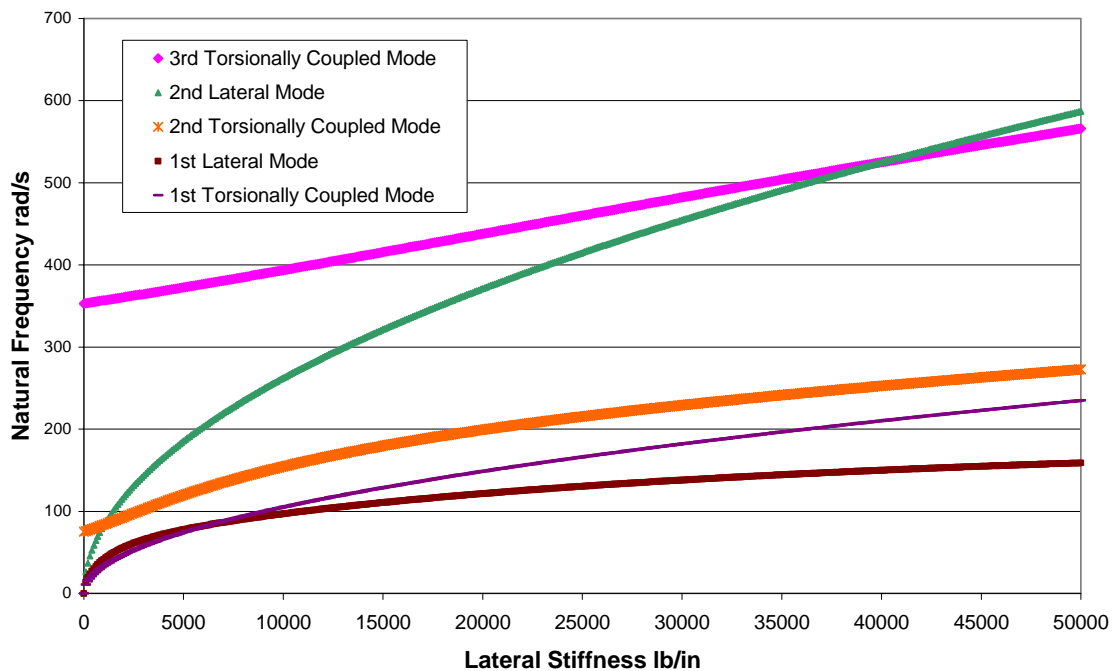
Figure 36: Undamped natural frequencies of system with symmetric bearing stiffness as a
function of lateral stiffness Kx

EFFECT OF TORSIONAL AND LATERAL STIFFNESS VALUES ON MODE 1

Figure 37 and 38 show how the lateral and torsional stiffness parameters listed in Table 5 affect the lowest coupled natural frequency and mode shape. When K_x is flexible, the natural frequency is loosely dependent on torsional stiffness. The torsional stiffness plays a larger role in the natural frequency as the support stiffness increases.

Table 5: Parameters for system with symmetric supports for various values of lateral stiffness

m1 = .1451 lb_m	R1 = 5 in	Kx = Various	0< Kt <1000000 in-lb/rad
m2 = .9068 lb_m	R2 = 12.5 in	Ky = Kx	
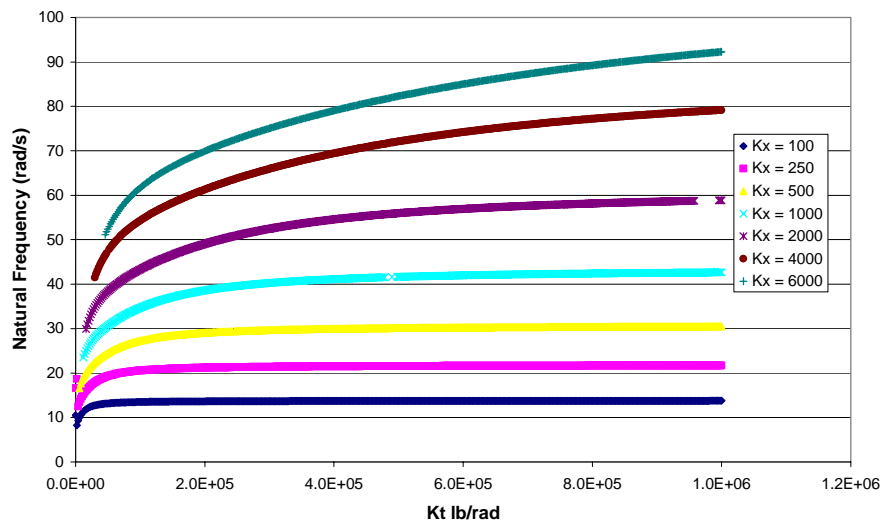
Figure 37: Natural frequency of lowest coupled mode with increasing torsional stiffness for various several lateral stiffness values
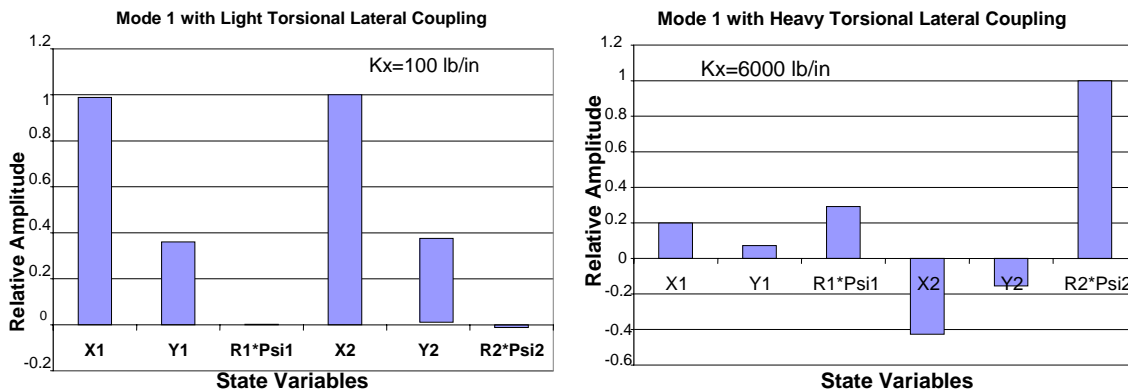
Figure 38: Change in mode shape as lateral support is stiffened from 100 lb/in to 6000 lb/in when Kt=100000 lb/rad

CRITICAL SPEED RESULTS

The forced response plot (Figure 39) obtained from the parameters listed in Table 6 is meant to show the accuracy of the forced response development. The eigenvalues, which were calculated independently of the forced response equations, agree with the peaks of the Forced Response Plot. The highest critical speed not shown on the graph corresponds with the calculated eigenvalue as well.

Table 6: Parameters for comparison to eigenvalue solutions

$m_1 = 0.029$ lb_m	$R_1 = 1$ in	$R_2 = 2.5$ in	$Kx = 5000$ lb/in
$m_2 = 0.0181$ lb_m	$Cx = 0.1$ lb-sec/in	$Ct = .1$ in-lb-sec/rad	$Kn = 2629381$ lb/in
	$u_1 = .004$ in	$u_2 = 0.004$ in	$Kt = 10000$ in-lb/rad
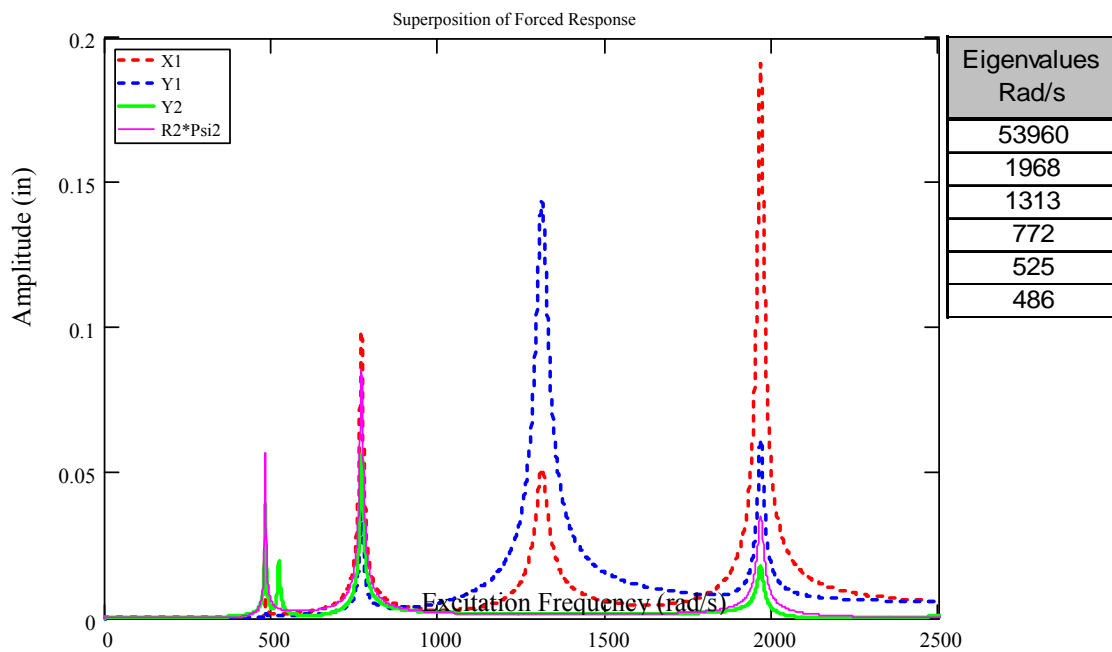
Figure 39: Forced response plot showing critical speeds closely match eigenvalues

Comparing Lateral Critical Speeds for Models with Symmetric Supports

Figure 40 and Figure 41 show that the uncoupled gear model successfully calculates two lateral critical speeds of the coupled system based on the parameters in Table 7. These plots confirm the results found during the natural frequency comparison where it was shown that the mode shape that vibrates perpendicular to the line of action would compare favorably to the uncoupled case. However, as these results show, the uncoupled case fails to predict the lateral vibration seen in other critical speeds.

Table 7: Parameters used for lateral critical speeds with symmetric bearings

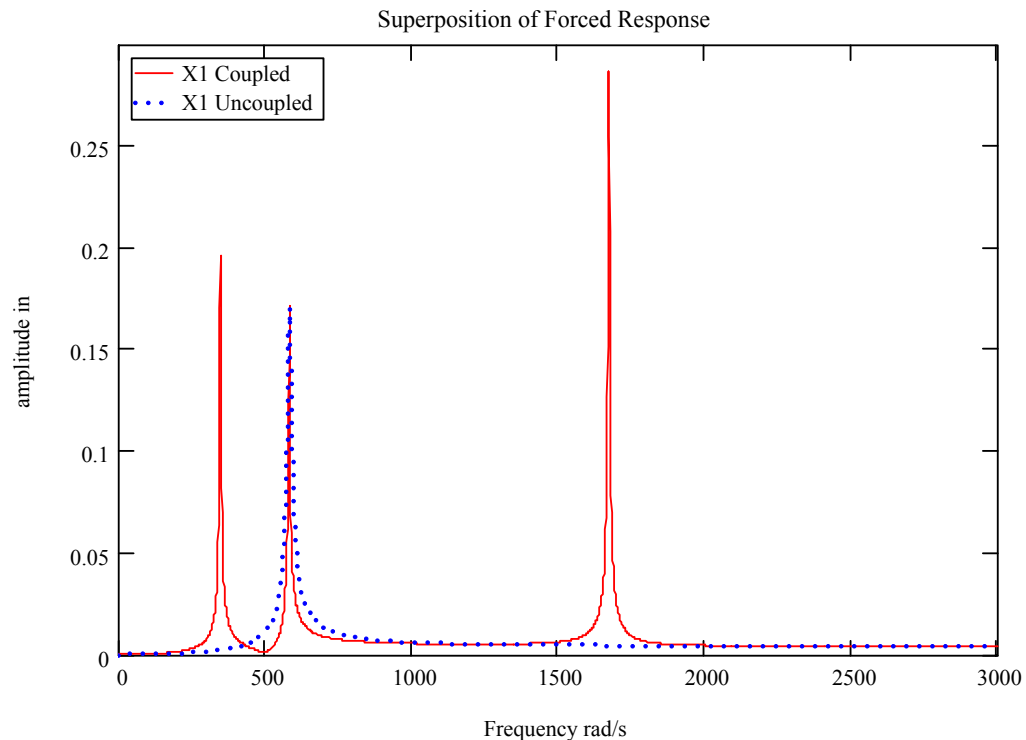| $m_1 = 0.029$ lb_m	$R_1 = 5$ in	$R_2 = 10$ in	Kx = 50,000 lb/in
$m_2 = 0.580$ lb_m	Cx =2 lb-sec/in	Ct = .1 lb-sec/rad	Ky = 50,000 lb/in
Kn = 5.94E6 lb/in	$u_1 = .004$ in	$u_2 = 0.004$ in	Kt = 10E6 in-lb/rad

Figure 40: Lateral (X1) forced response plot for uncoupled and coupled systems with symmetric bearings
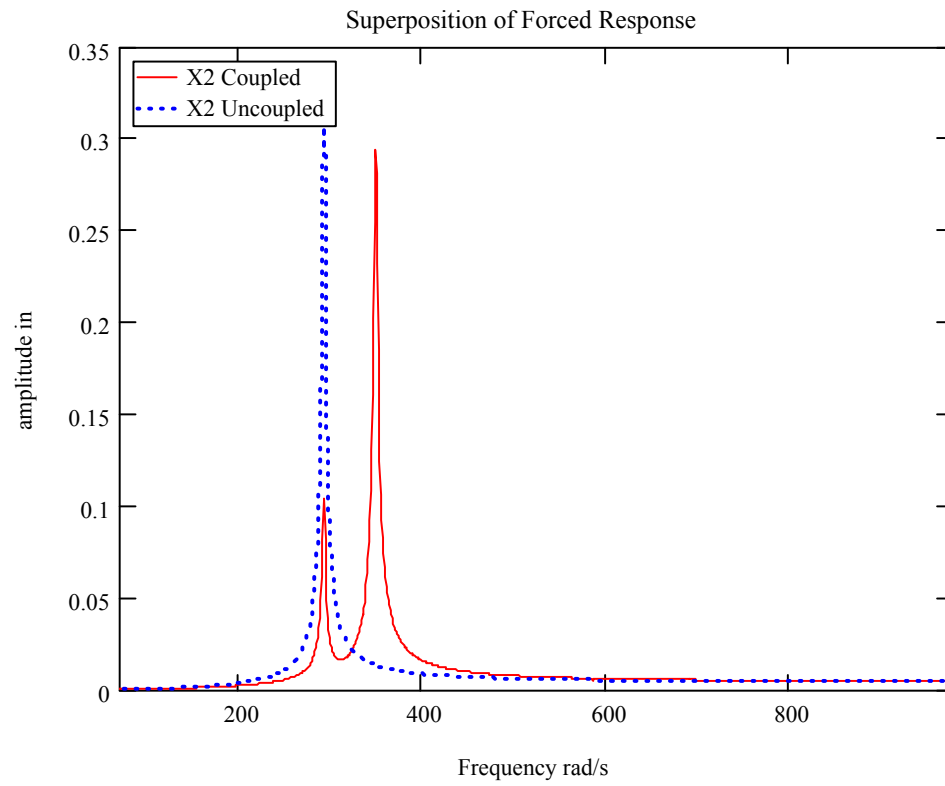
Figure 41: Lateral (X2) forced response plot for uncoupled and coupled systems with symmetric bearings

Comparing Lateral Critical Speeds of Models with Asymmetric Supports

Figure 42 through Figure 45 shows that lateral critical speeds calculations for an asymmetric system agree with the results obtained for the natural frequency study. The results show that the coupled lateral modes that matched the uncoupled modes with symmetric bearings no longer agree when asymmetric bearings are used. The parameters used in this simulation are listed in Table 8. With asymmetric bearings, the uncoupled model fails to predict all but one critical speed.

Table 8: Parameters used for lateral critical speeds with asymmetric bearings

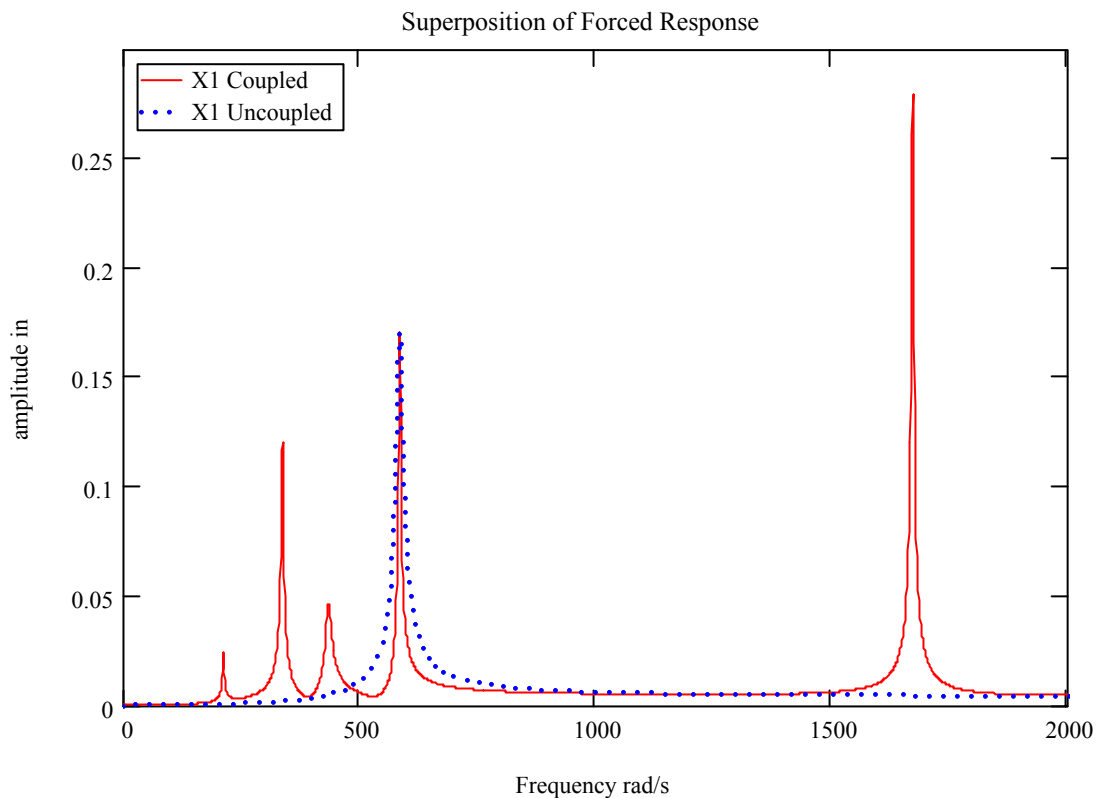| m_1 = 0.029 lb_m	R_1 = 5 in	R_2 = 10 in	Kx = 50,000 lb/in
m_2 = 0.0181 lb_m	Cx =5 lb-sec/in	Ct = .1 lb-sec/rad	Ky = 25,000 lb/in
Kn = 5,944,975 lb/in	u_1 = .004 in	u_2 = 0.004 in	Kt = 10E6 in-lb/rad

Figure 42: Lateral (X1) forced response plot for uncoupled and coupled models with asymmetric bearings
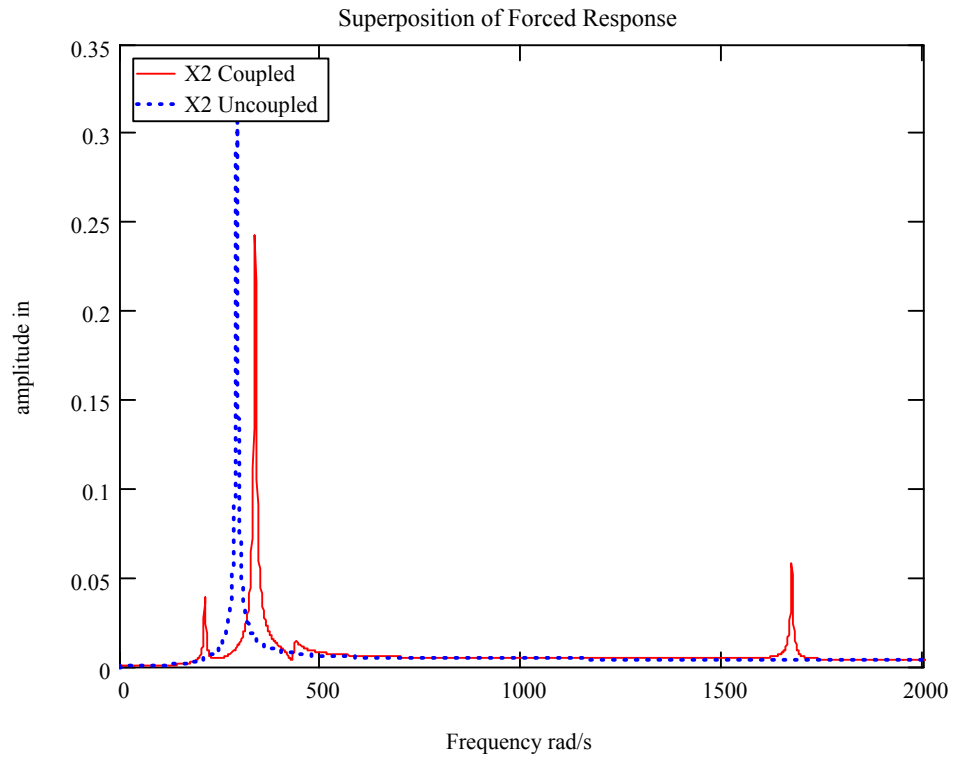
Figure 43: Lateral (X1) forced response plot for uncoupled and coupled models with asymmetric bearings
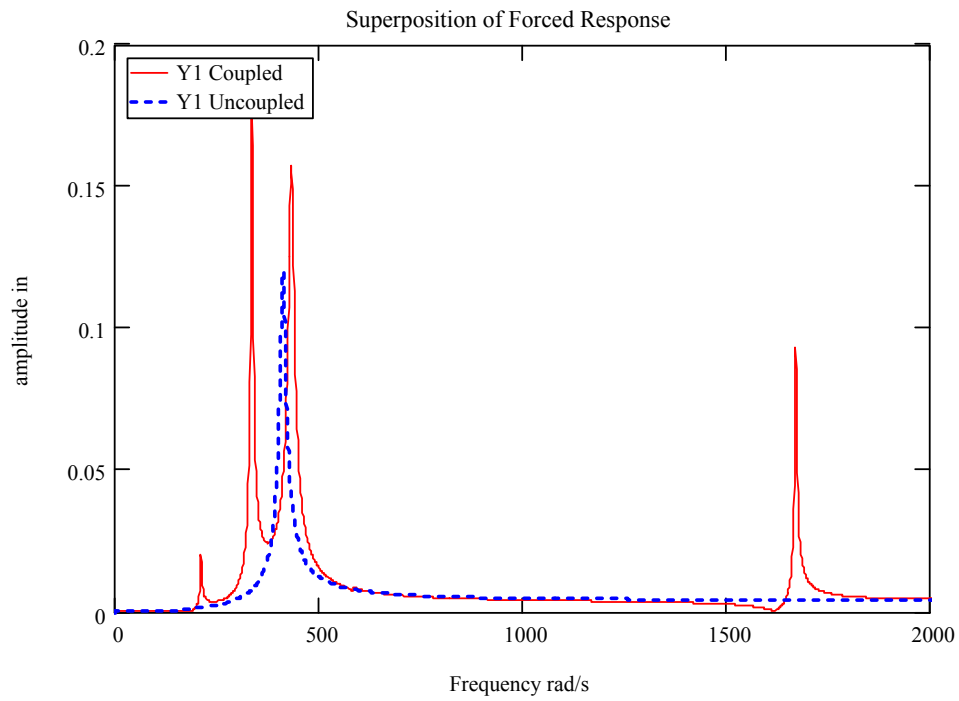

Figure 44: Lateral (Y1) forced response plot for uncoupled and coupled models with asymmetric bearings
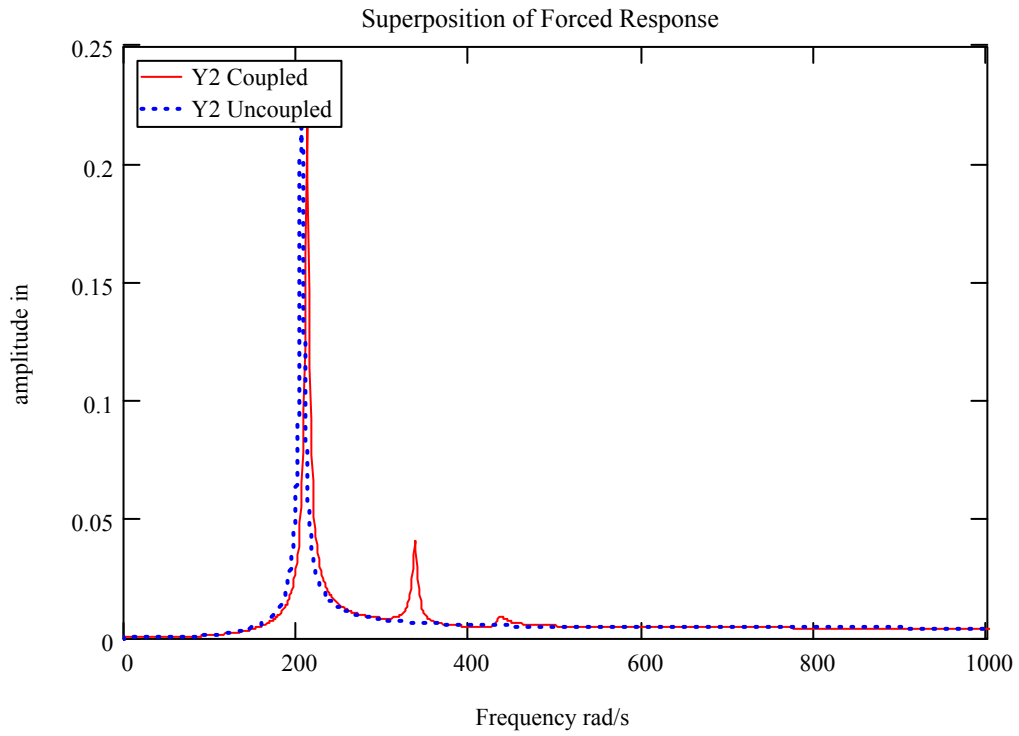
Figure 45: Lateral (Y2) forced response plot for uncoupled and coupled models with asymmetric bearings

Comparing the Torsional Critical Speeds of the Coupled Model to the Uncoupled Model

To study the forced response in the torsional direction, an external torsional torque has been added to the uncoupled equations of motion. The results show that the uncoupled does not predict torsional critical speeds consistently (Figure 46). Accurate predictions may be possible if certain lateral bearing stiffnesses are used (see Table 9 for parameters).

Table 9: Parameters for torsional critical speed plots

$m_1 = 0.029$ lb$_m$	$R_1 = 5$ in	$R_2 = 10$ in	Kx = 50,000 lb/in
$m_2 = 0.580$ lb$_m$	Cx =2 lb-s/in	Ct = .1 lb-s/rad	Ky = 25,000 lb/in
Kn = 5.94E6 lb/in	$u_1 = .004$ in	$u_2 = 0.004$ in	Kt = 10E6 in-lb/rad
$T_{1external} = 5000$ in-lb	$T_{2external} = 1000$ in-lb		
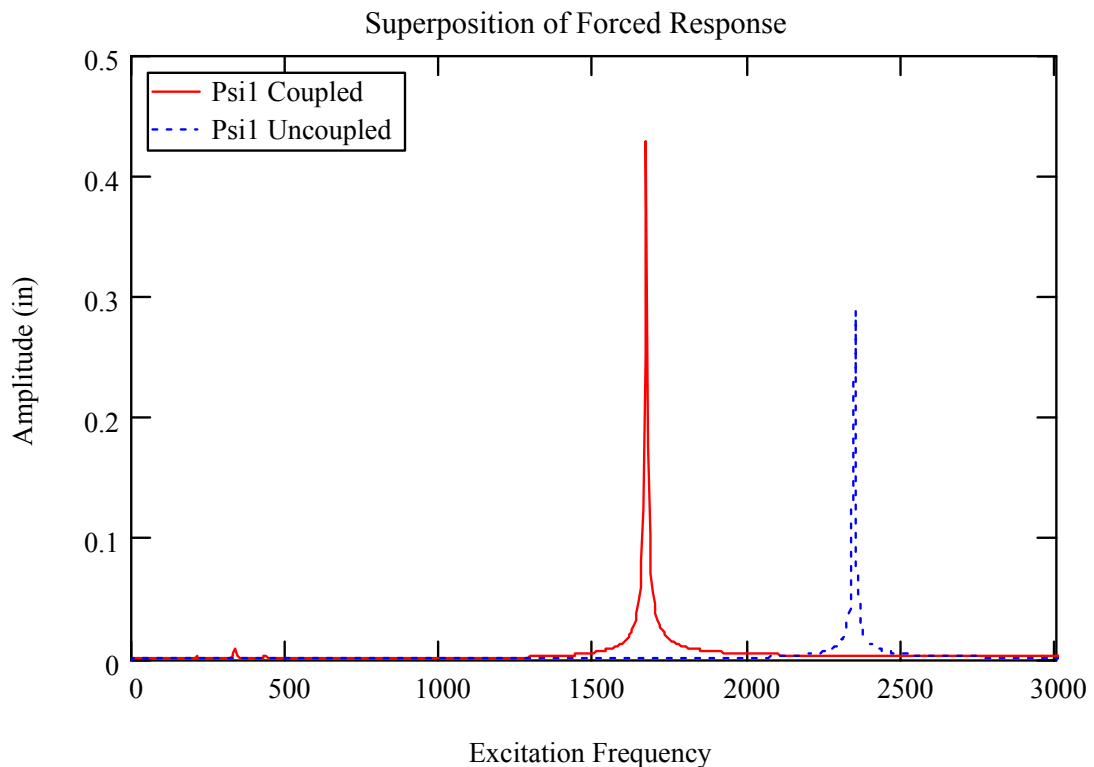
Figure 46: Torsional (Psi1) forced response plot for uncoupled and coupled models
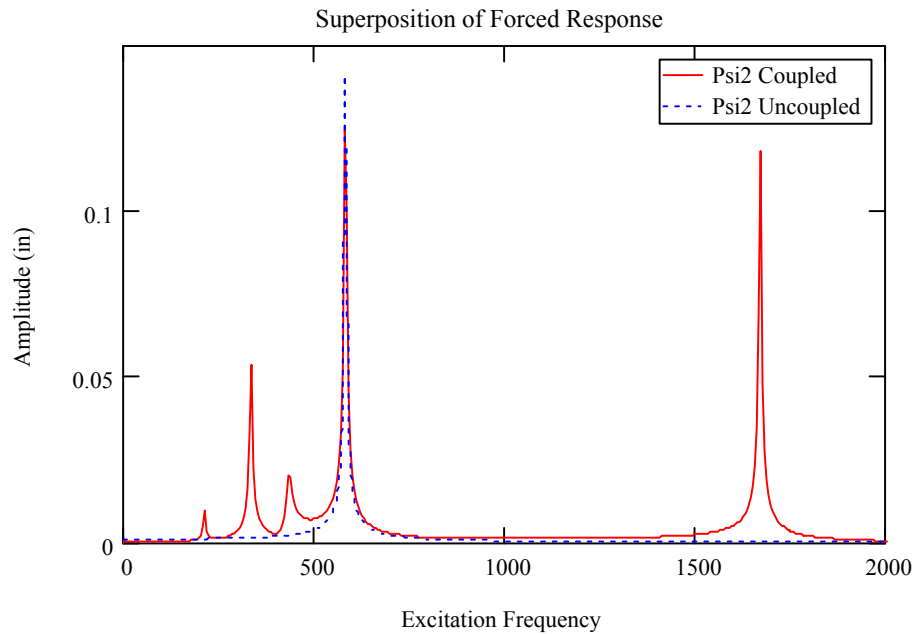
Superposition of Forced Response

Figure 47: Torsional (Psi2) forced response plot for uncoupled and coupled models

Figure 47 shows a case where the uncoupled model agrees with the coupled model. In this case, the uncoupled torsional natural frequency of the second gear happens to be extremely close to the uncoupled lateral natural frequency of the first gear. Figure 48 shows the models no longer agree when the lateral bearing stiffness is changed.
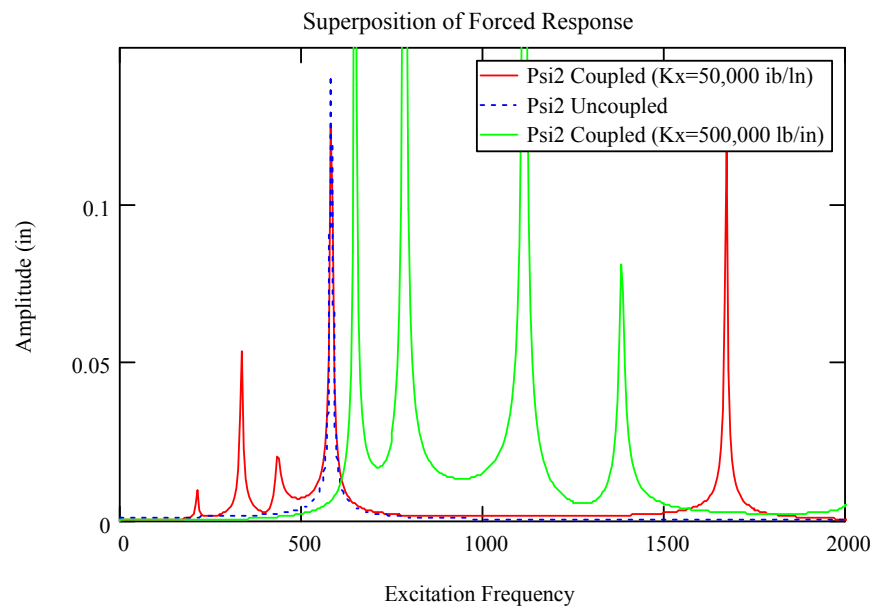
Superposition of Forced Response

Figure 48: Torsional (Psi2) forced response plot for uncoupled and coupled models using two lateral bearing stiffnesses

How Torsional Stiffness Affects the Coupled System's Lateral Critical Speeds

Figure 49 shows how external torsional stiffness affects lateral critical speeds based on the parameters listed in Table 10. The plot shows that the torsional stiffness can play a significant role in the critical speeds with significant lateral vibration. The critical speeds that move to the right as the torsional shaft stiffness is increased are the torsionally coupled critical speeds.

Table 10: Parameters for study of torsional stiffness effects on lateral critical speeds

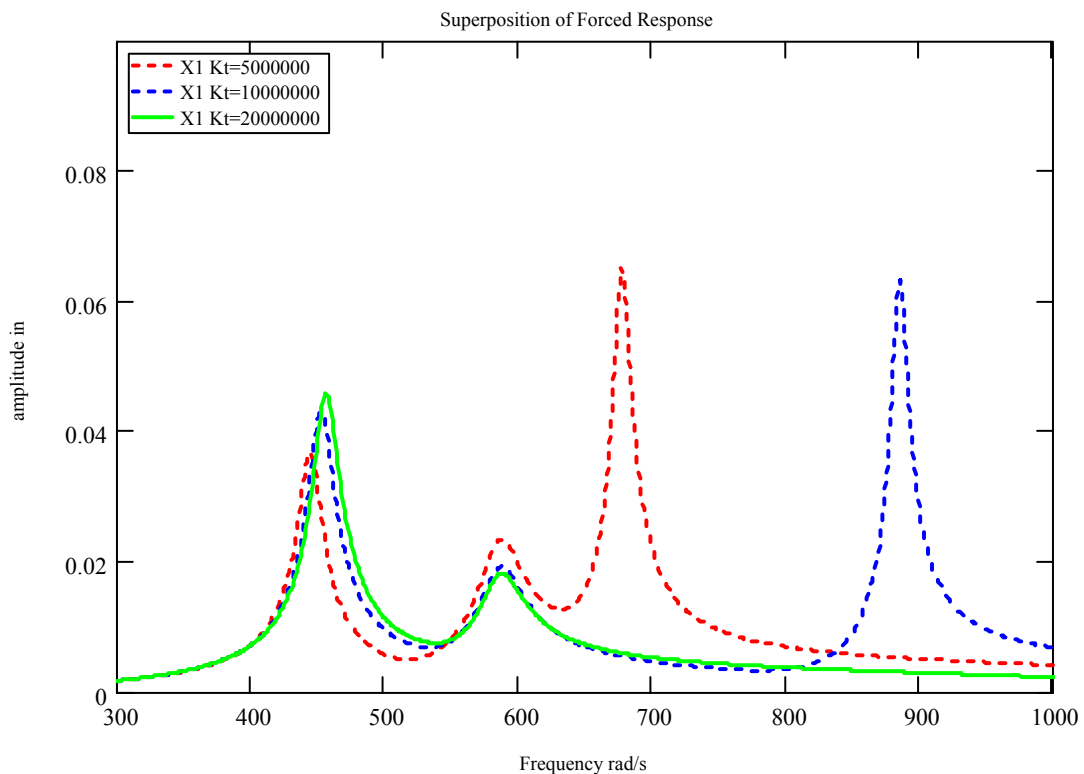| m1 =0.058 lbm	u1= 0.004 in	Cx = 1 lb-sec/in
m2 = 0.13 lbm	u2 = 0.004 in	Crψ = .001 1 lb-sec/rad
R1 = 5 in	Kx = 5000 lb/in	
R2 = 7.5 in	Kn = 2365430 lb/in	

Figure 49: Lateral forced response plots when torsional stiffness is varied

How Lateral Damping Affects the Coupled Model's Critical Speed Amplitudes

Figure 50 shows how lateral damping affects torsional critical speed amplitudes. The torsional critical speed amplitudes of Gear 1 decrease significantly as the lateral support damping is increased.
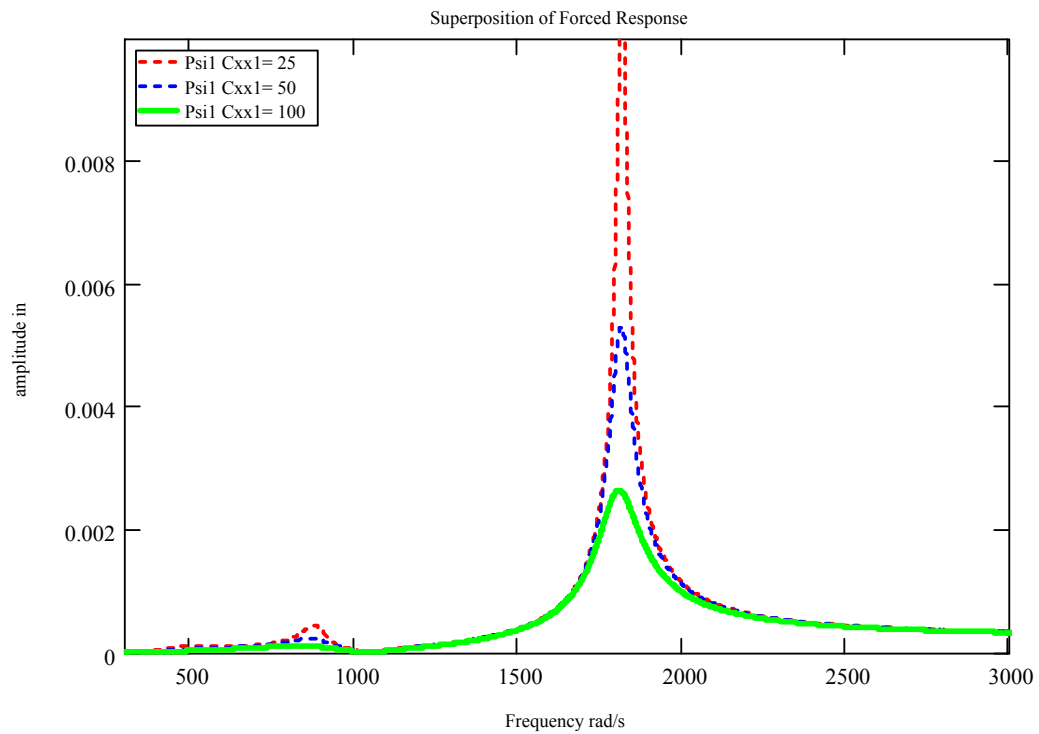

Figure 50: Forced response plot showing effect of lateral damping on torsional amplitudes

The Contribution of Lateral Damping to Effective Damping

Figure 51 shows how the lateral damping coefficient (Cxx1) affects the damping ratios of the other five modes based on the parameters listed in Table 11. The graph shows that increasing lateral damping also increases the damping ratios of the other modes in a linear fashion. The mode least affected by the increase in lateral damping is the critical speed associated with the tooth stiffness. However, the other coupled modes are more sensitive to lateral damping.

Table 11: Parameters for the study on the effects lateral damping has on damping ratios

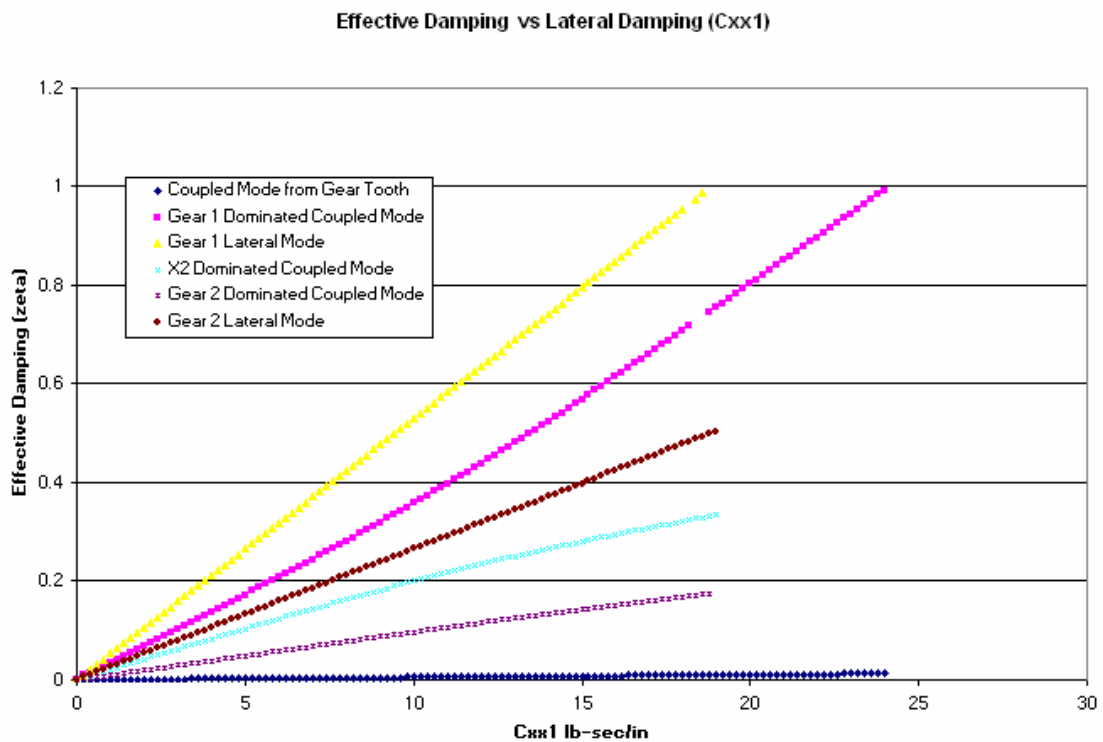| m1 =0.0725 lbm	Cx= Variable
m2 = 0.2902 lbm	Ct = .001 1 lb-sec/rad
R1 = 5 in	Kx = 1000 lb/in
R2 = 10 in	Kn = 2988941 lb/in

Figure 51: How the lateral damping coefficient (Cxx1) affects damping coefficients in other modes

CRITICAL SPEEDS WITH RESPECT TO GEAR RUNNING SPEED

So far, the forced response plots have been shown based on excitation frequency, not running speed. To show the critical speeds as a function of gear running speed, the forced response data is shown using two X-Axes; one based on the excitation from Gear 1's running speed and one based on the excitation from Gear 2's running speed. The parameters listed in Table 12 have been used in this study.

Table 12: Parameters used for forced response with respect to running speed

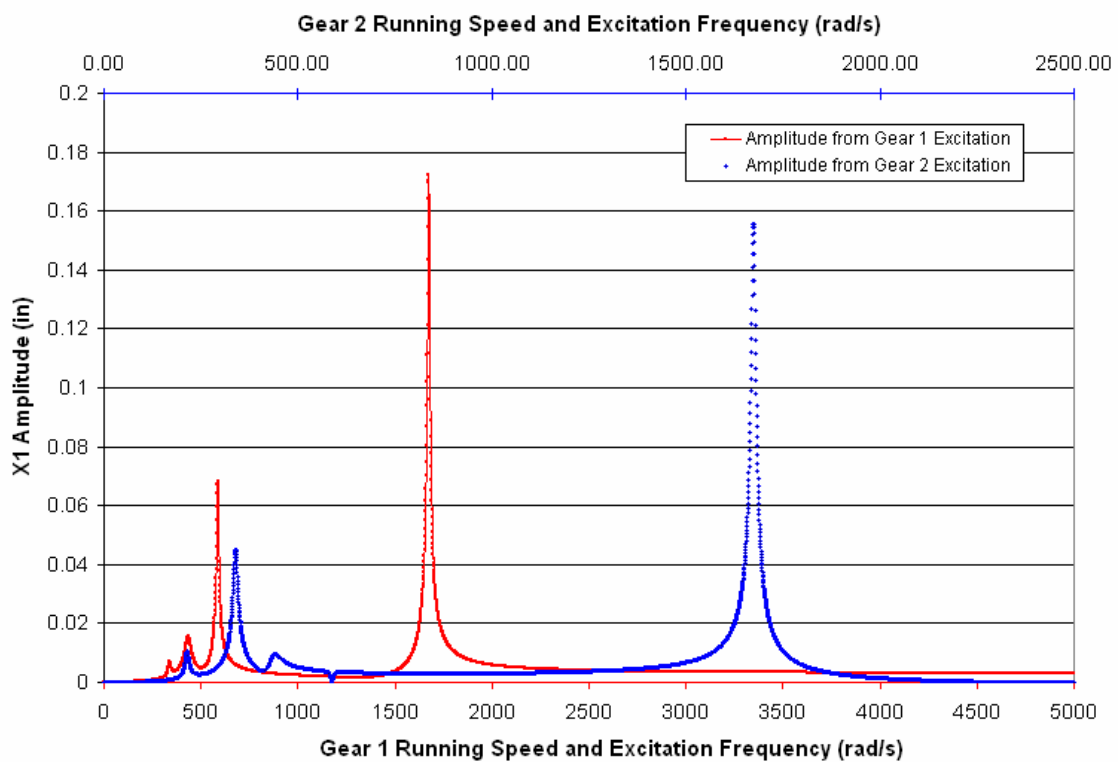| $m_1 = 0.029$ lb$_m$ | $R_1 = 5$ in | $R_2 = 10$ in | Kx = 50,000 lb/in |
| $m_2 = 0.0181$ lb$_m$ | Cx =5 lb-s/in | Ct = .1 lb-s/rad | Ky = 25,000 lb/in |
| Kn = 5.944E6 lb/in | u_1 = .004 in | u_2 = 0.004 in | Kt = 10,000,000 in-lb/rad |

Figure 52: Lateral X1 forced response plot with respect to running speed

Figure 52 shows the response of the lateral X_1 direction for each excitation source. The red line is the synchronous vibration amplitude of X_1 due to the rotating unbalance of Gear 1. The blue line is the subsynchronous vibration amplitude of X_1 due to the rotating unbalance of Gear 2. The figure shows the unbalance in Gear 2 causes significant subsynchronous lateral X_1 vibrations in Gear 1
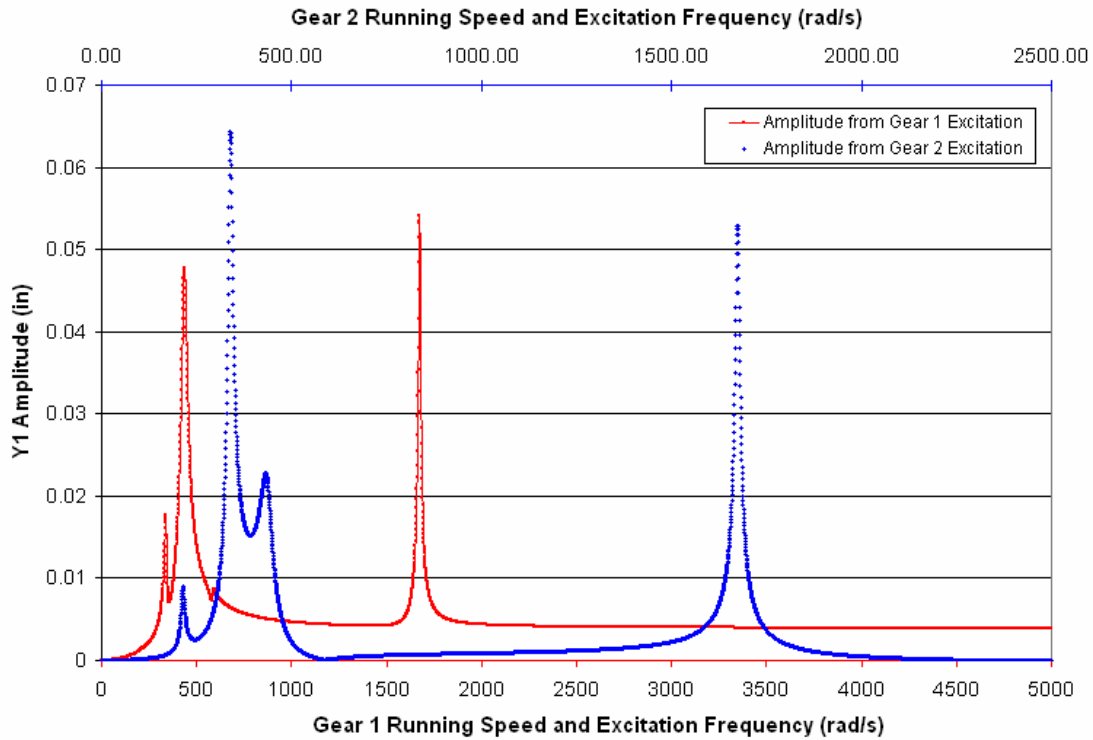

Figure 53: Lateral Y1 forced response plot with respect to running speed

Figure 53 shows the response of the lateral Y_1 direction for each excitation source. The red line is the synchronous vibration amplitude of Y_1 due to the rotating unbalance of Gear 1. The blue line is the subsynchronous vibration amplitude of Y_1 due to the rotating unbalance of Gear 2. The figure shows that the subsynchronous vibration amplitude caused by Gear 2 exceeds the vibration amplitude caused by Gear 1.
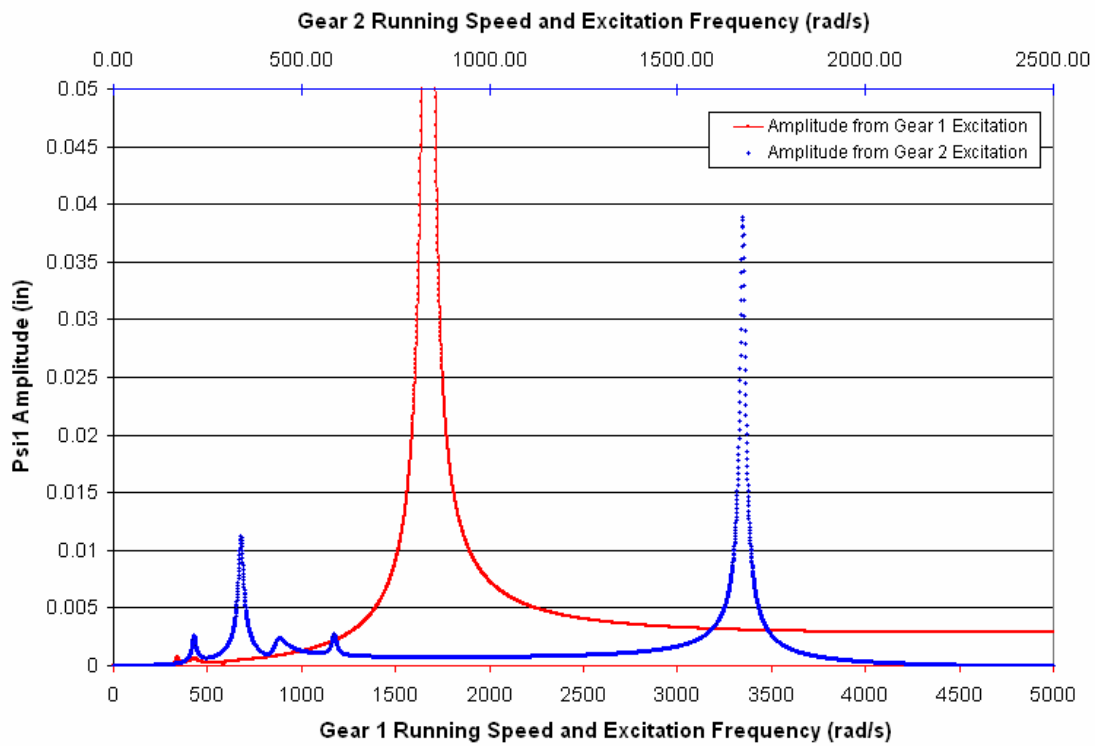
Figure 54: Torsional ψ_1 forced response plot with respect to running speed

Figure 54 shows the response of the lateral ψ_1 direction for each excitation source. The red line is the synchronous vibration amplitude of ψ_1 due to the rotating unbalance of Gear 1. The blue line is the subsynchronous vibration amplitude of ψ_1 due to the rotating unbalance of Gear 2. The figure shows that the subsynchronous vibration caused by Gear 2 exists, but compared to the lateral case, plays a smaller roll in the overall torsional vibration of the Gear 1.

Figure 55 and Figure 56 show the lateral X_2 and Y_2 forced response amplitudes. For Gear 2 (the larger gear), the vibration caused by Gear 1 is supersynchronous (red line) to its running speed. Compared to the effects Gear 2 has on subsynchronous vibrations in Gear 1, the effects Gear 1 has on supersynchronous vibrations in Gear 2 play a smaller roll.
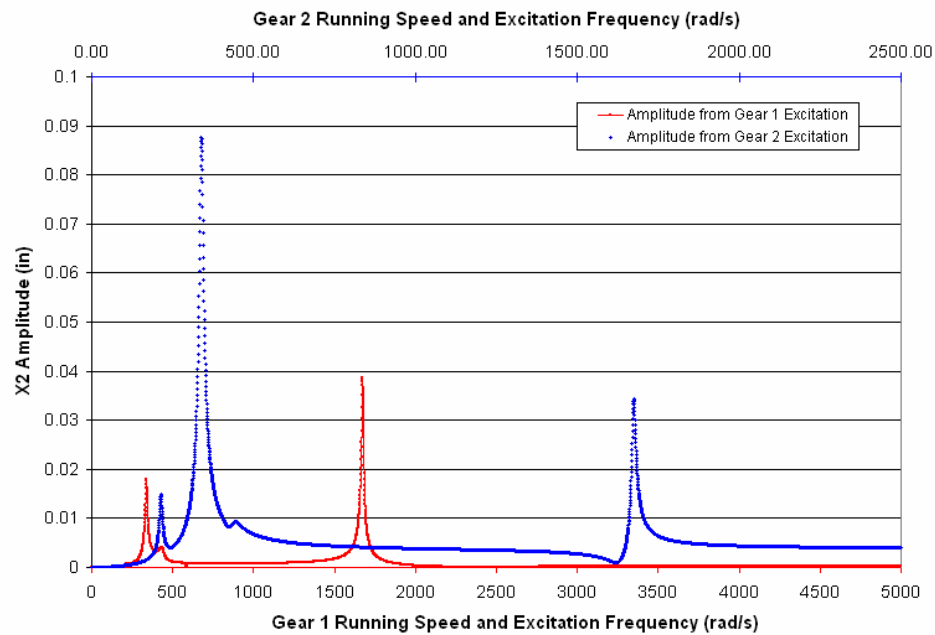

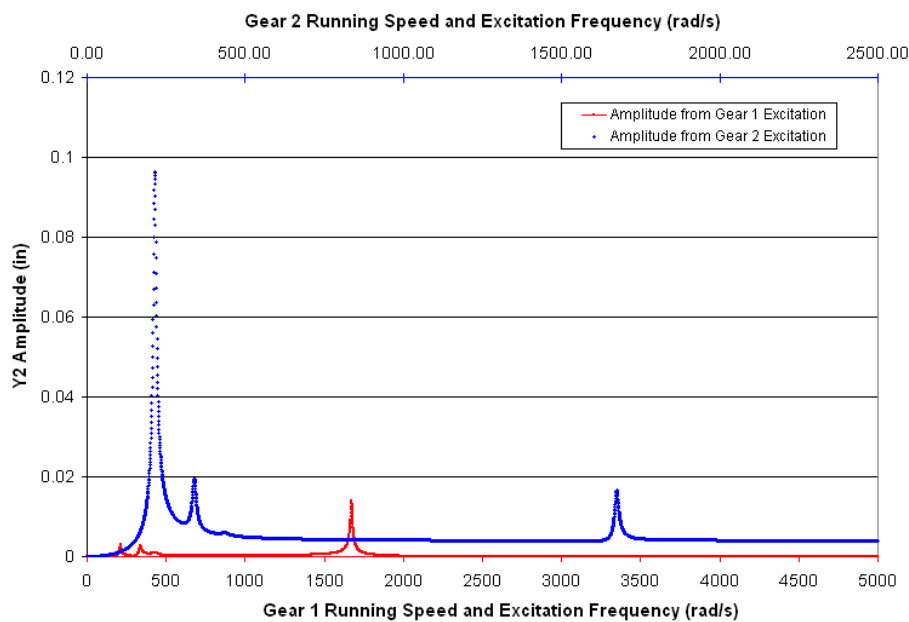**Figure 55:** Lateral X_2 forced response plot with respect to running speed

Figure 56: Lateral Y_2 forced response plot with respect to running speed
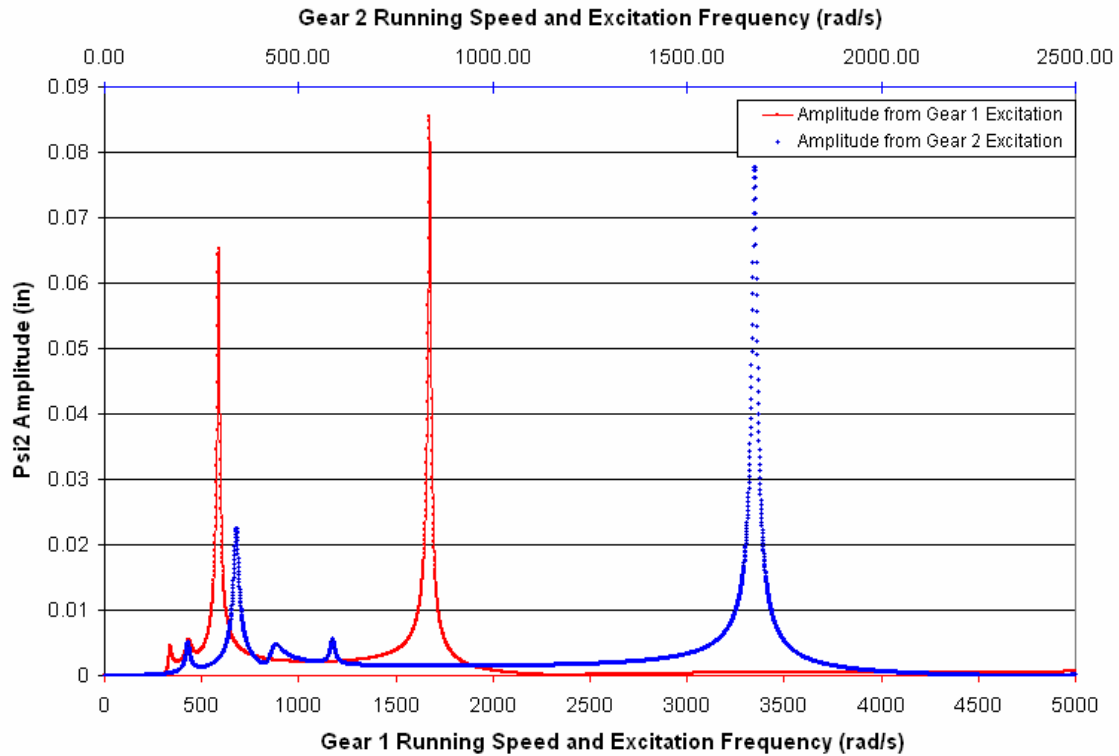
Figure 57: Torsional ψ_2 forced response plot with respect to running speed

Figure 57 shows the torsional ψ_2 forced response amplitudes. The red line is the supersynchronous vibration amplitude of ψ_2 due to the rotating unbalance of Gear 1. The blue line is the synchronous vibration amplitude of ψ_2 due to the rotating unbalance of Gear 2. The figure shows that the supersynchronous component of the ψ_2 can be as great as or greater than the synchronous vibration, depending on the running speed.

NONSYNCHRONOUS VIBRATIONS AND THE WACHEL PAPER

In their paper, Wachel and Szenasi conclude that the vibration of the fourth stage compressor was an instability because it contained a vibration frequency not equal to its running speed (See Figure 58). Also, the unstable lateral vibrations they measured were at the same frequency as the third torsional natural frequency (see Figure 59). They concluded that the vibrations were coming from the idler gear (the larger gear) and were transferred through the pinion and to the fourth stage compressor.
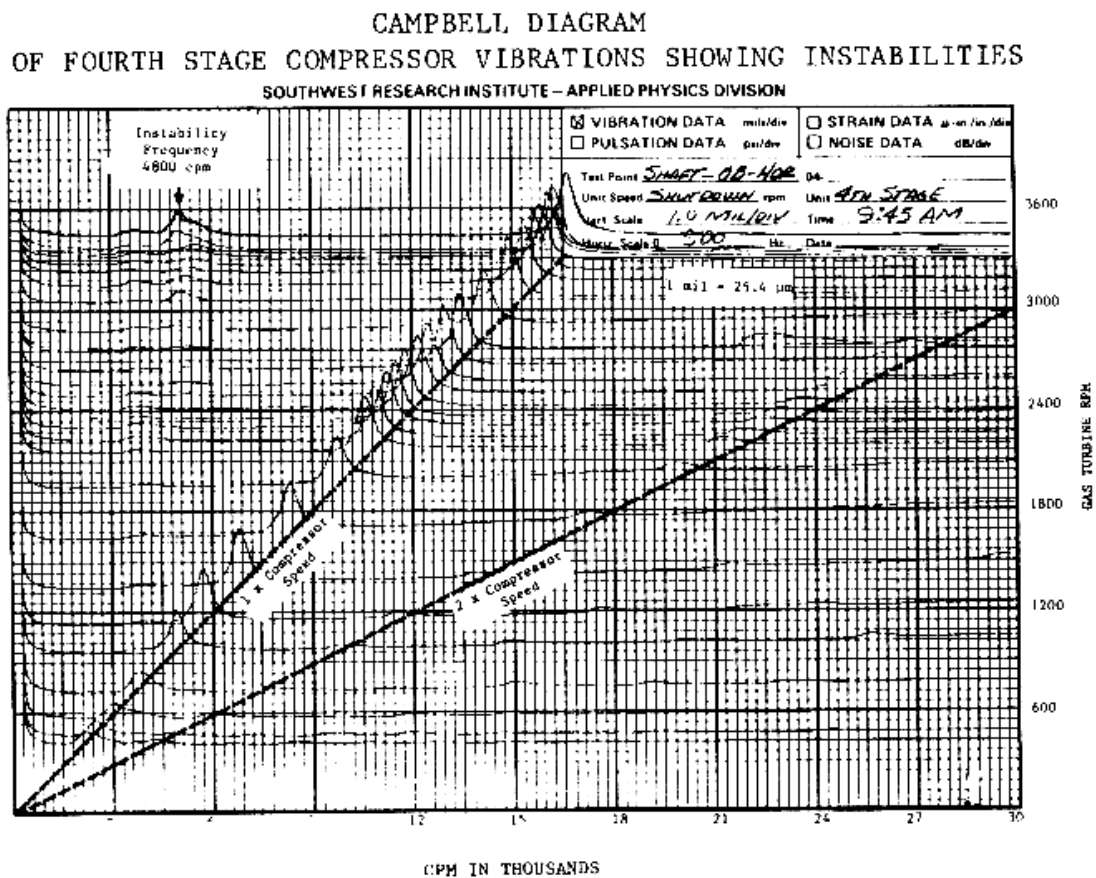

Figure 58: Lateral waterfall plot of the fourth stage compressor [1]

TORSIONAL VIBRATIONS MEASURED ON PINION
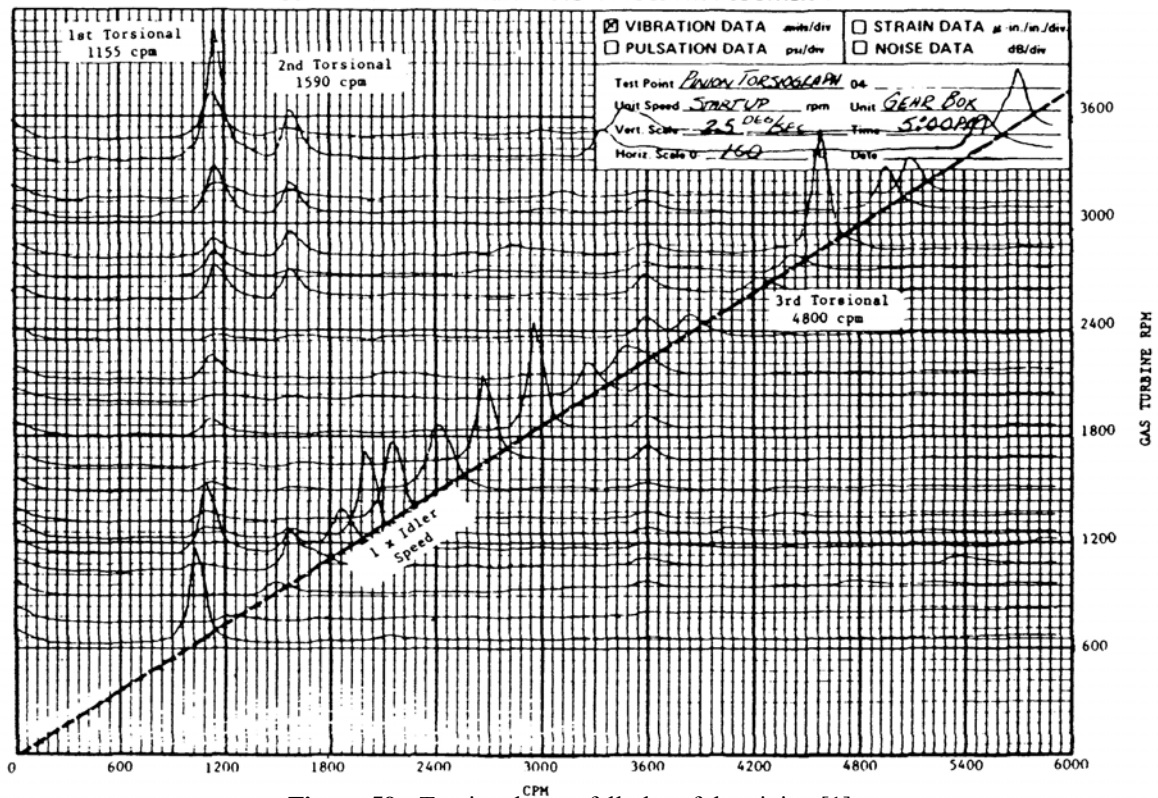### SOUTHWEST RESEARCH INSTITUTE – APPLIED PHYSICS DIVISION

Figure 59: Torsional waterfall plot of the pinion [1]

Figure 60 shows that the sub-synchronous lateral vibrations with a well balance gear are very low at slower running speeds. The subsynchronous vibrations in Gear 1 spike when the first coupled torsional natural frequency is excited by the second gear (Figure 61). This may be an explanation to the instability seen by Wachel and Szenasi. Note that subsynchronous spike is not an unstable vibration. Similar waterfall results can be reproduced in MathCAD[TM] based on the amplitudes from the forced response calculations and the assumed sinusoidal vibration wave. The parameters used in this study are listed in Table 13.

Table 13: Parameters used to create apparent instability

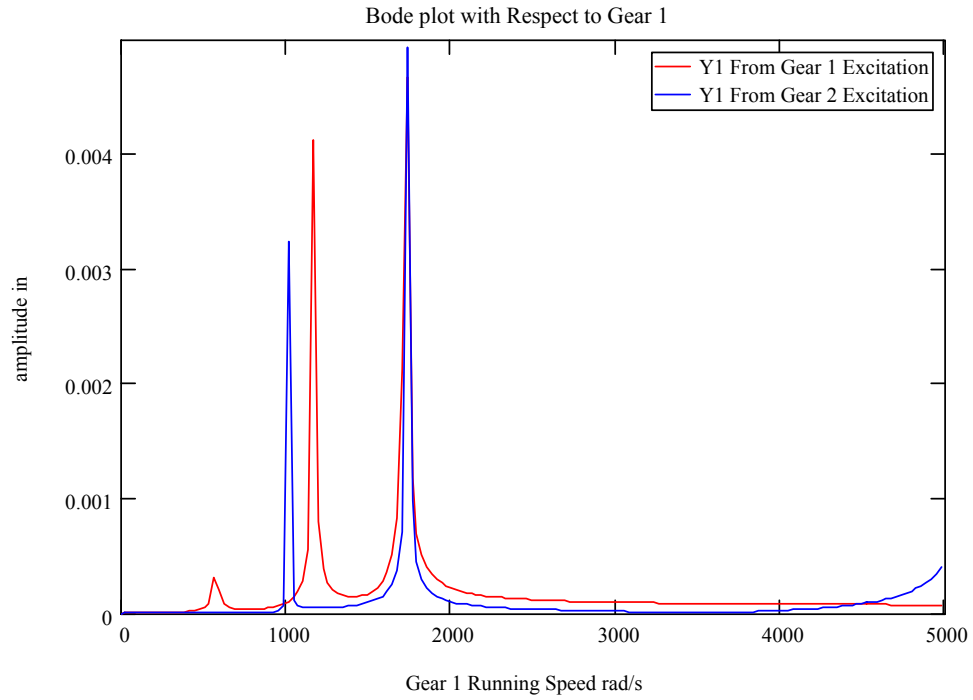| m_1 = .1451 lbm	$K_x=K_y$=20000 lb/in	$C_x=C_y$=0.75 lb-sec/in
m_2 = 1.3057 lbm	$u_1=u_2$=.0001 in	R_1 = 5 in
K_n = 6,012,477 lb/in	K_t=10,000,000 in-lb/rad	R_2 = 15 in

Bode plot with Respect to Gear 1

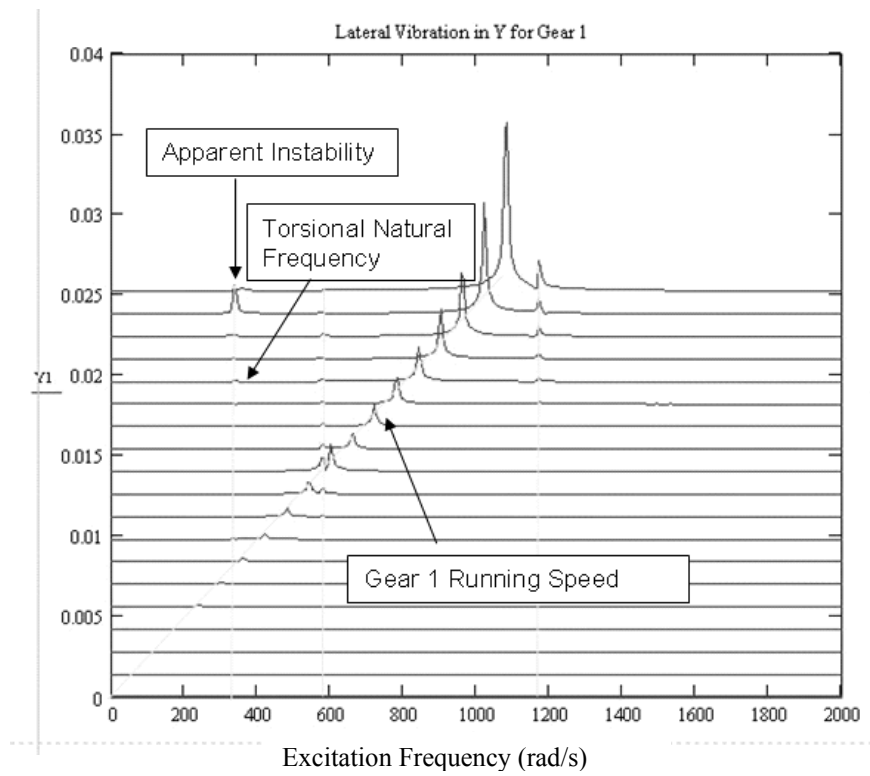**Figure 60:** Lateral Y_1 bode plot with respect to Gear 1 running speed

Figure 61: Lateral Y_1 waterfall plot of Gear 1

THE ROTATING MOMENT ARM'S EFFECT ON SYSTEM VIBRATION

The waterfall plots from the numerical integration results are shown in this section. The results show that the lowest natural frequency can be heavily excited by the rotating moment arm of the second gear when using the parameters listed in Table 14. Figure 62 shows that the first mode shape of the first is torsionally-laterally coupled at this natural frequency. This excitation is subsynchronous in relation to the running speed of Gear 1 and supersynchronous in relation to the running speed of Gear 2.

Table 14: System parameters for waterfall computation

m1 = .1451 lb$_m$	Kx = 30000 lb/in	Cx = 10 lb-s/in
m2 = .9068 lb$_m$	Ky = 30000 lb/in	Cy = 10 lb-s/in
R1 = 5 inch	Kn = 5977883 lb/in	Ct = 0 in-lb-s/rad
R2 = 12.5 inch	Kt = 200000 in-lb/rad	α = 20 degrees
u1 = 0.4 in	u2 = 0.8 in	ω$_n$ = 109 and 199 rad/s

Mode Shape of Torsional Dominate Eigenvalue
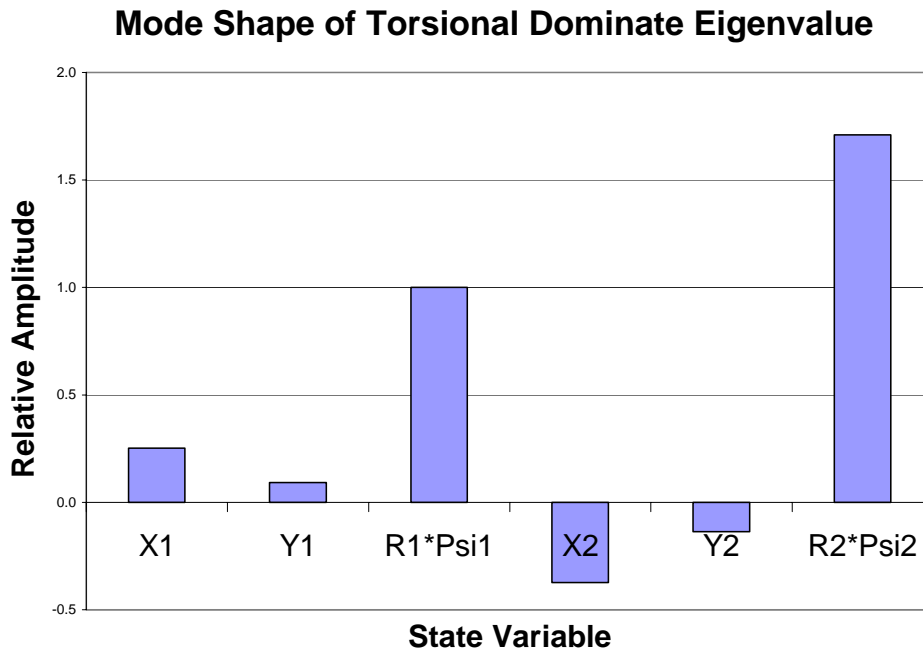

Figure 62: Mode shape of first eigenvalue

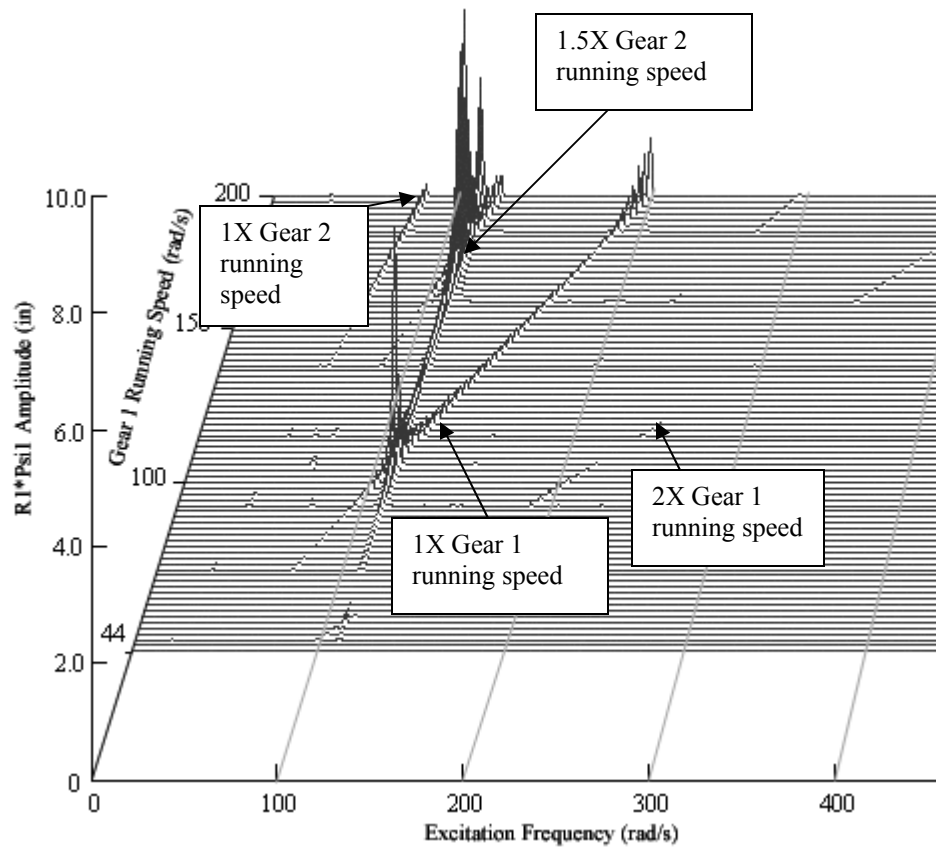**Figure 63:** Torsional vibration in ψ1 direction of Gear 1 for 44-200 rad/s running speeds
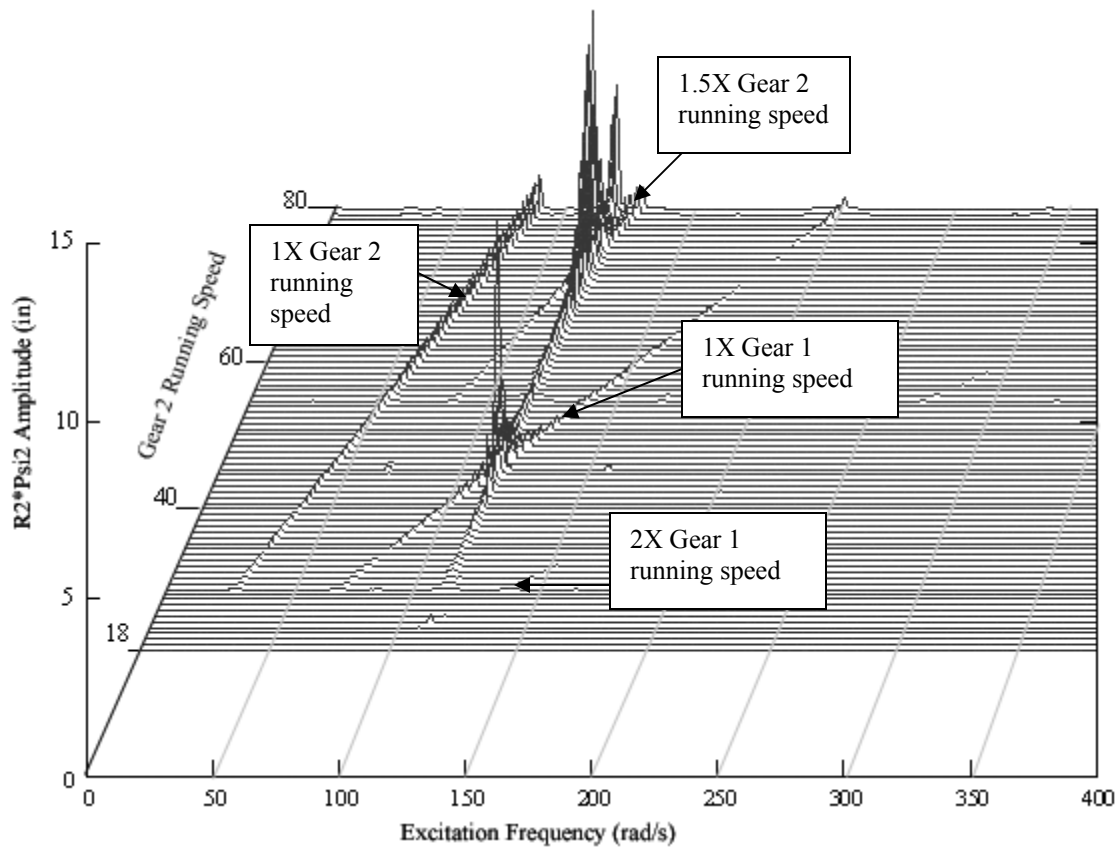
Figure 64: Gear 2 torsional vibration in ψ_2 direction for 18-80 rad/s running speeds
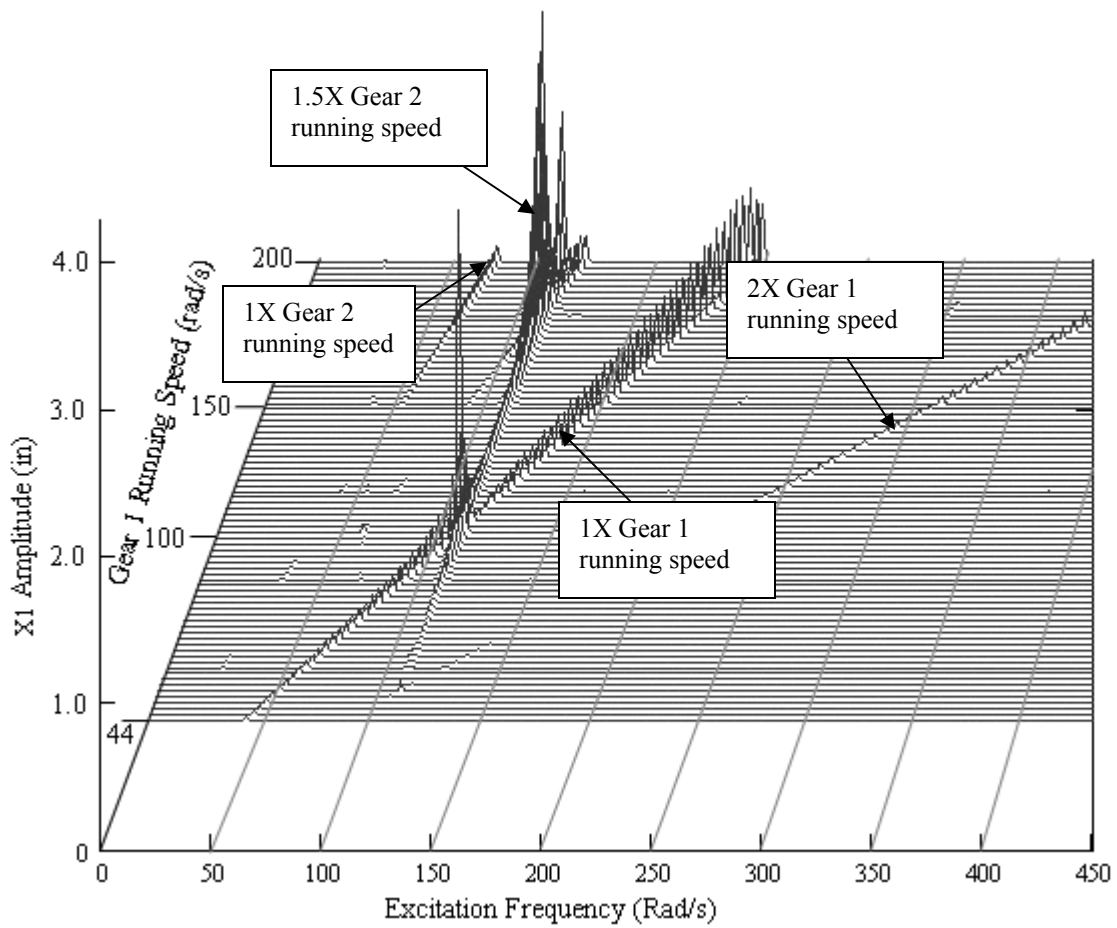
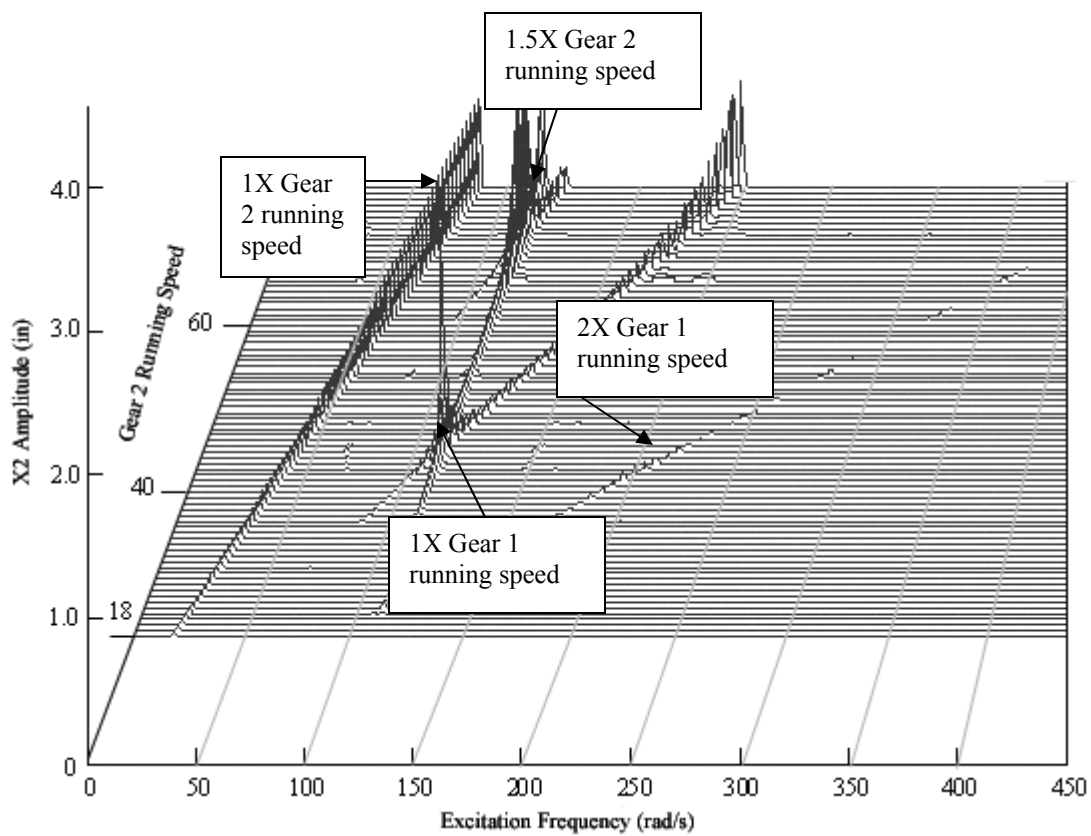**Figure 65:** Lateral vibration in X_1 for 44-200 rad/s running speeds

Figure 66: Lateral vibration in X_2 for 18-80 rad/s running speeds
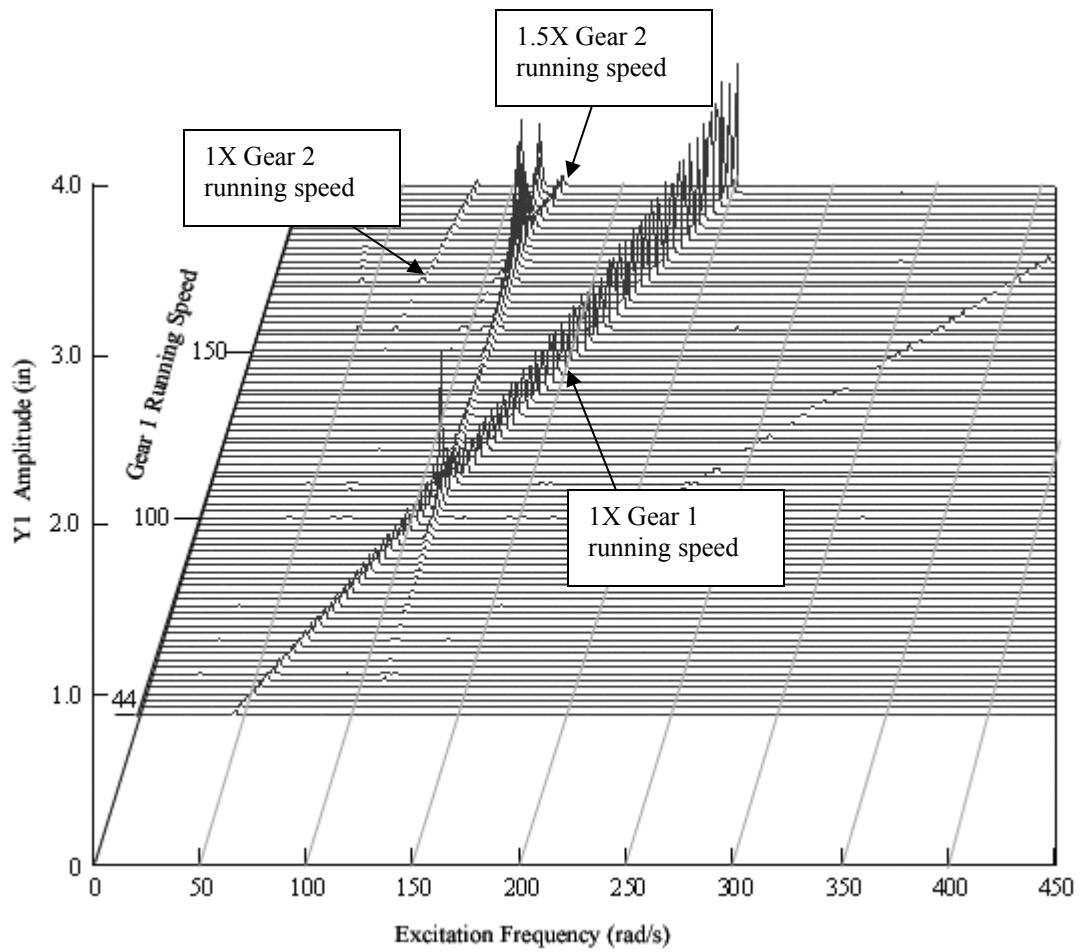
Figure 67: Lateral vibration in Y_1 for 44-200 rad/s running speeds
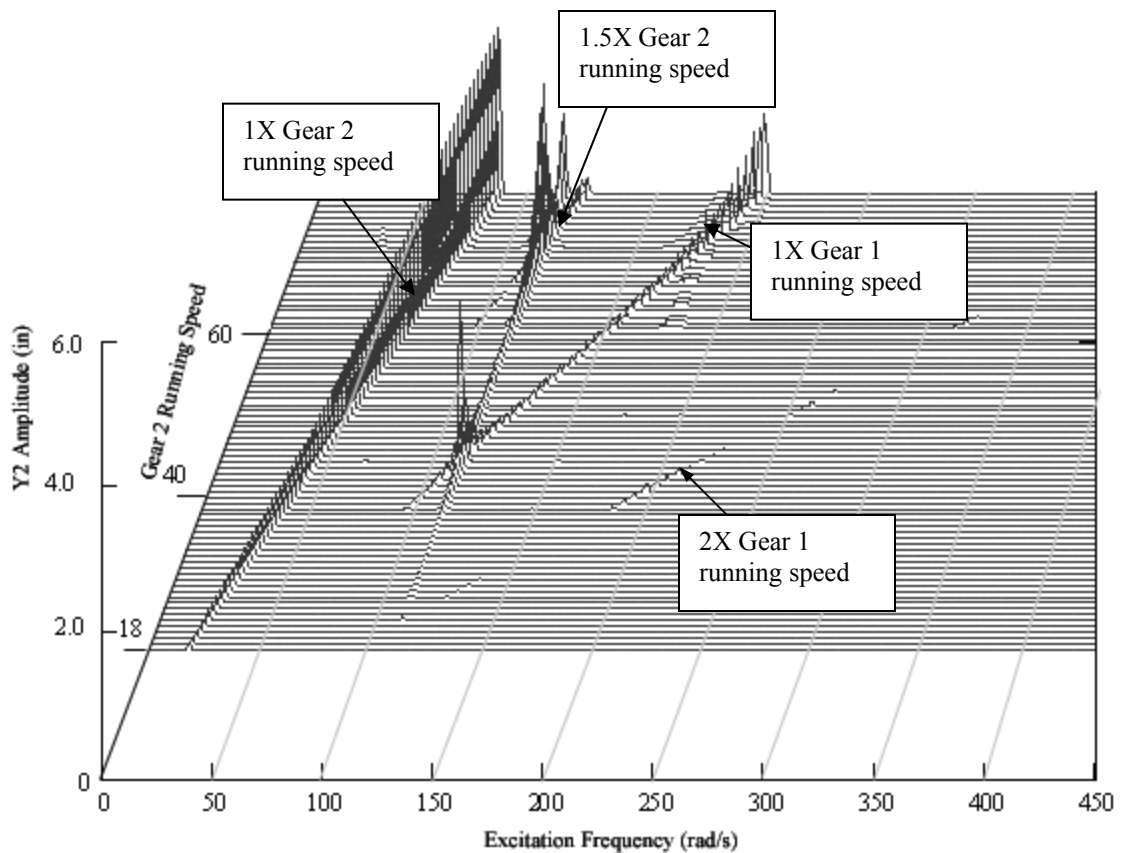
Figure 68: Lateral vibration in Y_2 for 18-80 rad/s running speeds

The waterfall plots shown in Figures 63-68 agree with the previous assertion that highly unbalanced gears exhibit non-synchronous (to either gear) harmonic frequencies. Furthermore, the plot shows that these harmonics excite the first natural frequency (which is has a highly torsional mode shape) several times during run-up. Surprisingly, the subsynchronous harmonic component is (R2/R1-1) times the running speed of Gear 2. Looking at Figure 63, the 1.5X sub-harmonic vibrations from Gear 2 excite the eigenvalues nearly as much as the synchronous component from Gear 1. This frequency is first excited, though much smaller, by the second order component of the from Gear 1's rotating moment arm.

V. CONCLUSIONS

The uncoupled gear model was compared to the six DOF coupled gear model. The results show that the uncoupled model fails to accurately predict as many as five natural frequencies, depending on the symmetry of the gear supports. With asymmetric supports the uncoupled model is less likely to predict any mode above the first mode, though certain exceptions do exist.

A force response analysis of the coupled system was used to study the forced excitations of a rotating mass imbalance. The results show that lateral critical speeds can be significantly affected by changes in torsional shaft stiffness. Further study of the forced response resulted in the finding that lateral damping can lower torsional critical speed amplitudes.

A well balanced, lightly damped geared rotor may show signs of instability if one of the torsional-lateral coupled natural frequencies is excited by the slower rotor. However, these subsynchronous vibrations are actually stable vibrations. Wachel and Szenasi may have incorrectly diagnosed the subsynchronous vibrations in the fourth stage compressor as an instability.

Finally, numerical integration was used to study how a rotating moment arm contributes to harmonic vibrations. In cases with severe imbalance, the system exhibits 2nd order harmonics that may excite the system's natural frequencies as much, or more than the synchronous vibration.

REFERENCES

[1]   Wachel, J. C., and Szenasi, F. R., 1980 "Field Verification of Lateral-Torsional Coupling Effects on Rotor Instabilities in Centrifugal Compressors." *NASA Conference Publication 2133*, College Station, pp. 15-34.

[2]   Remmers, E. P., 1971, "The Dynamics of Gear Pair Systems," ASME Paper No. 71-DE-23.

[3]   Mitchell, L.D., 1975, "Torsional-Lateral Coupling in a Geared High Speed Rotor System," ASME Paper No. 75-DET-75.

[4]   Iwatsubo, T. I., Arii, S., amd Kawai, R., 1984, "The Coupled Lateral Torsional Vibration of a Geared Rotor System," *Proceedings of the Third International Conference on Vibrations in Rotating Machinery,* Heslington, England, pp. 59-66.

[5]   Iida, H and Tamura, A., 1984, "Coupled Torsional-Flexural Vibration of a Shaft in a Geared System," *Proceedings of the Third International Conference on Vibrations in Rotating Machinery,* Heslington, England, pp. 67-70.

[6]   Iannuzzelli, R.J., and Edwards, R.M., 1984, "Torsional/Lateral Coupling in Geared Rotors," ASME Paper No. 84-GT-71.

[7]   Simmons, H. R., and Smalley, A. J., 1984, "Lateral Gear Shaft Dynamics Control Torsional Stresses in Turbine-Driven Compressor Train," ASME Transactions, **106**, pp. 946-951.

[8]   David, J. W., and Park N. G., 1987, "The Vibration Problem in Gear Coupled Rotor Systems," *Proceedings of the Eleventh Biennial Conference on Mechanical Vibration and Noise*, Boston, pp. 297-303.

[9]   Ozguven, H. N., and Houser, D. R., 1988, "Dynamic Analysis of High Speed Gears by Using Loaded Static Transmission Error 1988b," Journal of Sound and Vibration, **125**, pp. 71-83.

[10] Zuerbes, A., Neumer T., Klimmek A., Schwibinger P., and Nordmann R., 1989, "Stability Behavior of Geared Rotor Systems Regarding Torsional Lateral Coupling," *Proceedings of the Twelfth Biennial Conference on Mechanical Vibration and Noise*, Montreal**,** pp. 217-224.

[11] Kahraman, A, Ozguven, H. N., Houser, D. R., Zakrajsek, J. J., 1992, "Dynamic Analysis of Geared Rotors by Finite Elements," ASME Journal of Mechanical Design, **114**, pp. 507-514.

[12] Nelson, H. D., Shiau, T. N., Chou, Y. W., and Chang, J. R., 1994, "A Study on the Dynamic Characteristics of Geared Rotor-Bearing System with Hybrid Method," ASME Paper No 94-GT-355.

[13] Norton, R. L., 2001, *Design of Machinery: New Media Version,* 3rd Ed. McGraw-Hill, Worcester, Massachusetts.

[14] Oberg, E., Jones, F.D., Horton H.L., Ryffel H. H., McCauley C. J., et al., 1986, *Machinery's Handbook,* 22nd Ed. Industrial Press Incorporated, New York.

[15] Vance, J., 1988, *Rotordynamics of Turbomachinery*, John Wiley and Sons, Inc. New York.

APPENDIX A

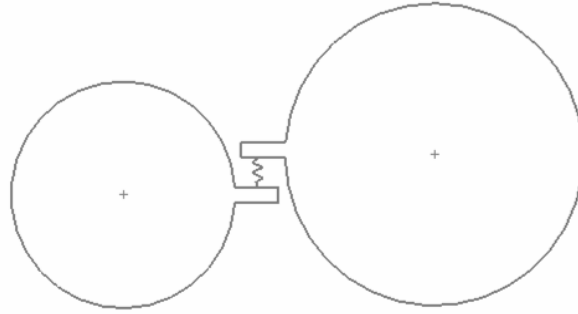Derivation of Torsional Equivalent Stiffness:

Case 1:

Figure 69: Gear pair with high bearing stiffness and 90 degree pressure angle.

$$T = \frac{1}{2}J_1\dot{\psi}_1^2 + \frac{1}{2}J_2\dot{\psi}_2^2 \qquad\qquad V = \frac{1}{2}K_n(R_1\psi_1 - R_2\psi_2)^2$$

$$\frac{\partial L}{\partial \psi_1} = K_n(R_1\psi_1 - R_2\psi_2) \qquad\qquad \frac{\partial L}{\partial \psi_2} = -K_n(R_1\psi_1 - R_2\psi_2)$$

$$\frac{d}{dt}\left(\frac{\partial L}{\partial \dot{\psi}_1}\right) - \frac{\partial L}{\partial \psi_1} = J_1\ddot{\psi}_1 + K_n(R_1\psi_1 - R_2\psi_2) \qquad\qquad \frac{d}{dt}\left(\frac{\partial L}{\partial \dot{\psi}_2}\right) - \frac{\partial L}{\partial \psi_2} = J_2\ddot{\psi}_2 - K_n(R_1\psi_1 - R_2\psi_2)$$

Converting to Matrix Form:

$$\begin{bmatrix} J_1 & \\ & J_2 \end{bmatrix}\begin{Bmatrix} \ddot{\psi}_1 \\ \ddot{\psi}_2 \end{Bmatrix} + \begin{bmatrix} K_n R_1^2 & -K_n R_1 R_2 \\ -K_n R_1 R_2 & K_n R_2^2 \end{bmatrix}\begin{Bmatrix} \psi_1 \\ \psi_2 \end{Bmatrix} = \begin{bmatrix} 0 \\ 0 \end{bmatrix}$$

Solving for the eigenvalues:

$$\left(K_n R_1^2 - J_1\lambda\right)\left(K_n R_2^2 - J_2\lambda\right) - \left(K_n R_1 R_2\right)^2 = 0$$

$$\cancel{K_n R_1^2 R_2^2} + \lambda\left(-K_n R_2^2 J_1 - K_n R_1^2 J_2\right) + J_1 J_2 \lambda^2 - \cancel{K_n R_1^2 R_2^2} = 0$$

$$\boxed{\lambda = -K_n \frac{\left(R_2^2 J_1 + R_1^2 J_2\right)}{J_1 J_2}}$$ Eigenvalue for Gear Pair with High Bearing Stiffness.
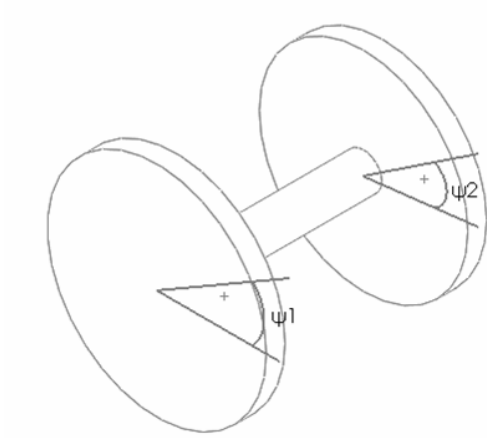
Case 2:

Figure 70: Equivalent torsional system used for eigenvalue check

$$T = \frac{1}{2}J_1\dot{\psi}_1^2 + \frac{1}{2}J_2\dot{\psi}_2^2 \qquad\qquad V = \frac{1}{2}K_nR^2(\psi_1 - \psi_2)^2$$

$$\frac{\partial L}{\partial \psi_1} = K_nR^2(\psi_1 - \psi_2) \qquad\qquad \frac{\partial L}{\partial \psi_2} = -K_nR^2(\psi_1 - \psi_2)$$

$$\frac{d}{dt}\left(\frac{\partial L}{\partial \dot{\psi}_1}\right) - \frac{\partial L}{\partial \psi_1} = J_1\ddot{\psi}_1 + K_nR^2(\psi_1 - \psi_2) \qquad \frac{d}{dt}\left(\frac{\partial L}{\partial \dot{\psi}_2}\right) - \frac{\partial L}{\partial \psi_2} = J_2\ddot{\psi}_2 - K_nR^2(\psi_1 - \psi_2)$$

Converting to Matrix Form:

$$\begin{bmatrix} J_1 & \\ & J_2 \end{bmatrix}\begin{Bmatrix} \ddot{\psi}_1 \\ \ddot{\psi}_2 \end{Bmatrix} + \begin{bmatrix} K_nR^2 & -K_nR^2 \\ -K_nR^2 & K_nR^2 \end{bmatrix}\begin{Bmatrix} \psi_1 \\ \psi_2 \end{Bmatrix} = \begin{bmatrix} 0 \\ 0 \end{bmatrix}$$

Solving for the eigenvalues:

$$\left(K_nR^2 - J_1\lambda\right)\left(K_nR^2 - J_2\lambda\right) - \left(K_nR\right)^2 = 0$$

$$\cancel{K_nR^2} + J_1K_nR^2\lambda + J_2K_nR^2\lambda + J_1J_2\lambda^2 - \cancel{K_nR^2} = 0$$

$$\boxed{\lambda = -K_nR^2\frac{(J_1 + J_2)}{J_1J_2}} \quad \text{Eigenvalue for Equivalent System} \qquad (92)$$

Setting Case 1 Eigenvalue equal to Case 2 Eigenvalue:

$$-K_n \frac{\left(R_2^2 J_1 + R_1^2 J_2\right)}{J_1 J_2} = -K_n R^2 \frac{\left(J_1 + J_2\right)}{J_1 J_2}$$

$$\boxed{R^2 = \frac{\left(R_2^2 J_1 + R_1^2 J_2\right)}{\left(J_1 + J_2\right)}}$$ Equivalent Radius to be used for Eigenvalue Projection   (93)

VITA

Michael Aaron Emery was born in Oklahoma City, Oklahoma. He was brought up in the cities of Amarillo and Houston and received his diploma from Mayde Creek High School in May 1997. In May 2003, he obtained his Bachelor of Science in mechanical engineering from Texas A&M University – College Station. He joined the Mechanical Engineering Department at Texas A&M University as a graduate student in August 2003, and graduated with his Master of Science in mechanical engineering in December, 2005. Michael may be contacted through Dr. John Vance at the Department of Mechanical Engineering, Texas A&M University, College Station, TX 77843-3123.